Disorder-based Electromagnetic Devices

by

Mohammad Haghtalab

A thesis
presented to the University of Waterloo
in fulfillment of the
thesis requirement for the degree of
Doctor of Philosophy
in
Electrical and Computer Engineering

Waterloo, Ontario, Canada, 2019

Examining Committee Membership

The following served on the Examining Committee for this thesis. The decision of the Examining Committee is by majority vote.

External Examiner: Nader Engheta
Professor, Department of Electrical and Systems Engineering
University of Pennsylvania

Supervisor: Safieddin Safavi-Naeini
Professor, Department of Electrical and Computer
Engineering, University of Waterloo

Internal Member: Simarjeet Saini
Associate Professor, Department of Electrical and Computer
Engineering, University of Waterloo

Internal Member: Irene Goldthorpe
Associate Professor, Department of Electrical and Computer
Engineering, University of Waterloo

Internal-External Member:	Zoran Miscovic Professor, Department of Applied Mathematics University of Waterloo
Defense Chair:	Vasudevan Lakshminarayanan Professor, Department of Optometry and Vision Science University of Waterloo

Abstract

Engineered complex media with unusual and exotic electrical properties, realized through subwavelength building blocks, are leading to the development of new applications and improved functionalities in a variety of fields. These range from electromagnetics- such as frequency selective surfaces, photonic crystals and various forms of the so-called metamaterials- to optical microscopy, nanolithography, quantum optics, and medicine. The potential of this area has spurred growing investment by industry and a huge amount of interest from the research community, as they strive to develop novel structures that reduce the cost and improve the performance of existing and emerging systems.

At the heart of this development is the engineering of electromagnetic wave interactions with complex structures composed of subwavelength pieces. Thus far, extensive efforts have been made to exploit the advantages offered by the periodicity and combination of different materials with desirable electromagnetic properties at the intended frequency bands. Despite the simplicity provided by periodic structures in terms of design, fundamental limitations are imposed by current fabrication techniques and material losses and imperfections.

In response, designs based on disordered structures with exotic properties have attracted wide attention. It has been shown that disorder and aperiodicity can lead to novel applications that are either impossible or too expensive to implement through periodic structures. Examples include omnidirectional anti-reflection coatings, imaging through complex media, localization of light far beyond the diffraction limit, and cloaking devices, to name a few. The extension and development of novel applications based on innovative approaches is clearly of great value.

The contributions of the present work, from an analysis and optimization point of view, include a new computationally efficient method to analyze the interaction of electromagnetic waves with complex structures composed of subwavelength scatterers in multilayer media, and the development of a novel design optimization algorithm for fast and efficient design of disorder-based electromagnetic devices. A complex images Green's function technique is employed for the fast and accurate calculation of matrix elements in the method-of-moments used to model the field interaction with optical nanoantennas. A new scheme, for the analysis of multiple scattering in complex systems, and a novel optimization algorithm, called the "near optimal freeform inverse design" (NOFID) approach, are employed to design structures with new functionalities and to improve the efficiency in existing/emerging electromagnetic devices.

In terms of design and application contributions, the devised analysis method and algorithm are used to design new structures based on engineering the multiple scattering occurring inside disordered systems. More specifically, it is demonstrated that engineered disorder can provide control over electromagnetic wave interactions with designed structures through excitation and optimal selection of desired localized/non-localized modes. Novel contributions include the design of highly coupled optical nanoantennas. The proposed analysis method, based on complex images technique, along with the simulated annealing optimization approach, are used to design disordered nanoantenna structures for optical signals multiplexing and demultiplexing that works by engineering the excited localized plasmonics modes. The developed NOFID algorithm is employed to design disordered dielectric metalenses for super-resolution imaging and communication by controlling the non-localized far-field radiating modes. The analysis of multiple scattering inside a network of disordered highly-coupled nano/micro wires reveals that such structures can be employed to realize self- invisibility or achieve significant localization of incident electromagnetic fields. The invisibility of disordered silver nanowires (AgNWs) with specific geometrical parameters at the millimeter wave range of frequencies is demonstrated. This is achieved through the decoupling of excited modes inside percolated networks of AgNWs. This feature is used to efficiently control the electrical properties of graphene in a millimeter-wave radiating device without disturbing the radiation characteristics of the original radiating structure. Finally, the NOFID algorithm, is employed to design a metastructure composed of metallic wires to demonstrate the enhanced localization of incident waves with various polarizations. This work ends with concluding remarks and provides suggestions for future work.

Acknowledgements

Tackling new areas of research has been an enriching experience; at times it has been exciting, at times depressing. Looking back, many people have helped turn this into a rewarding experience to whom I wish to express my gratitude.

First and foremost, I would like to express my gratitude to my supervisor, Professor Safieddin (Ali) Safavi-Naeini. His encouragement and support, his many insights and ideas have been invaluable throughout all stages of the work. I have been very fortunate to have him with solid diverse knowledge and intuition in a broad range of new applications.

I would wish to express my gratitude to Professor Federico Capasso of Harvard University. I am grateful for an amazing collaboration we started during the last years of my Ph.D. Mainly known for his invention of quantum cascade lasers, among his other seminal contributions, his support, passion and determination for science set a role-model for all who have worked with him.

I would like to thank my committee members Professors Simarjeet Saini, Irene Godthorpe, and Zoran Miskovic. My special thanks to Professor Irene Goldthorpe for her help and collaboration on the silver nanowire project, and her valuable comments and suggestions. My sincere thanks to Professor Nader Engheta of the University of Pennsylvania for accepting our invitation to be my external examiner.

My thanks to all CIARS members, friends and colleagues from Waterloo; Chris Schroeder for her administrative support; my special thanks to Mohsen Raeiszadeh for helping me out with many technical/non-technical problems; Hadi Hosseinzadeh for providing help on silver nanowire project; Nathan Fitzpatrick, Brian Goddard, and Rod Salandanan for their help in fabrication; Aidin Taeb and Gholamreza Z.Rafi for their support with the VNA, the laser machine, and near-field measurement systems; Shahed Shahir for helpful discussions on THz and millimeter-wave imaging systems; Hussam Al-Saedi for his help in milling machine and fruitful discussions on fabrication techniques; Naeimeh Ghafarian and Mehdi Salehi whom I had a pleasure to do collaboration with; Hadi Amarloo, Wael M. Abdel-Wahab, Behrooz Semnani, Ahmad Ehsandar, Mohammad Fereidani, Nazy Ranjkesh, and Mehrbod Mohajer for helpful discussions.

I have also been very fortunate to work closely and have helpful discussions with some wonderful peers and colleagues at Harvard and MIT; my special thanks to Michele Tamagnone for all his help on various theoretical/practical challenges; Reza Khorasaninejad, Wei-Ting Chen, Alexander Yutong Zhu, Yao-Wei Huang, Zhujun Shi, Noah Rubin, Xinghui Yin, Paul Chevalier, Nanjia Zhou, Kundan Chaudhary, Arman Amirzhan, Joon-Suh Park, Professor Steven Johnson of MIT, Raphael Pestourie, and Wu Zhang for the constructive

discussions and feedbacks. I would like to thank Jared Sisler for his help on some of the graphics used in this thesis. Thank you to all my other friends in Capasso group, Gabriele D'Aversa, Christina Spagele, Zameer Bharwani, Marco Piccardo, and Yousef Kerolos for the time and enjoyment we shared.

I would like to take this upportunity to thank Professors Reza Faraji-Dana and Mahmoud Shahabadi of the University of Tehran. Most of the knowledge I have used throughout this work, I learnt from them.

I would also like to acknowledge National Science and Engineering Research Council of Canada (NSERC), BlackBerry, C-COM Satellite Inc., and National Science Foundation (NSF) for funding the research.

Last, but not least, I would like to thank my wife, Azhar, for her understanding, inspiration, continuous support and patience; our parents for their unconditional support; and our two kids for being exceptional sources of energy and joy in our life.

To my Family

Table of Contents

List of Tables

List of Figures

Chapter 1

Introduction

The interaction of waves with objects is an established phenomenon in science and engineering, and appears in a variety of fields such as electromagnetism, condensed-matter physics, acoustics, seismology, and hydrodynamics. Multiple scattering is the mathematical theory and technology needed to understand and describe this phenomenon [3]. Taking advantage of multiple scattering, various structures have been developed and designed to realize novel applications (e.g., artificial materials or meta-materials, photovoltaic technology, imaging, beamforming) in which the incident fields are manipulated to achieve intended specifications. The spatial order and periodicity of the objects in these structures are considered integral parts of the design procedures. Techniques to eliminate disorder and optimize regularity have been devised to improve the functionality in many structures like photonic crystals, Bragg reflectors, and phased array systems, whereby the amplitude and phase of the radiated and/or guided waves can be controlled precisely. Irregularities are known to have detrimental effects and can result in inefficient designs. However, with scientists learning how to harness disordered media, the study of disordered systems has become an active topic of research in recent years [4].

The scattering of waves by disordered objects is an everyday occurrence in nature, cropping up for example in the scattering of light when it passes through clouds, human bones, or milk. However, the process was not well understood for centuries until in 1957 Phillip Anderson proposed that the coherent scattering of electrons passing through disordered crystals causes materials to no longer conduct charges, essentially becoming insulators [5]. Anderson, while studying electron transport inside semiconductors using quantum mechanical modeling, noted that the scattering of electron wavefunctions due to the semiconductor's defects and impurities led to a localized phenomenon that was a direct consequence of the interference of the waves resulting from the multiple scattering process.

Inspired by this observation, microwave and optical analogies of Anderson's localization theory have been investigated in an effort to better understand the localization of waves and to explore parallel applications in other fields in physics and engineering [6] such as communication, imaging, random lasing, and solar energy.

The concept of modes is pivotal to all wave phenomena in physics. In classical electromagnetism theory, modes are the solutions to source-free Maxwell equations. Relating this to the Anderson localization, the multiple scattering process inside disordered media leads to highly confined spatial modes that are hardly coupled to their environment. The modes inside close cavities behave in a similar manner. Based on this similarity, a new field of research has been developed which deals with lasing inside random photonic materials [7]. Combining the modes of disordered materials with gain medium, random lasers achieve the feedback and amplification needed for lasing and posses new characteristics not found in conventional lasers. Unlike the conventional, monochromatic, single-mode lasers designed for use in well-defined cavities, random lasers excite a large number of modes leading to a broader spectral bandwidth. This is due to the fact that each mode corresponds to a particular frequency in the spectral domain. Additionally, the direction of emission for each mode can be different from the others, causing the formation of a complex and disordered profile of spatial emission. Various aspects of random lasers are currently under investigation [8, 9, 10]. Random lasing has also been observed in clouds of cold atoms, where the atoms provide both the gain and scattering needed for the lasing process [11].

Wave transport through scattering media is of both fundamental interest and practical importance. Two classes of problems are considered here. The first class deals with wave propagation inside different types of waveguides in which introduced disorder gives rise to interesting features. The second class considers the free space radiation of waves inside disordered random media. Light localization has been investigated in disordered photonic crystal waveguides [12]. By introducing scattering elements in two-dimensional (2D) waveguides, microwave localization can be achieved [13]. It has also been shown that transverse confinement can be preserved when disorder is introduced in photonic waveguides [14]. Disordered media are also used to improve the absorption of light in solar cells where the coupling between sunlight and the excited modes due to multiple scattering reduces the amount of energy that can escape from the structure, thereby increasing the efficiency of the cell [15]. Light transport through highly-scattering nanowire mats is investigated in [16]. It is demonstrated that the transmission of light occurs through exciting a few 'open' modes, with transmission close to unity, while the transmission of a large number of excited 'closed' modes is negligible.

One of the main motivations to study wave propagation inside disordered media is the possible application to the transmission of information by electronic or photonic devices or through wireless communications [17]. Communication through disordered media has been studied extensively in order to increase the maximum possible information that can be transferred to receiver(s); this is known as channel information capacity [18]. It has been shown that, unexpectedly, disordered media can lead to an increase in the amount of information that can be sent through a channel rather than limiting the information capacity, when a multiple-input multiple-output (MIMO) scheme is employed [19]. This is due to the fact that the disorder increases the aperture of the lens looking at the transmitting array; this allows the receivers to capture signals from a wider range of directions and thus increases the number of signals distinguishable by the receiving array. However, limiting factors are the correlation between the signals received by the receiver antennas and the signal-to-noise ratio (SNR) that is degraded by the noise power present in the system.

Disorder is a rich subject area which has inspired scientists and engineers to study and discover its wealth of interesting physical effects and potential applications. In this thesis, the author studies and realizes novel disorder-based electromagnetic (EM) devices. The main purpose of the thesis is the design and analysis of disordered structures that interact with impinging EM waves. Several novel concepts and applications are introduced and implemented, operating at the optical and millimeter wave (mm-W) ranges of the EM spectrum.

1.1 Mode engineering through engineered disorder

A pivotal concept to wave phenomena in general, and to EM theory in particular, EM modes are referred to as the solutions to source-free Maxwell equations in a given media with known physical characteristics and specified boundary conditions (BC). Maxwell's equations describe how the EM waves are generated and how they evolved through the media from a given set of sources including electrical charges and currents as:

$$\begin{aligned}\nabla \times \mathbf{E}(\mathbf{r},t) &= -\frac{\partial \mathbf{B}(\mathbf{r},t)}{\partial t},\\ \nabla \times \mathbf{H}(\mathbf{r},t) &= \frac{\partial \mathbf{D}(\mathbf{r},t)}{\partial t} + \mathbf{J}(\mathbf{r},t).\end{aligned} \tag{1.1}$$

Traditionally, the constitutive equations of a medium are described in the frequency domain as $\mathbf{D}(\mathbf{r},\omega) = \epsilon(\mathbf{r},\omega)\mathbf{E}(\mathbf{r},\omega)$ and $\mathbf{B}(\mathbf{r},\omega) = \mu(\mathbf{r},\omega)\mathbf{H}(\mathbf{r},\omega)$; however, in its most general form the displacement field, $\mathbf{D}$, and the induced magnetic field, $\mathbf{B}$, are described by functionals that depend on both the electric ($\mathbf{E}$) and magnetic fields ($\mathbf{H}$) as $\mathbf{D} = f_{\mathbf{D}}(\mathbf{E}, \mathbf{H})$ and $\mathbf{B} = f_{\mathbf{B}}(\mathbf{E}, \mathbf{H})$. Here, the values of the EM fields at any time (t) and at a given spatial location ($\mathbf{r}$), may depend on the values of the EM fields at all spatial locations at the present moment and at all previous times (complying with causality). The non-trivial solutions that satisfy the above equations for $\mathbf{J} = 0$ and $\rho = 0$ ($\nabla.\mathbf{J} = \frac{-\partial\rho}{\partial t}$), are defined as the modes supported by the media/structure.

The ultimate goal of EM waves/modes engineering is to design the media in such a way that given boundary conditions and exciting sources can achieve a desired EM wave distribution at near and/or far distances from the source region. A tremendous amount of effort has been expended over the past few decades to find analytical solutions to these equations for simple media/structures. However, the complications involved in real-life scenarios require a totally different approach to finding solutions to Maxwell's equations.

The advent of computers gave scientists and engineers powerful computational resources to approach this problem from an entirely different perspective. First considered as auxiliary tools to support the validity of analytical solutions and theoretical predictions, numerical methods were developed by mathematicians/engineers. Later, these methods started to become essential gadgets in the analysis and design process of a wide range of real-life physical systems. As the role of such tools became clearly game-changing for emerging engineering systems, researchers began to explore this field as a separate research area of which the aim was to develop new computational techniques and improve existing ones to adapt to current scientific and engineering application needs. Not only do such computational resources and techniques facilitate the process of finding/engineering the solutions of mathematical equations describing underlying physical phenomena, they provide a virtual experimental environment to explore and even discover new phenomena [20] while emulating real-life and natural physical scenarios including inevitable random processes and structures that are subject to large unavoidable uncertainties. Chaotic dynamic systems are among the best examples for which extensive and efficient computational efforts are crucial in order to predict and analyse the outcomes of real "deterministic" physical systems that are extremely sensitive to the initial (present) conditions. Although at first glance this unpredictable behavior may seem to be detrimental for engineering systems that typically require a robust outcome, it can be exploited to achieve goals which are very difficult if not impossible to achieve through regular systems [21, 22, 23]. This new approach, referred to as "engineered chaos", aims to take advantage of chaotic features; this is quite different from "chaos engineering" which focuses on approaches aimed at stabilizing dynamic systems, making them more tolerant to noise and turbulence [24]. The author's goal in this work is to harness randomness in disordered EM structures to develop new functionalities for emerging scientific/engineering applications and to improve the performance of existing devices. More specifically, engineered disorder is explored to design and realize desired EM modes in a variety of applications ranging from optics and photonics to mm-W and microwave communication/imaging systems. The contributions encompass the whole chain of required steps to realize disorder-based EM devices. They include the development of a fast and accurate EM solver, the selection of an efficient optimization approach to optimize designed disordered structures, and the realization of designed structures. The developed concepts and realized structures exploit randomness to create desired modes, and engineer the strength and spatial locality of the excited modes in the desired ways. This includes the engineering of optical plasmonic modes confined to close proximity in designed optical structures or nanoantennas. The engineering of far-field propagating modes is also investigated. A new class of metalenses with super-resolution properties is developed. In another study, the author investigates mode decoupling due to disorder in percolated networks of silver nano-wires (AgNWs). This feature is used to realize near-invisible electrodes in the mm-W range of frequencies. Also, the developed optimization algorithm is employed to design three dimensional (3D) scattering structures where the incident EM waves undergo multiple scattering to become localized over the desired region(s). In the following sections, an overview is given of the concepts and steps detailed in the remaining chapters, and the organization of the thesis is provided.

1.2 Disordered electromagnetics computational techniques

The field of computational electromagnetics (CEM) deals with the development of numerical techniques to solve Maxwell's equations in irregular media where analytical solutions cannot be obtained easily. This situation arises in the computation of the interaction of EM waves with media which have complex constitutive relations under various boundary conditions. A variety of techniques have been developed and employed for different applications dealing with the calculation of EM scattering, absorption, radiation and guided waves across the solution domain. Depending on the application, time-domain or frequency-domain approaches have been followed. The geometry of objects interacting with EM waves has also been an important factor in determining the type of numerical technique used to solve the problem. Methods like those based on finite element (FEM) techniques are best suited to frequency-domain solutions and general complex geometries; while time-domain methods such as those based on finite difference time-domain (FDTD) techniques are best suited for systems featuring wideband or transient excitations and responses. On the other hand, method of moments (MoM) approaches are suitable for structures using Green's functions for the background medium that are calculated analytically or numerically, facilitating the computational process. Unlike the two former methods, there is no need to define absorbing boundary conditions in the latter approach as Green's functions take into consideration the effect of the background medium and the boundary conditions. The step that is common to all these techniques is the discretization of the solution domain where the calculations of the fields distribution (**E** and **H**) are carried out. While in the FEM- and FDTD-based methods the entire solution domain must be extended to the absorbing boundary conditions to be discretized, in MoM-based approaches only the scattering objects need to be discretized. This leads to a remarkable reduction in the size of the resultant matrices in this technique. However, these matrices are densely populated as opposed to those of the FEM approach where near-sparse matrices are obtained for EM-field calculations. The proper numerical approach(es) should be developed or chosen for design optimization in disordered structures. For example, in problems where the EM waves interact with objects in the presence of a multilayered background, using FEM or FDTD would not be efficient due to the requirements for the discretization of the entire solution space. Although MoM seems to be much faster, it suffers from having to calculate Sommerfeld's integrals which are not easily converged. To overcome this drawback, various techniques have been proposed to accelerate the numerical evaluation of Sommerfeld's integrals appearing in the Green's functions of multilayered media. The complex-images (CI) technique is one of the most successful solutions to this issue. Accelerating the computation of the impedance matrices ($[Z]$) in the MoM, this technique simplifies the process of EM modeling for various applications ranging from microwave integrated circuits to photonics and optical lithography.

The development of fast EM field solvers, used in the forward problem, is key for optimizing large-scale complex structures such as disordered structures. This is therefore a key objective of this thesis. Two distinct structure features targeted in this work include the non-periodicity of lattice in designed devices and the infinitely large degrees of freedom in the definition of possible various configurations determined by the locations and sizes of inclusions. To analyse and design structures with these properties, one requires both a fast EM field solver and a fast optimization technique. For a fast numerical solver, essential in the analysis of multilayered structures, the author employs the CI technique to compute the matrix elements in the MoM. Although the approach has been used in other studies, here, for the first time, it is applied to plasmonic structures. The details are provided in Chapter 2 of this thesis: the problem of engineering the near-field due to EM interactions with optical nano scatterers with arbitrary configurations is investigated.

In its most general form, the optimization of complex structures made up of infinitely large numbers of inclusions can assume an infinite number of configurations; thus, the development and employment of a novel technique for optimization is required. Algorithms that have been proposed for optimization can be divided into two major groups. Starting from an initial point in the solution space, local optimization algorithms try to find the optimum value of function in the vicinity of the initial point. On the other hand, global optimization algorithms aim at finding the best optimum point in the entire domain of solution space. Because of this difference, the processing time of local optimization algorithms is much less than that of the global optimization approaches; the latter typically needs to examine more points inside the solution domain before starting to converge on the best or close to the best solution(s). Nevertheless, global optimization algorithms look more appealing to scientists and engineers given the nature of engineering problems, i.e. the defined cost functions that satisfy different criteria demonstrate multiple local minima or maxima within the solution space and it is usually desirable to find the best solution(s) for the given trade-offs. Methods known as Genetic Algorithms (GA), Particle Swarm Optimization (PSA), Simulated Annealing (SA), Evolutionary Optimization (EO) and different combinations of these are among the global optimization approaches. One inherent limitation of all these methods is that they operate based on different combinations of input variables defined based on the discretization of the solution domain. As the dimensions of the problem increase or the sizes of the defined variables expand, the process of searching for the best solution become computationally expensive. To solve this issue in highly complex structures, methods based on gradient descent such as Topology Optimization (TO) have been proposed. Although some tricks are involved to prevent these methods from getting stuck into local solutions, they still suffer from the fundamental issue of not efficiently searching the entire solution space to find the “better” solutions. To overcome this drawback, the author developed a novel optimization approach suited to highly-complex disordered structures. Not being bounded to the limitations imposed by the discretization, the proposed method called “Near-Optimal Freeform Inverse Design” (NOFID) explores a theoretically “infinite”-dimensional solution space while gradually perturbing the solution towards optimizing the cost function(s). More details of the proposed method are provided in Appendix B. The method is successfully employed to design metalenses with engineered far-field propagating modes; resulting in a remarkably enhanced resolution far beyond the diffraction limit.

1.3 Optical radiation dynamic control: state of the art

The main role of optical antennas is to convert localized EM fields from/to the nanoscale regions to/from the far-field radiating modes. They have found a wide range of applications from sensing to quantum optics [25, 26, 27, 28]. The design and control of the radiation characteristics of nanoantennas have been the focus of various studies and can be classified into two groups. The first group of methods propose various schemes to control the spectral response of nanoantennas. Dynamic color displays [29] and multiresonant nanoantennas for resolving molecule-specific information in dynamic environments [30] are examples that use spectral control of nanoantenna radiations. The second group engineers the spatial characteristics of nanoantenna radiations. Examples include optical phased array antennas that change the amplitude and phase of individual radiating elements to control the direction of radiation pattern in the far-field region [31, 32]. Controlling the near-field of optical fields has been demonstrated in strongly scattering materials where, by controlling the phase front of the incident plane waves over the input plane, the transmitted fields can be controlled to achieve highly-localized EM fields over the output plane [33, 34]. While there is no control over the exact location of incoming wave concentration, by using “disorder engineered” nanoantennas, the author demonstrates full control over the location of these “hot spots” where each is associated with a unique phase matrix defined over the input plane (Chapter 2). Table 1.1 summarizes some of the existing approaches for controlling the optical responses of nanoantennas.

Table 1.1: Selected technologies for dynamic control of optical waves.

Reference	Type	Material	Application
[29]	Spectral	Au, Ag, Mg	Dynamic control display
[30]	Spectral	Au	Molecular biology
[31, 32]	Spatial	Au, Si	Optical communication
[33, 34]	Spatial	Rutile TiO_2, etc.	Imaging through scattering media
This work	Spatial	Au	Spatial optical multiplexing

1.4 Information enhancement through scattering media: state of the art

Effective generation and transmission of information through scattering media is of great importance in emerging imaging systems and highly beneficial in wireless communication. A variety of techniques have been proposed to enhance this process. The first group of techniques aims to develop devices based on engineered metastructures where arrays of highly-coupled sub-wavelength-scale scatterers are employed not only to realize the same functionalities as conventional bulky optical/electrical devices but also to develop multi-functional devices through planar structures [35, 36, 37, 38]. In this way, highly integrated devices with superior efficiencies can replace current bulky systems and be employed to address demands in emerging applications such as virtual and augmented reality (VR/AR). However, due to the limitations imposed by the diffraction of EM/optical waves, super-resolution features cannot be achieved through these structures. The second group of techniques benefits from the combination of designed scattering media and computational techniques for further enhancement of information capacity and fidelity. Examples include using machine learning algorithms to visualize 3D structures of biological cells through microscopy [39], the physical realization of machine learning by diffractive deep neural networks (D^2NNs) [40], imaging through scattering layers [41], and using time-reversal (TR) techniques for imaging beyond the diffraction limit [42]. While the focus of reported research has been the improvement of imaging/communication systems, not all proposed methods can achieve super-resolution features for a "given" scattering medium. In this thesis, the author proposes a method to design "disorder engineered" all-dielectric metalenses to significantly enhance the resolution of imaging systems and the capacity of information in current communication systems. This is done through using the singluar value decomposition technique (SVD). As will be shown in Chapter 3, the "disordered" nature of the proposed structures leads to superior characteristics when compared to those of conventional structures. Table 1.2 summarizes some of the state of the art techniques.

Table 1.2: Techniques for information enhancement using scattering structures.

Reference	Engineered Media	Computational technique	Diffraction limited
[35, 38]	Yes	-	Yes
[42]	No	TR technique	No
[39]	No	Artificial neural networks	Yes
[41]	No	Speckle correlation	Yes
[40]	Yes	Deep neural networks	Not reported
This work	Yes	SVD technique	No

1.5 Invisibility cloak: state of the art

Making objects invisible to impinging EM waves has been of significant scientific and technological interest. A variety of techniques have been proposed to realize invisibility through engineered structures such as metamaterials. However, the suggested approaches impose practical limitations for a wide range of applications. Limitations include the scalability of the approach, the requirement to employ loss/gain materials or satisfy a required refractive index (RI) profile within the structure, the frequency bandwidth, and the electrical/heat conductivity, to name a few [43, 44, 45, 46, 47, 48, 49, 50]. Considering these limitations, the author demonstrates that engineered disorder can alleviate many of the disadvantages associated with other proposed methods. In Chapter 4, it is theoretically and experimentally demonstrated that networks of disordered AgNWs with certain geometrical parameters can exhibit invisibility features. As an application example, it is shown that EM radiating devices can benefit from such structures to achieve higher performance in the designed specifications. Table 1.3 summarizes some of the current proposed methods and provides key properties attributed to each method.

Table 1.3: Techniques for information enhancement using scattering structures.

Reference	Method	Adv.	Disadv.
[45]	Transformation optics (TO)	Scalability	Bandwidth RI requirement
[46]	TO (Carpet cloak)	Bandwidth	Not general (3D)
[47]	Scattering cancellation	Sensor's app.	Scalability
[48]	Kramers-Kronig relations	Self invisibility	Scalability Bandwidth Loss/Gain materials
[49]	Hilbert transform	Self invisibility	Scalability RI requirement
[50]	Scattering cancellation	Self invisibility Conductivity	Bandwidth
This work	Disorder induced mode decoupling	Self invisibility Conductivity Bandwidth Scalability	Scattering residuals

1.6 Disorder induced localization: state of the art

The multiple scattering process inside disordered media leads to highly confined spatial modes that are only loosely coupled to their environment. Combining the modes of disordered materials with a gain medium is the key concept in random lasers with new characteristics not found in conventional lasers. Various aspects of random lasers are currently under investigation [7, 8, 9, 10]. Random lasing has also been observed in clouds of cold atoms, where the atoms provide both the gain and scattering needed for the lasing process [11]. Based on a similar principle, light localization has been investigated in disordered photonic crystal waveguides [12]. By introducing scattering elements in a 2D waveguide, microwave localization can be achieved [13]. It has also been shown that transverse confinement can be preserved when disorder is introduced in photonic waveguides [14]. Disordered media are also used to improve the absorption of light in solar cells where the coupling between the sunlight and the excited modes due to multiple scattering reduces the amount of energy that can escape from the structure; thereby, increasing the efficiency of the cell [15]. Recent studies have investigated the engineering of laser optical modes generated by "engineered disorder," leading to the enhancement of emission characteristics in terms of direction and spectral properties [51]. However, the reported works are limited to lower dimensions (uni-dimensional and 2D systems). This is due to the fact that satisfying the Ioffe-Regel criterion, $kl \leq 1$, where l is the mean free path and k is the wavelength, is difficult to achieve in optics [7]. In Chapter 5 of this thesis, the author proposes a multilayer structure designed using the developed optimization algorithm (NOFID), that employs disorder engineered identical micro-wires dispersed at different layers in order to enhance the localization of the incident EM waves.

1.7 Thesis organization and original contributions

This thesis covers both theoretical and experimental work and is organized as follows (Figure 1.1):

- **Chapter 1**: Provides an introduction to the theoretical background and conventional frameworks used to model and design disordered EM structures. Throughout the thesis, state of the art methods related to the development of disorder-based EM devices are referenced and serve as a starting point for novel contributions.
- **Chapter 2**: Describes the development of a fast and accurate computational method for analysing EM wave interactions with multilayer structures. The method is used

to analyse and design disordered optical antennas with engineered localized modes. *Original contribution*: Complex-image Green's functions are developed to model the interaction of light with optical antennas embedded in multilayer media. This numerical method has not previously been applied to such structures. It is shown that orthogonal transmission channels can be realized. Each channel is associated with a localized plasmonic mode confined in the near-field of the illuminated disordered nanoantenna. These channels can be employed for the spatial multiplexing and demultiplexing of optical signals. Such an application of optical antennas has not previously been reported. *Publications*: [JA1], [CA1], [CA2].

- **Chapter 3**: Presents a study of dielectric metalenses composed of disordered arrangements of highly coupled dielectric wires. The singular value decomposition technique is used to analyse the far-field propagating modes when the metalenses interact with emitted fields from point sources located at sub-wavelength distances from each other, and close to the structures. *Original contribution*: Using the developed optimization algorithm (NOFID), a new class of metalenses are introduced. Such devices enhance the information content of far-field signals emitted from point sources located at sub-wavelength distances. The far-field signals can be decomposed in terms of orthogonal modes (channels) which can be used to modulate transmitter signals. In this way, both the resolution and the information capacity can be significantly enhanced in imaging/communication systems. Both the optimization algorithm and the proposed metalenses are original contributions. *Publications*: [JA2], [CA4].

- **Chapter 4**: The interaction of EM waves with percolated networks of AgNWs is studied. AgNWs with proper geometrical parameters are shown to have minimal interactions with impinging EM waves. *Original contribution*: The near-invisibility features of select type of AgNWs are theoretically and experimentally demonstrated. The integration of these structures with tunable EM devices is studied. It is shown that highly tunable devices in the mm-wave range of frequencies can be achieved using such invisible electrodes. The study of the invisibility of such structures and the design and fabrication of such devices are novel contributions to the field. *Publication*: [JA3].

- **Chapter 5**: The developed optimization algorithm (NOFID) is employed to design a structure made of layers of highly coupled "disorder engineered" metallic wires. The device is designed to maximize the localization of the incident EM waves at specified locations.*Original contribution*: To the best of the candidate's knowledge, this is the

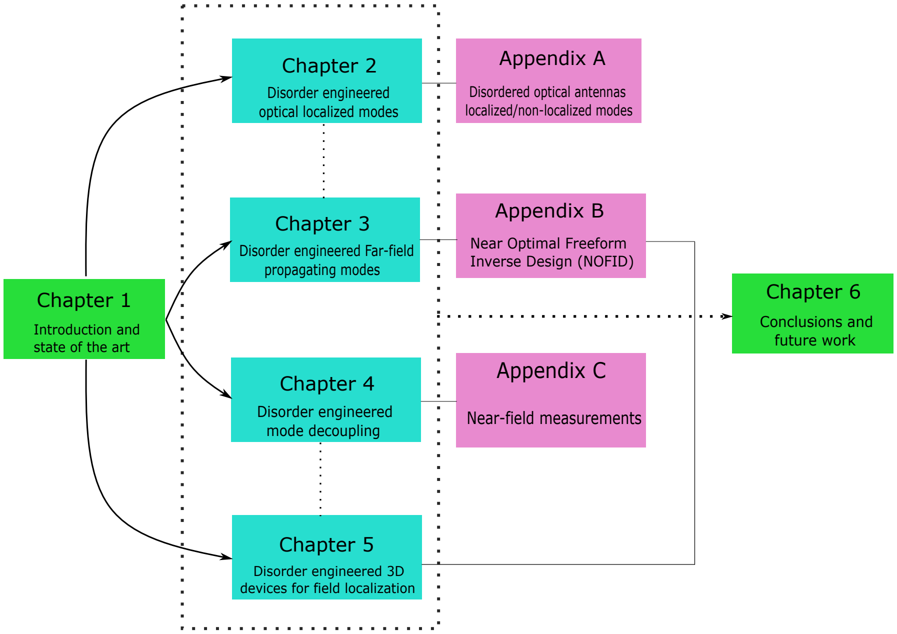

Figure 1.1: Thesis organization.

first 3D "disorder engineered" structure designed for 3D localization of impinging waves.

- **Chapter 6**: Conclusions and suggestions for future work are presented.
- **Appendix A**: Study of localized and nonlocalized modes of disordered optical antennas.
- **Appendix B**: Detailed description of the "Near-Optimal Freeform Inverse Design" (NOFID) algorithm developed for "disorder engineered" EM devices.
- **Appendix C**: Near-field measurement results as discussed in Chapter 4 of the thesis.

1.8 Publications

[JA1] M. Haghtalab, R. Faraji-Dana, and S. Safavi-Naeini, "Design and analysis of disordered optical nanoantenna structures," Journal of Lightwave Technology, vol. 34, no. 11, pp. 2838-2847 (2016).

[JA2] M. Haghtalab and S. Safavi-Naeini, “Freeform engineered disordered metalenses for super-resolution imaging and communication,” Optics Express, vol. 26, pp. 9749-9771 (2018).

[JA3] M. Haghtalab, S.M. Raeis-Zadeh, H. Hosseinzadeh Khaligh, I.A. Goldthorpe, and S. Safavi-Naeini, “Near invisible nano-wires and their implications in highly efficient electromagnetic devices,” Submitted.

[CA1] M. Haghtalab, and S. Safavi-Naeini, “Disordered nanoantennas: A new paradigm in space-division multiplexing,” CLEO: Science and Innovations. Optical Society of America, 2017.

[CA2] M. Haghtalab, S.M. Raeis-Zadeh, and S. Safavi-Naeini, “Space division multiplexing using disordered optical antennas,” IEEE International Symposium on Antennas and Propagation, USNC/URSI National Radio Science Meeting, pp. 1751-1752, 2017.

[CA3] M. Haghtalab, M. Tamagnone, S. Safavi-Naeini, and F. Capasso, “Negative refraction based on guided-mode assisted meta-gratings,” IEEE International Symposium on Antennas and Propagation, USNC/URSI National Radio Science Meeting, 2018.

[CA4] M. Haghtalab, F. Capasso, and S. Safavi-Naeini, “Near optimal freeform inverse design approach for future metastructures,” META 2018 Conference (accepted), 2018.

Chapter 2

Design and Analaysis of Disordered Optical Nanoantenna Structures

Nanoantennas are optical wave radiating structures operating based on the same physical principles as those underlying their radio-frequency counterparts. However, the physical properties of materials in the optical range of frequency cause different response to the incident electromagnetic field leading to novel applications in optics. The conventional methods for the analysis and design of antennas need to be modified for these structures. An integral equation formulation using the complex images Green's function technique is employed to model the optical wave interactions with nanoantennas embedded in multilayer media. The scattered field by an arbitrary shape nanoantenna is described by the mixed potential integral equation formulation. In this formulation the electric field is represented in terms of complex images Green's functions. The method of moments is then employed to solve the resulting integral equation. In this way an accurate and computationally efficient method is achieved. The accuracy of the proposed model is confirmed through comparison with direct numerical integration results. In addition, the comparison is made between the results obtained by the proposed method and those obtained by a full-wave finite-element method. The developed method is combined with the simulated annealing algorithm to design and optimize structures composed of strongly coupled nanoscale scatterers. It is shown that not only can they lead to improved efficiency in optical devices, but also orthogonal transmission channels are attainable when they are excited properly. The latter provides a new scheme for encoding and multiplexing signals in optical information systems.

2.1 Introduction

The ever-increasing advances in nanotechnology are leading to the realization of nanostructured materials among which are various forms of metallic structures. Utilizing the optical properties of metals, metallic nanostructures are capable of coupling the free space propagating optical waves with plasmonic resonances to localize the incident waves by several orders of magnitude in the regions much smaller than the wavelength. These structures have found many applications especially in biosensing and nanolithography and can also be used to enhance the nonlinear effects and radiation efficiency of nanoscale optical and quantum sources [25, 26, 27, 28].

Nanoantennas have created new possibilities for processing electromagnetic waves for a wide range of applications. Arrays of plasmonic particles either in the form of Yagi-Uda nanoantennas or artificial materials (metamaterials) are used to manipulate light in unprecedented ways [52, 53]. Thanks to the plasmonic features, the diffracted fields from the illuminated nanoantenna structures possess significant high spatial frequency components over the planes near the nanoantennas. Due to the multiple scattering process, similar phenomenon is observed in "strongly scattering materials" [33, 54]. The multiple scattering process inside these complex structures have been harnessed to develop new applications [8]. Highly focused light beams are obtained when disordered samples are illuminated by wavefront engineered light source [34]. Nature inspired omnidirectional anti-reflection properties are reported in engineered random nanostructures [55]. Maximal energy transport through disordered media with the implementation of transmission eigenchannels have been investigated in [56]. In this research, new applications of disordered structures based on strongly coupled nanoantennas are investigated. It is shown that how optimizing the pattern of randomly configured nanoscale gold cubes leads to improved field localization in nanoantenna structures. Also I demonstrate that randomly configured gold nanoantennas can be used to realize orthogonal transmission channels, each associated with an optimized phase modulated incident field. This provides new avenues for signal processing in optical information systems where signals can be encoded and multiplexed taking advantage of the potentially large number of degrees of freedom provided by disordered systems.

To design such complex structures, a fast and accurate method is needed. Various schemes have been proposed to design and optimize nanoantennas. Exploiting the concept of antenna impedance, optical nanocircuit elements are used as nanoantenna loading to optimize their performance [57, 58]. Efforts aimed at the simplification of design procedures have led to a number of closed form solutions describing nanoantennas behavior in highly simple structures [59]. These methods are not sufficiently accurate for practical configurations of interest. Common full-wave analysis methods, on the other hand, are too slow [60, 61] to be directly combined with the efficient optimization algorithms, which are needed in the development of the design procedures, particularly for nanoantennas integrated with other nanostructures nearby. Therefore, there is a need for reliable design guidelines and practical optimization methods for nanoantennas geometrical parameters and configurations. Employing such methods facilitates the design and optimization of complex engineered media such as random nanostructures composed of arbitrary shape subwavelength building blocks.

The most important numerical techniques for the analysis of nanoantennas are those based on the FDTD (finite-difference time-domain) method, FEM (finite-element method), and MoM (method of moments) [62, 63, 64]. However, the design procedure of nanoantennas based on the FDTD and FEM, is a very time consuming process especially for those embedded in multilayer media. The reported approaches based on MoM also suffer from the complexity of the numerical evaluation of the required Green's functions appearing in the form of Sommerfeld's integrals.

In this work, the complex images technique [65] is used for fast and accurate computation of the required Green's functions of the layered media in the mixed potential integral equation (MPIE) formulation [66]. The nanoantennas in optical range of frequency should be modeled as three dimensional lossy dielectric objects. Both surface or volumetric integral equation formulations can be used in the modeling process. Although employing the surface integral equations will lead to less number of unknowns in the resultant matrix formulation, matrix elements must be computed for modified geometry at each iteration during the optimization process. On the other hand, in the volumetric approach, the impedance matrix for a fictitious antenna whose geometry covers the entire region the antenna can maximally occupy, is computed once. In this approach when the geometry of antenna is changed, the new antenna can be modeled without any computational efforts leading to significant reduction in total optimization time [67]. Therefore, in the method presented in this research, nanoantennas which are formed by a collection of nano-scale cubes are modeled by volume current density. The method of moments, based on complex images technique, is then used to solve for the unknown current distribution in the formulation. The method is quite fast and is used to design and optimize nanoantenna structures with complex geometries. The complex images technique has been utilized for various applications like microstrip antennas, nanolithography and photonic crystals [65, 68, 69]. In this technique, a closed form expression of Green's dyadics using complex images, is used to efficiently calculate the Sommerfeld's integrals which are known to have slowly convergent behaviors.

This chapter is organized as follows. In Section 2.2, I introduce a new approach for multiplexing signals. This is based on utilizing the optimized phase modulated incident fields which are associated with orthogonal transmission channels in disordered nanoantenna based structures. The design optimization method of these structures is also explained in this section. In Section 2.3, I describe a fast and convenient model to compute the electric field distribution in regions near and far from an illuminated nanoantenna structure with arbitrary shape. In the last Section, the numerical results are provided and discussed.

2.2 Orthogonal transmission channels

A general configuration of nanoantennas is shown in Fig. 2.1(a). Regions 1 and 2 are nonmagnetic dielectric media with known relative permittivities. The nanoantennas with arbitrary shape and material are placed on the interface between region 1 and region 2 (substrate). The antenna is illuminated by an electromagnetic wave with time-harmonic dependence $exp(j\omega t)$ coming from the region 2. It is observed that when an external electric field shines through nanoantenna structures, the field distribution over a plane at short distance above the nanoantennas contains high spatial frequency components leading to subwavelength high and low intensity regions. This property is more pronounced when the incident field is spatially modulated as it introduces even higher spatial frequencies in the diffracted fields. As mentioned earlier, thanks to the multiple scattering process a similar phenomenon occurs in disordered samples [33, 34]. Changing the phase distribution of the incident field over the input plane, the diffracted fields can be controlled leading to highly focused beams and improved imaging through disordered media [54]. A similar concept is applied here. The checker board plane (Fig. 2.1(a)) indicates the incident field distribution over the input plane at $z = 0$. This plane is divided into square pixels. Each pixel defines the amplitude and phase of a particular sample of incident field at the point $(x'_m,\, y'_n)$. The phase distribution over the checker board plane can be written in a matrix form which is called the phase matrix, $[\mathbf{\Phi}]$, with the element ϕ_{mn} being the phase of the incident field at the point $(x'_m,\, y'_n)$ over the input plane. The amplitude/phase-modulated electric field continues to propagate from the $z = 0$ plane towards the structure. If there is no modulation on the incident field, optimizing the configuration of nanoantennas for the constructive collective coupling between them can lead to improved field enhancement over a desired subwavelength region. On the other hand, phase modulations provide more degrees of freedom in controlling the diffracted fields. Unlike the commonly used disordered samples, the location of the nanoscale scatterers in the structure proposed here, are known. For a given nanoantenna configuration, the pixels close to the gold nanoantennas are chosen to excite the antennas. Amplitude of the incident field is assumed to be zero over the open regions, where the nanoantennas do not exist. First, a large number of simulations are

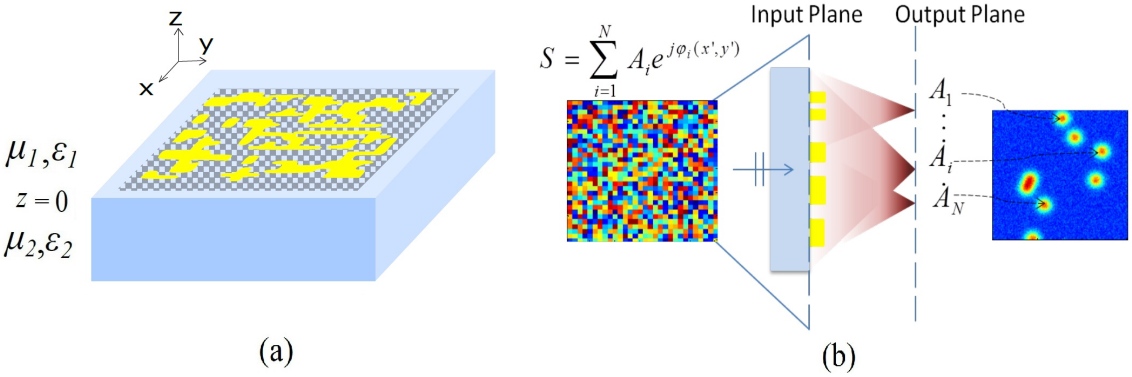

Figure 2.1: (a) Nanoantenna based structure in stratified medium. (b) Over the input plane, the 2D signal represents the combined information symbols using the phase distribution basis denoted by $e^{j\phi_i(x',y')}$. The nanostructure will demultiplex the information symbols, A_i s, over the output plane.

performed, where at each simulation the structure is illuminated with a randomly phase modulated incident electric field. Accumulating the diffracted fields over the output plane for all simulations, will indicate the regions (channels) where the diffracted fields are most likely to focus. A set of phase distributions $\{e^{j\phi_i(x',y')}; i = 1, ..., N\}$, each representing a particular transmission channel, can be defined for the given structure. The transmission channels associated with $e^{j\phi_M(x',y')}$ and $e^{j\phi_N(x',y')}$ are considered to be orthogonal if their images over the output plane have zero or minimal overlap. Using the phase distribution basis, the information symbols A_i, can be encoded and combined to form a 2D signal $S = \sum_{i=1}^{N} A_i e^{j\phi_i(x',y')}$, which is a complex (amplitude and phase) field distribution on the input plane $z = 0$. For a given nanostructure, the aforementioned phase distributions are chosen in such a way that the incident field with complex distribution (S) will be mapped onto disjoint spots over the output plane (Fig. 2.1(b)). Each spot represents a localized transmission channel carrying the corresponding information symbol.

As it is clear, the design and optimization of these complex structures require the development and application of a fast and accurate model. The proposed design procedure involves two steps. The first step is the computation of the matrix elements in the method of moments which takes into consideration all possible interactions between coupled nanoantennas in any possible configuration. The second step is the combination of the accurate developed model with a suitable optimizer. The developed method will be used to solve two classes of problems. The first class involves geometrical optimization of the nanostructures to maximize their efficiency. It is shown that strongly coupled nanoscale scatterers can improve the field localization in nanoantennas. The second class of problems deals with finding the optimized sources for a given structure. It is shown that for a pattern of randomly configured nanoantennas, the orthogonal transmission channels can be realized through exciting the optimized sources.

2.3 Formulation of the problem

In this section I present a fast and accurate analysis method for a general configuration of nanoantennas. The method as described below, is based on complex images representation of dyadic Green's functions, which will be used in the method of moments.

Fig. 2.1(a) shows a general configuration of nanoantennas illuminated by an electromagnetic wave with time-harmonic dependence $exp(j\omega t)$ coming from the region 2. The total electric field can be described by the magnetic vector potential ($\mathbf{A}$) and the electric scalar potential (φ) as

$$\mathbf{B} = \nabla \times \mathbf{A} - \frac{\nabla \times \mathbf{E}_{inc}}{j\omega}, \ \mathbf{E} = -j\omega\mathbf{A} - \nabla\varphi + \mathbf{E}_{inc}, \tag{2.1}$$

where $\mathbf{E}_{inc}$ denotes the incident field which satisfies the Maxwell's equations in the layered media in the absence of nanoantennas. Replacing the nanoantennas by the volume current $\mathbf{J}_{eff}$, one can formulate the problem in terms of the Green's functions for a two-layer media. To this end, the governing equations of the magnetic vector potential and the electric scalar potential in the two layers are written as

$$\begin{gathered} \nabla^2\mathbf{A} + k_n^2\mathbf{A} = -\mu\mathbf{J}^n_{eff}, \quad k_n^2 = \omega^2\mu\epsilon_0\epsilon_{rn}(n=1,2) \\ \mathbf{J}^n_{eff} = j\omega\epsilon_0(\epsilon_r - \epsilon_{rn})\mathbf{E}, \end{gathered} \tag{2.2}$$

and

$$\nabla.\mathbf{A} = -j\omega\mu\epsilon_0\epsilon_r\varphi, \tag{2.3}$$

respectively, where k_n is the wavenumber of the nth layer, ϵ_r is the relative electrical permittivity of the nanoantenna, and Eq. 2.3 is the Lorentz gauge condition. Thus, the total electric field in each region can be obtained through the mixed potential integral equation (MPIE) as

$$\mathbf{E} = -j\omega \int_{v'} \bar{\bar{\mathbf{G}}}^{mn}_{\mathbf{A}}(\mathbf{r},\mathbf{r}').\mu\mathbf{J}^n_{eff}(\mathbf{r}')dv' - \nabla \int_{v'} G^{mn}_q(\mathbf{r},\mathbf{r}')\rho^n_v(\mathbf{r}')dv' + \mathbf{E}_{inc}, \tag{2.4}$$

where the integration is carried out over the effective volume current areas, i.e. the antenna regions. $\bar{\bar{\mathbf{G}}}_{\mathbf{A}}^{mn}$ and G_q^{mn} denote the dyadic Green's function of $\mathbf{A}$ and the Green's function of φ, respectively, observed in the mth layer due to an electric dipole located in the nth layer of the two-layer stratified media shown in Fig. 2.1 and $\rho = -\nabla'.\mathbf{J}/j\omega$ is the charge density. I apply the Sommerfeld choice for the vector potential Green's function , that is

$$\bar{\bar{\mathbf{G}}}_{\mathbf{A}}^{mn} = \begin{pmatrix} G_{xx}^{mn} & 0 & 0 \\ 0 & G_{yy}^{mn} & 0 \\ G_{zx}^{mn} & G_{zy}^{mn} & G_{zz}^{mn} \end{pmatrix}, \tag{2.5}$$

where G_{uv}^{mn} denotes the u component of the vector potential Green's function observed in the mth layer due to a v-directed electric dipole source located in the nth layer. Using the Fourier transform, one can express $\bar{\bar{\mathbf{G}}}_{\mathbf{A}}^{mn}$ and G_q^{mn} as

$$\bar{\bar{\mathbf{G}}}_{\mathbf{A}}^{mn}(\mathbf{r},\mathbf{r}') = \frac{1}{(2\pi)^2}\iint\limits_{-\infty}^{+\infty} \frac{\tilde{\bar{\bar{\mathbf{G}}}}_{\mathbf{A}}^{mn}(k_\rho; z, z')}{2jk_{zn}} exp(-j\mathbf{k}^t.\mathbf{R}^t)dk_x dk_y, \tag{2.6a}$$

$$G_q^{mn}(\mathbf{r},\mathbf{r}') = \frac{1}{(2\pi)^2}\iint\limits_{-\infty}^{+\infty} \frac{\widetilde{G}_q^{mn}(k_\rho; z, z')}{2jk_{zn}} exp(-j\mathbf{k}^t.\mathbf{R}^t)dk_x dk_y, \tag{2.6b}$$

where $\mathbf{R}^t = (x - x')\hat{\mathbf{x}} + (y - y')\hat{\mathbf{y}}, k_\rho = \sqrt{k_x^2 + k_y^2}, \quad k_{zn} = \sqrt{k_n^2 - k_\rho^2}, \quad \mathbf{k}^t = k_x\hat{\mathbf{x}} + k_y\hat{\mathbf{y}}$. $\tilde{\bar{\bar{\mathbf{G}}}}_{\mathbf{A}}^{mn}/2jk_{zn}$ and $\widetilde{G}_q^{mn}/2jk_{zn}$ are the spectral domain representation of the dyadic Green's function of $\mathbf{A}$ and the Green's function of φ, respectively. Since the antenna is located in the first layer (Fig. 2.1), we just need to compute the spectral domain Green's functions for the source points located in this layer ; i.e., for m=1 and n=1, $\tilde{\bar{\bar{\mathbf{G}}}}_{\mathbf{A}}^{mn}$ is given by

$$\widetilde{G}_{xx}^{11} = \widetilde{G}_{yy}^{11} = exp(-jk_{z1}|z - z'|) + Aexp(-jk_{z1}(z + z')), \tag{2.7a}$$

$$\widetilde{G}_{zx}^{11} = -jk_x Bexp(-jk_{z1}(z + z')), \tag{2.7b}$$

$$\widetilde{G}_{zy}^{11} = -jk_y Bexp(-jk_{z1}(z + z')), \tag{2.7c}$$

$$\widetilde{G}_{zz}^{11} = exp(-jk_{z1}|z - z'|) + Cexp(-jk_{z1}(z + z')), \tag{2.7d}$$

where

$$A = \frac{k_{z1} - k_{z2}}{k_{z1} + k_{z2}}, \tag{2.8a}$$

$$B = \frac{2jk_{z1}(\epsilon_1 - \epsilon_2)}{(k_{z1} + k_{z2})(\epsilon_2 k_{z1} + \epsilon_1 k_{z2})}, \tag{2.8b}$$

$$C = \frac{\epsilon_2 k_{z1} - \epsilon_1 k_{z2}}{\epsilon_2 k_{z1} + \epsilon_1 k_{z2}}. \tag{2.8c}$$

According to Eq. 2.3 and the direction of electric dipole source, for m=1 and n=1, $\tilde{G}_q^{mn}$ s are obtained and chosen as

$$\widetilde{G}_{qx}^{11} = \widetilde{G}_{qy}^{11} = \frac{(exp(-jk_{z1}|z - z'|) + Dexp(-jk_{z1}(z + z')))}{\epsilon_1}, \tag{2.9a}$$

and

$$\widetilde{G}_{qz}^{11} = \frac{(exp(-jk_{z1}|z - z'|) - Cexp(-jk_{z1}(z + z')))}{\epsilon_1}, \tag{2.9b}$$

for x-(y-) and z- directed electric dipole source, respectively, where

$$D = \frac{(k_{z1} - k_{z2})(\epsilon_2 k_{z1} + \epsilon_1 k_{z2}) - 2k_{z1}^2(\epsilon_2 - \epsilon_1)}{(k_{z1} + k_{z2})(\epsilon_2 k_{z1} + \epsilon_1 k_{z2})}. \tag{2.10}$$

The coefficients A through D are obtained such that the continuity of tangential components of electric and magnetic fields are satisfied over the interface of two media and the Eq. 2.2 and Eq. 2.3 hold true. In general, there is no closed form solution for the spatial Green's functions given by Eq. 2.6, where the numerical evaluation for all possible source and field points is a very time consuming process. This is one of the major challenges in solving the MPIE (Eq. 2.4) for the unknown current distribution $\mathbf{J}_{eff}$. Therefore, the complex images technique is used to derive a closed form representation of the Green's functions. To this end, the spectral domain Green's functions given by Eq. 2.7 and Eq. 2.9 are approximated by a finite summation of complex exponential functions. Employing the 3D Sommerfeld's identity given in Eq. 2.13, the Green's functions of the stratified medium will be reduced to a closed form summation of complex terms each representing an electric dipole radiating in a homogenous unbounded area. The amplitudes and coordinates of these sources can assume complex values. The generalized pencil-of-function (GPOF) method [70] is used to expand the spectral domain functions in terms of complex exponential series. This is done by choosing a suitable path, determined by a real variable t, in the k_{zn} plane so that simpler path integration will provide an accurate approximation for the original Sommerfeld's integral. To achieve sufficient accuracy, different approximation paths can be chosen depending on the observation point distance to source. We place the complex images in region 1 and to make more accurate approximations, appropriate

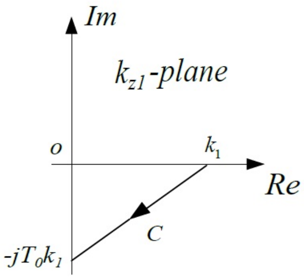

Figure 2.2: Approximation path in k_{z1} plane.

paths can be selected in the k_{z1} plane. Fig. 2.2 shows a typical path which is denoted by C. Each path is determined by a certain value of the real parameter t as

$$k_{z1} = k_1[-jt + (1 - t/T_0)], \quad 0 \leq t \leq T_0 \tag{2.11}$$

where T_0 is the truncation point with respect to k_1. If $\tilde{G}$ represents the spectral domain functions introduced in Eq. 2.8 and Eq. 2.10, they are approximated along the path C with a finite summation of exponentials, i.e.

$$\tilde{G}(k_{z1})\big|_C \approx \sum_{n=1}^{N_{\tilde{G}}} a_{n\tilde{G}} exp(k_{z1} b_{n\tilde{G}}). \tag{2.12}$$

The complex coefficients $a_{n\tilde{G}}$ and $b_{n\tilde{G}}$ are obtained by the GPOF method. Table 2.1 gives the typical values of the parameters used for approximating the spectral domain functions A through D in Eq. 2.8 and Eq. 2.10. In order to achieve a desired approximation error in Eq. 2.12, certain values of $N_{\tilde{G}}$ and T_0 will be selected. Substituting Eq. 2.12 in Eq. 2.7 and Eq. 2.9, the spatial Green's function will be reduced to a closed form summation utilizing the following 3D Sommerfel's identity,

$$\frac{exp(-jk|\mathbf{r} - \mathbf{r}'|)}{4\pi|\mathbf{r} - \mathbf{r}'|} = \int_{-\infty}^{+\infty} \frac{exp(-jk_z|z - z'|)}{2jk_z} H_0^2(k_\rho(|\rho - \rho'|)k_\rho dk_\rho, \tag{2.13}$$

where $|\rho - \rho'| = [(x - x')^2 + (y - y')^2]^{1/2}$ and $k = [k_\rho^2 + k_z^2]^{1/2}$.To demonstrate the accuracy of the complex images Green's function, comparison is made with the numerical integration of the spectral Green's function in Fig. 2.3. Perfect agreement is observed over a wide range of distances which validates the accuracy of our method in finding electromagnetic fields from the near- to far-field regions. Using the typical values of Table 2.1, the maximum and average values of the error between the approximate Green's functions and the accurate numerical integrations will be 0.5% and less than 0.01%, respectively.

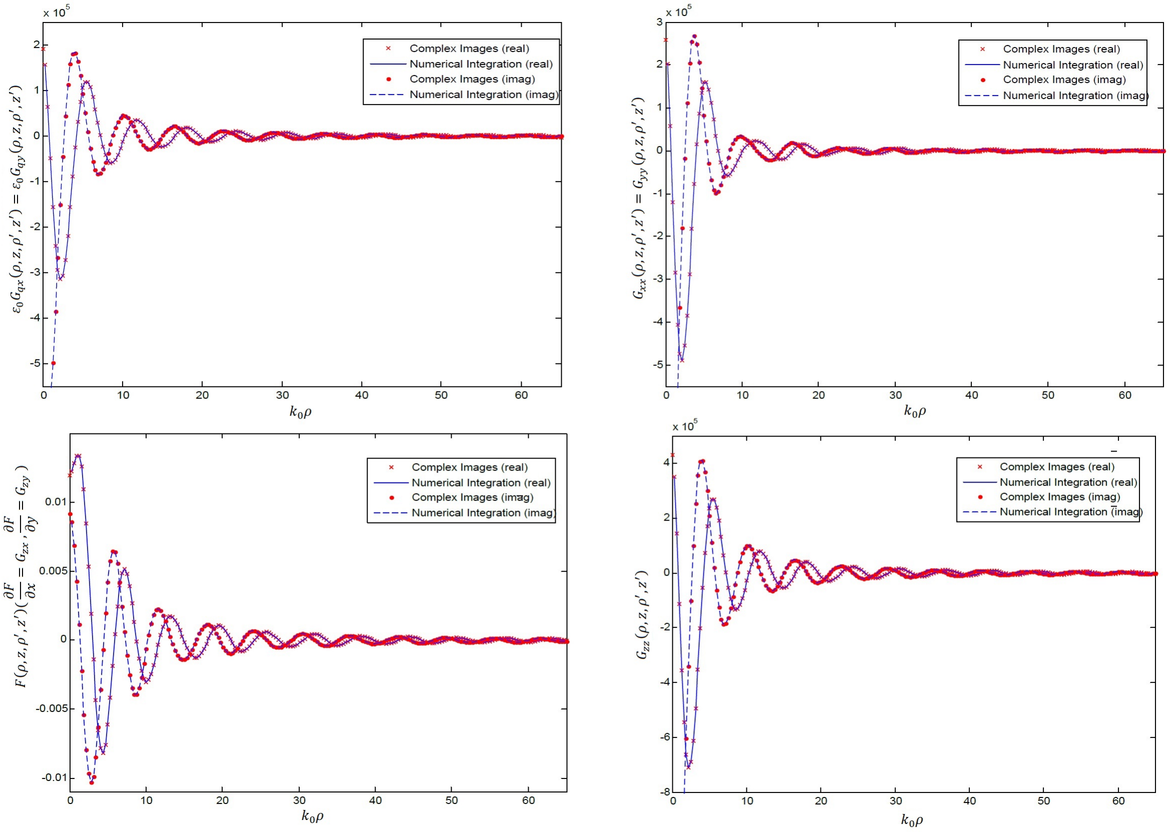

Figure 2.3: Complex images Green's functions versus numerical integration for $z = 0$ when source is located at $z' = 60\ nm$ over glass substrate ($n = 1.5$).

Table 2.1: Parameters used in approximating the Green's functions. For $N_{\tilde{G}}$, the first number from left is the number of exponential terms required for only near field approximation, the second is for near and intermediate field and the last is for near to far field approximation.

Green's Function	**Coefficients**	$N_{\tilde{G}}$	T_0	Region of images
$\widetilde{G}_{xx}^{11}, \widetilde{G}_{yy}^{11}$	A	4,8,20	1.9596	k_{z1}
$\widetilde{G}_{zx}^{11}, \widetilde{G}_{zy}^{11}$	B	5,8,20	3.0397	k_{z1}
$\widetilde{G}_{zz}^{11}, \widetilde{G}_{qz}^{11}$	C	4,8,20	3.0397	k_{z1}
$\widetilde{G}_{qx}^{11}, \widetilde{G}_{qy}^{11}$	D	4,8,20	3.0397	k_{z1}

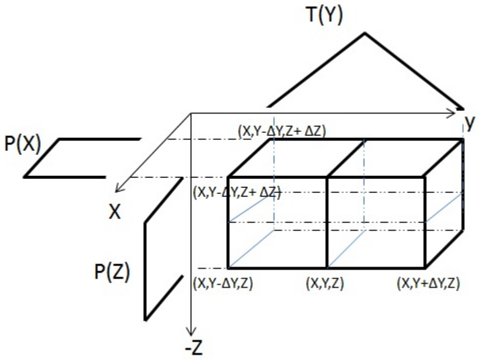

Figure 2.4: The basis function used to expand the y-directed currents.

The integral equation 2.4 can now be solved by employing the MoM. I use the rectangular and triangular functions to segmentize the different components of electric field in the source region 1 as

$$\mathbf{E} = \sum_{m=1}^{M} \alpha_m BF_{xm}\hat{\mathbf{x}} + \sum_{n=1}^{N} \beta_n BF_{yn}\hat{\mathbf{y}} + \sum_{l=1}^{L} \gamma_l BF_{zl}\hat{\mathbf{z}} \qquad , \tag{2.14}$$

where the electric field is expanded in terms of the basis functions $BF_{xm} = T_m(x)P_m(y)P_m(z)$, $BF_{yn} = P_n(x)T_n(y)P_n(z)$, and $BF_{zl} = P_l(x)P_l(y)T_l(z)$ and P and T are rectangular and triangular functions, respectively, used to segmentize the source region. From the physical point of view, the source region is divided into cubic charge elements where the current segments are located between these elements in all three directions. Fig. 2.4 shows the basis function used to expand the y-directed currents. This choice for basis functions will significantly reduce the number of unknowns in the resulting matrix equation. Substituting

Eq. 2.14 in Eq. 2.4 and employing the Galerkin technique [71], we will have $M + N + L$ equations for the unknown coefficients in Eq. 2.14, converted to the matrix form as

$$[S\_\,A]\begin{bmatrix}\alpha\\ \beta\\ \gamma\end{bmatrix} = (\Delta_x\Delta_y\Delta_z)[\mathbf{E}_{inc}] + \begin{bmatrix}\mathbf{Z}_{xx} & \mathbf{Z}_{xy} & \mathbf{Z}_{xz}\\ \mathbf{Z}_{yx} & \mathbf{Z}_{yy} & \mathbf{Z}_{yz}\\ \mathbf{Z}_{zx} & \mathbf{Z}_{zy} & \mathbf{Z}_{zz}\end{bmatrix}\begin{bmatrix}\alpha\\ \beta\\ \gamma\end{bmatrix}. \tag{2.15}$$

$[S\_\,A]$ is the matrix representation of the inner product of the electric field expanded in Eq. 2.14 by itself whose components are all zero with the exception for the elements related to the self and adjacent parallel current segments which can be easily shown that are equal to $\frac{2}{3}\Delta_x\Delta_y\Delta_z$ and $\frac{1}{6}\Delta_x\Delta_y\Delta_z$ respectively. Δ_x, Δ_y, and Δ_z are the side length of the cubic charge element along x-, y-, and z- direction respectively. For the impedance matrix we obtain

$$\begin{gathered}Z_{uu,rc} = \\ \omega^2\mu\epsilon_0(\epsilon_r - \epsilon_{rn})\int_{BF_{ur}}\int_{BF_{uc}} G^{11}_{uu}(\mathbf{r},\mathbf{r}')T_r(u)T_c(u')dvdv \\ -\frac{\epsilon_0(\epsilon_r - \epsilon_{rn})}{(\Delta_u)^2}\int_{BF_{ur}}\int_{BF_{uc}} G^{11}_{qu}(\mathbf{r},\mathbf{r}')(P^-_r(u) - P^+_r(u))(P^-_c(u') - P^+_c(u'))dvdv'\end{gathered} \tag{2.16a}$$

for $u = x, y, z$,

$$\begin{gathered}Z_{uw,rc} = \\ -\frac{\epsilon_0(\epsilon_r - \epsilon_{rn})}{\Delta_u\Delta_w}\int_{BF_{ur}}\int_{BF_{wc}} G^{11}_{qw}(\mathbf{r},\mathbf{r}')(P^-_r(u) - P^+_r(u))(P^-_c(w') - P^+_c(w'))dvdv'\end{gathered} \tag{2.16b}$$

for $u = x, y$, $w = x, y, z$ and $u \neq w$,

$$\begin{gathered}Z_{zw,rc} = \\ -\frac{\epsilon_0(\epsilon_r - \epsilon_{rn})}{\Delta_z\Delta_w}\int_{BF_{zr}}\int_{BF_{wc}} G^{11}_{qw}(\mathbf{r},\mathbf{r}')(P^-_r(u) - P^+_r(u))(P^-_c(w') - P^+_c(w'))dvdv' \\ +\frac{\omega^2\mu\epsilon_0(\epsilon_r - \epsilon_{rn})}{\Delta_w}\int_{BF_{zr}}\int_{BF_{wc}} F(\mathbf{r},\mathbf{r}')T_r(z)(P^-_c(w') - P^+_c(w'))dvdv',\end{gathered} \tag{2.16c}$$

for $w = x, y$. In these equations, $(P^-(u') - P^+(u'))/\Delta_u$ is the derivative of the triangular function $T(u)$ and $G^{11}_{zu} = -\partial F/\partial u'$ for $u = x$ and y. Rewriting Eq. 2.15 gives

$$[\mathbf{Z}_{antenna}]\begin{bmatrix}\alpha\\ \beta\\ \gamma\end{bmatrix} = [\mathbf{E}_{inc}]. \tag{2.17}$$

α, β, and γ are vectors representing the corresponding variables used for **E** field expansion in Eq. 2.14. This equation is the discretized version of MPIE (Eq. 2.4), where the elements of the antenna impedance matrix, $[\mathbf{Z}_{antenna}]$, represent the electromagnetic interaction between any two cells of the antenna. The antenna impedance matrix, therefore, depends on the shape of metallic pattern. This dependence can be expressed in this form

$$[\mathbf{Z}_{antenna}] = [Pattern]^T[\mathbf{Z}_{region}][Pattern], \tag{2.18}$$

where $[\mathbf{Z}_{region}]$ is the impedance matrix of a fictitious antenna whose metallic pattern covers the entire region the antenna can maximally occupy and $[Pattern]$ is a matrix, which defines the actual shape of one particular antenna. This is a convenient formulation for the antenna shape optimization, because the antenna matrix elements only depend on the positions of two particular cells of the antenna and the $[\mathbf{Z}_{region}]$, which is computed once, contains these values for all possible positions of the antenna cells. Once $[\mathbf{Z}_{region}]$, which only depends on the multilayer properties, wavelength, size of the cell, and the size of the region, is known the $[\mathbf{Z}_{antenna}]$ for each particular antenna geometry is obtained from simple matrix multiplication of Eq. 2.18. Then, to find the near-field of a particular antenna shape, $[\mathbf{Z}_{antenna}]$ is inverted to solve Eq. 2.17 for the unknown coefficients α, β, and γ. These coefficients are used in Eq. 2.2 to find the volume currents, which are then used in Eq. 2.4 to find the field at desired points above the structure.

2.4 Numerical results

In this section, we apply our proposed method to the problem of simulating the near field of an illuminated arbitrary shape nanoantenna configuration. First, the problem of maximizing the near field localization of a nanoantenna structure for a given incident field is considered. Next, we consider the problem of finding the orthogonal transmission channels of a randomly configured gold nanopattern. The wavelength of the incident electric field is assumed to be 633 nm. The regions 1 and 2 of Fig. 2.1(a) are air and glass, respectively. The antenna is made up of gold with refractive index of $n_{gold} = 0.1726 - 3.4218j$ at $\lambda = 633nm$ [72] and the refractive index of glass is taken as $n_{glass} = 1.5$. To validate the accuracy of our proposed method, we consider a square shape antenna illuminated by an x-polarized plane-wave with unit amplitude in glass, propagating along z-axis which hits the antenna from the substrate (region 2) (Fig. 2.1). The side length and the thickness of antenna are 300 nm and 40 nm respectively. The electric field distribution at z=60 nm above substrate is obtained by a finite element method solver, HFSS (ANSYS) and is compared with the results of our method in Fig. 2.5.

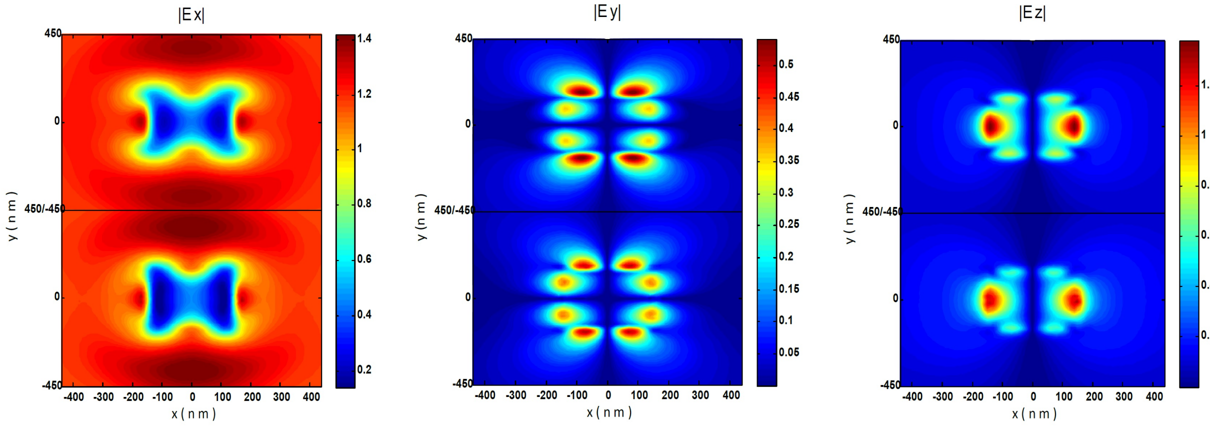

(a) (b) (c)

Figure 2.5: Electric Field distribution at the plane $z = 60\ nm$ above substrate when the square shape antenna (side length of 300 nm and thickness of 40 nm) is illuminated from substrate by an x-polarized electric field propagating along z-axis with unit amplitude in glass and $\lambda = 633\ nm$.(a) absolute value of x-component of electric field. The top half of the image is the result of our method and the bottom half is that of FEM obtained by HFSS.(b)-(c) are for y-and z- components of electric field respectively.

The root mean square errors for the results of two methods which are computed through

$$Error = \sqrt{\frac{\iint_{OutputPlane} |E_1 - E_2|^2 ds}{\iint_{OutputPlane} |E_{avg}|^2 ds}}, \tag{2.19}$$

are less than 0.8 % for the x-component, and 3% for the y- and the z-component of electric field. E_1 and E_2 are the absolute values of corresponding electric field components obtained by two methods. $|E_{avg}|$ is the average value of E_2 (the finite element method) over the output plane.

2.4.1 Field enhancement

Now we investigate the problem of field localization using a structure consisting of nanoscale scatterers optimally arranged on a glass substrate . The goal of optimizer is to maximize the field intensity at $x = 0$, $y = 120\ nm$, and $z = 60\ nm$ above the substrate. The structure is spanned over a square shape area which is divided into 225 smaller square cells with the side length of 20 nm and the thickness of 40 nm. Considering the fact that the cost function of optimization problem has several local minima, a global optimization algorithm should be used. The simulated annealing (SA) algorithm with parameters listed in Table 2.2 is employed to find an optimized pattern for a given excitation field which is assumed to be an x-polarized plane-wave propagating along z-axis hitting the structure from beneath. The suggested parameters in Table 2.2 are obtained after some test optimizations. For larger structures the parameters should be changed for better exploration of the new larger solution space. This can be done by increasing the starting temprature, T_0, or increasing the temprature reduction coefficient, r_T, or the combination of both. Increasing N_T, also, allows better exploration of the solution space in larger problems. For small problems, however, these changes lead to longer optimization time with no significant gain in the performance of optimization algorithm in finding the optimum solution.

Table 2.2: Parameters of Simulated Annealing Algorithm. T_0, starting temperature; N_T , test for temperature reduction; N_ϵ, number of successive temperature reductions to test for termination; r_T , temperature reduction coefficient; ϵ, termination criterion [1].

T_0	N_T	N_ϵ	r_T	ϵ
2	5	4	0.5	1e-5

Each cell of structure is defined as a variable which could have a value of one if it is filled with gold rectangular cubic or zero if it is filled with air. To start the optimization, a large number of sparse random patterns are generated and the field intensity at the desired point is computed and recorded. The best pattern is chosen as an initial point in the optimization. The solution to the optimization problem may not be unique. As an example, we choose the point of interest at some height over the center of defined region for antenna. For this particular case, we investigate symmetric and asymmetric solutions with respect to the y axis. The obtained optimized antennas are shown in Fig. 2.6(a). The total electric field intensity when the optimized antennas are illuminated by the aforementioned plane wave is depicted in Fig. 2.6(c). Comparison of this field intensity with that of the incident field in the absence of nanoantenna shows a maximum field enhancement of about 14.15 dB for both antennas. As it is shown, the symmetric antenna contains less number of gold cubics than the asymmetric one, but the patterns are similar near the points of maximum field. This indicates the field enhancement is mostly influenced by the gold cubic cells located near the gap of the resonating antenna below the point of interest. Antenna current distribution near the focal points (Fig. 2.6(b)) reveals the combination of dipolar electric mode and dipolar magnetic mode of split ring resonator leading to the field

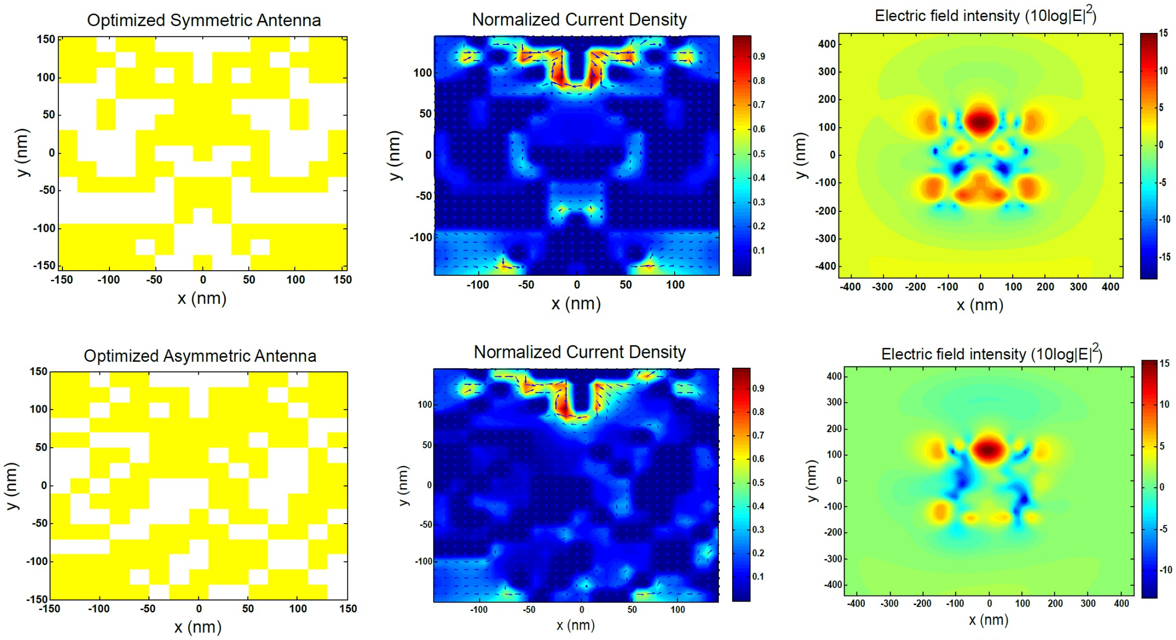

(a) (b) (c)

Figure 2.6: (a) The optimized antenna configurations, (b) an overlay of current density and direction inside antenna and (c) the obtained field intensity at the plane $z = 60\ nm$ above substrate, when the optimized antenna is illuminated from substrate by an x-polarized electric field propagating along z-axis with unit amplitude in glass and $\lambda = 633\ nm$.

intensity maximization. Similar situation has also been observed in [60]. From the antenna current distribution, shown in Fig. 2.6(b), it is also observed that some regions contribute much less to the total electric field enhancement at the desired point. Removing the gold cubic cells in these regions, obviously has negligible effect on the field enhancement, while can reduce the complexity of the antenna. However, this should be done carefully as there exist C-shape sections (Fig. 2.7(a)), whose removal can significantly decrease the collective coupling to the main resonator below the focal point leading to much lower field intensity than the original pattern.

This method is now applied to the symmetric antenna configuration. As it is illustrated in Fig. 2.7(b), although the field intensity increases in the other areas, the reduced structure has a maximum field enhancement almost identical to the original one.

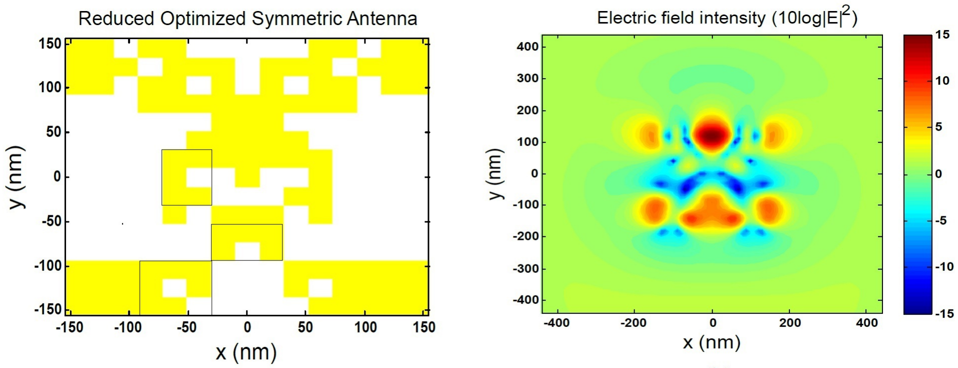

(a) (b)

Figure 2.7: (a) The reduced version of the optimized symmetric antenna configuration. Also shown are three of C-shape sections which have significant contribution to the near field localization at the focal point.(b) the field intensity while the antenna is illuminated.

2.4.2 Orthogonal transmission channels

In this section, we investigate the problem of phase modulated electromagnetic field interaction with random gold nano patterns. For a given structure, depending on the configuration and the type of excitation used to illuminate the structure, the number of realizable channels can vary. In the present work, we are interested in realizing localized orthogonal channels. The electric field over the output plane for this type of channels are more focused over smaller regions as opposed to the non-localized channels where the diffracted fields expand over larger area. A random pattern which consists of 400 randomly chosen cubic cells out of a total of 900 cells covering the entire defined region is considered like the one shown in Fig. 2.8(a). The side length and the thickness of each cell is 10 nm and 40 nm respectively.

To identify the possible regions to be considered as output channels we perform a large number of simulations. In each simulation the structure is illuminated with an initially x-polarized incident electric field which undergoes phase modulation at each defined pixel with a value randomly drawn from the uniform distribution on the interval $[0, 2\pi]$. The size of each pixel is 10nm by 10 nm. Accumulating the absolute value of the total electric fields indicates the regions where the diffracted fields are most likely to focus. Fig. 2.8(b) shows the result for the x-component of the diffracted electric fields. The high intensity regions are associated with resonating local nanoantennas and are candidates for the localized transmission channels. As it is shown before, the value of field near a resonating local nanoantenna is mostly influenced by the nearby elements. Owing to the accumulation of

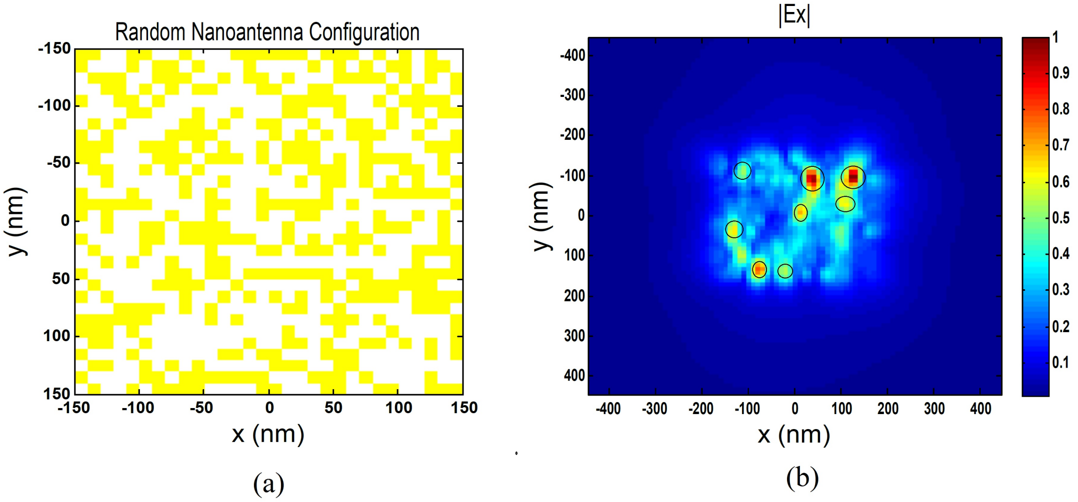

(a) (b)

Figure 2.8: (a) Strongly coupled nanoantennas with random configuration.(b) Specified spots can represent possible transmission channels.

phase differences of diffracted fields due to the phase modulation over the input plane and the coupling between elements, the value of electric field can become negligible at other channel regions leading to the realization of orthogonal transmission channels. This process can be systematically carried out through the optimization process. On the other hand, choosing low intensity regions leads to non-localized transmission channels. Not being associated with any local nanoantenna, the diffracted fields expand over larger area. Eight high intensity spots (Fig. 2.8(b)) are chosen to represent the localized orthogonal channels. The optimizer goal is set to find the optimum phase value for each pixel so that when they are applied to the incident field, we get a maximum value for the ratio of the x-component of electric field at the specified spot, associated with each channel, to that at the other spots. This optimization is performed for all channels. Similar to the previous problem, we apply the SA algorithm for optimization. The parameters used here are similar to Table 2.2 except that $T_0 = 0.1$, and $N_T = 10$. In addition to the parameters mentioned in Table 2.2, another parameter is used here for test of step variation which is $N_S = 10$. Fig. 2.9 shows the x-component of the total electric field across the output plane above the structure when each channel is excited by an optimized phase modulated incident field separately. The isolation obtained between channels are better than -40 dB for all cases. The optimized phases corresponding to orthogonal channels are depicted in Fig. 2.10. Table 2.3 shows the average values of the isolation between channels when the SNR (signal-to-noise ratio) is 40 dB. As can be seen, some channels (the 5th,7th, and 8th column) are less sensitive

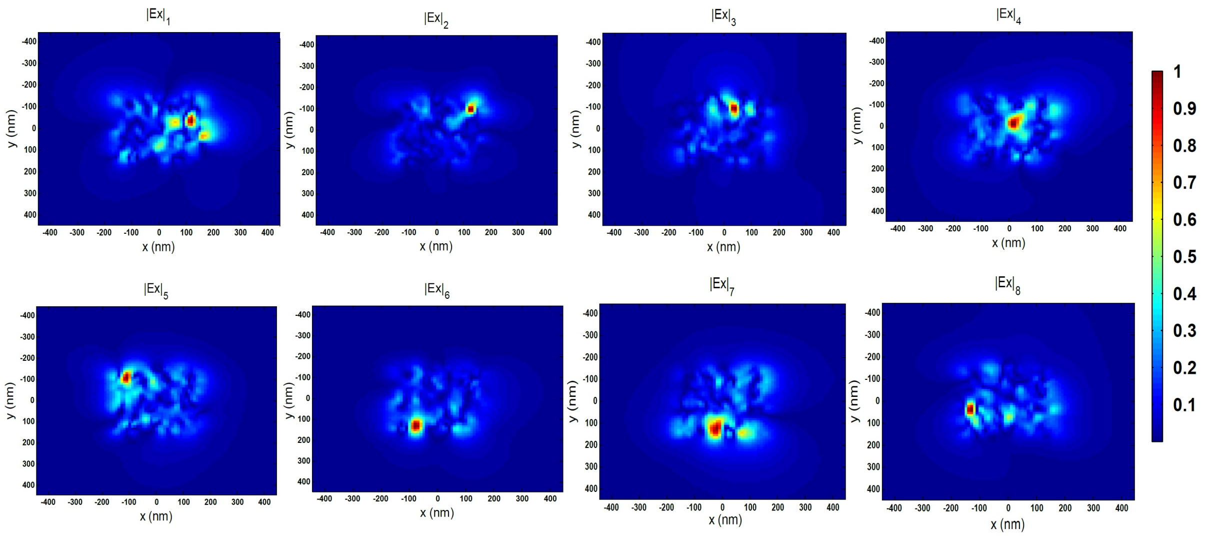

Figure 2.9: The total normalized electric field (x-component) distribution at $z = 60\ nm$ above the structure when the incident x-polarized electric field is modulated with the phase matrix associated with each channel.

to the noise. This mainly depends on the number, the configuration and the orientation of elements near each channel. Reducing the SNR to 20 dB will cause the isolation level between channels to decrease by approximately 20 dB. For SNRs of 15 dB and lower, there is no guarantee that all the channels are isolated and the field distributions of Fig. 2.9 are no longer preserved.

Table 2.3: Channels isolation in the presence of noise. Each row indicates the selected channel and the columns are the average values of the isolation (dB) when the phase matrix (SNR=40 dB) corresponding to the selected channel is applied.

Channels	1	2	3	4	5	6	7	8
1	-	-31.45	-32.27	-34.27	-37.33	-33.60	-36.02	-35.2
2	-42.95	-	-39.23	-39.4	-44.24	-39.48	-41.64	-43.16
3	-40.75	-36.69	-	-39.12	-39.33	-39.01	-41.82	-39.87
4	-36.52	-33.60	-34.60	-	-38.71	-36.25	-38.30	-36.77
5	-37.29	-33.12	-33.78	-36.23	-	-34.63	-37.57	-37.76
6	-37.54	-34.14	-35.15	-38	-40	-	-39.48	-39.07
7	-36.92	-34.19	-34.91	-38.02	-40.53	-36.87	-	-39.05
8	-38.87	-35	-36.13	-38.02	-41.09	-37.31	-40.35	-

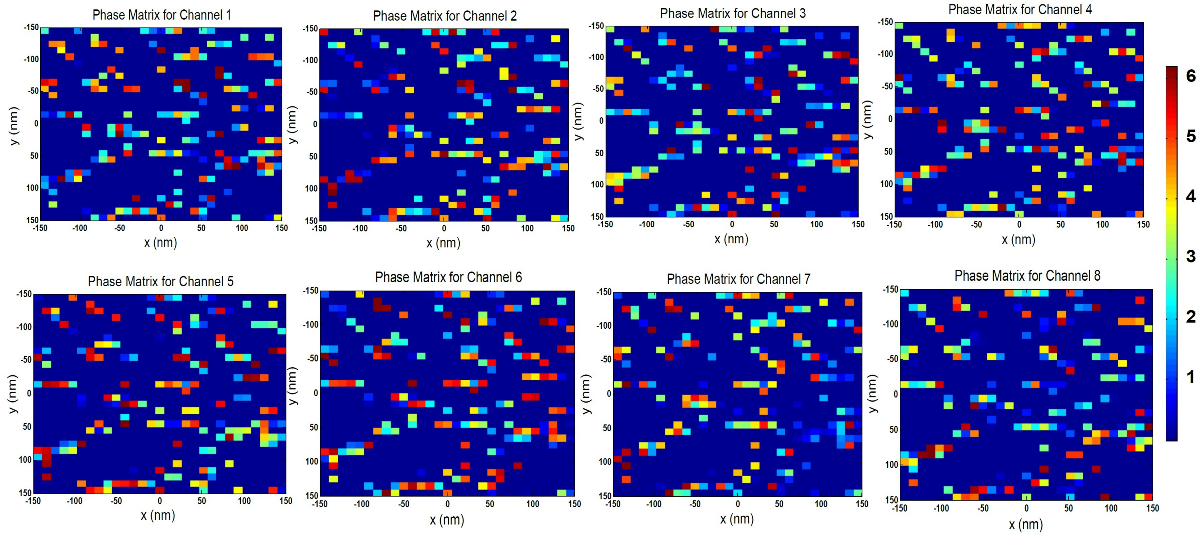

Figure 2.10: Phase matrix represents the optimized value for the phase distribution on the input plane. Applying each phase matrix, the diffracted field will have a focus in the corresponding spot for each transmission channel, while the value of field is negligible in other spots.

The proposed geometrical parameters correspond to what can be achieved with the state-of-the art fabrication techniques [73, 74]. All the computations are performed using MATLAB codes without implementing any parallel computation technique on a 3.2 GHz Core i5 CPU with 16GB RAM. For a good convergence of the field disrtribution over the output plane with less than 0.1 % error, the size of the segments should be less than $\frac{\lambda}{45}$. With the chosen grid size of $\frac{\lambda}{60}$, for a volume of $\frac{\lambda}{2} \times \frac{\lambda}{2} \times \frac{\lambda}{15}$, it takes about 7 hours to compute the MoM matrix elements. In the problem of geometrical optimization, the average time for computing the electric field intensity for a pattern with half of the entire area covered by gold is about 5 seconds. With near 17000 patterns chosen to solve the forward problems in the optimization process, it takes about 24 hours to obtain the optimized solution using SA algorithm. It is worth mentioning that the FEM computation time to solve one forward problem, i.e. the field intensity for one pattern, is about 30 minutes which is 360 times slower than our proposed method.

2.5 Conclusion

The analysis and design optimization of disordered nanoantenna structures are investigated. A new application of disordered systems was introduced. It is shown that orthogonal transmission channels can be employed to multiplex optical signals. An efficient and precise method to analyze and optimize the nanostructures in multilayered medium is proposed. The MPIE formulation is used to analyze the electromagnetic field interactions with these structures. Employing the complex images technique, the spatial Green's function computation is performed in an extremely fast and highly accurate manner. An effective combination of this fast and accurate solver with simulated annealing algorithm was applied to the design and optimization of the highly complex nanostructures. A nano gold pattern for maximizing the field intensity at a certain point near the antenna was successfully designed and optimized. For a given randomly configured nanoantennas, optimized phase modulated incident fields corresponding to orthogonal transmission channels were obtained.

Chapter 3

Freeform engineered disordered metalenses for super-resolution imaging and communication

Effective transmission of information through scattering media has been of great importance in imaging systems and beneficial to high capacity wireless communication. Despite numerous attempts to achieve high-resolution sub-diffraction-limited imaging through employing the engineered structures such as the so-called metamaterials or utilizing techniques like time reversal methods, the proposed ideas suffer from the fundamental limitations for design and practical realization. In this chapter, we investigate disorder-based engineered scattering structures and introduce a novel technique for achieving super-resolution based on designing and employing engineered all-dielectric medium. We show that disorder in the proposed design can be exploited to significantly modify the information content of scattered fields in the far-field region. Under the presence of the designed structures, using computational methods, signals associated with ultra sub-wavelength features of the illuminating sources can be enhanced and extracted from the far-field image. Not only can the presented approach lead to remarkable enhancement of resolution in such systems, but also orthogonal transmission channels are attainable when the closely-packed sources are excited properly. The latter provides a new scheme for encoding and multiplexing signals leading to the enhancement of information capacity in emerging information processing systems. The design procedure and physical constraints are studied and discussed.

3.1 Introduction

Diffraction limits the maximum resolution, which can be achieved to the order of the wavelength of light in conventional imaging systems. This is due to the limited capabilities in collecting the scattered high spatial-frequency components from the illuminated samples which render the reconstruction of sub-wavelength features impossible. Numerous attempts have been made to develop methods known as super-resolution techniques to overcome this limitation and push the boundaries of imaging capabilities into sub-diffractional regime. These attempts encompass the engineering of structured lenses, structured illuminating sources, and the development of computational algorithms which in combination with the proposed techniques have led to unprecedented achievements in the optical imaging systems. Capturing and amplifying the evanescent components of scattered fields, metamaterial-based structures break the diffraction barriers and achieve resolutions beyond those imposed by the diffraction of light [75, 76]. For these kinds of structures, however, the super-resolution features are satisfied only for a fixed transverse plane near the structure. In addition, the limitations imposed by practical fabrication techniques and material losses and imperfections restrict their effective implementation. Although some techniques achieve high resolution imaging by exploiting the nonlinear effects, the need for labeling or possessing nonlinear properties confines the application of these methods to certain groups of optical samples [77, 78]. Employing computational methods along with the optical imaging techniques such as structured illumination, on the other hand, provides new possibilities in extracting the sub-resolution information of samples. These breakthroughs are made possible through increasing the effective numerical aperture of the optical systems employing numerical algorithms like machine learning and without significant hardware modification [39, 79]. Relying on computational techniques, lens-less imaging systems provide a new scheme for optical imaging. The spatial coding realized by metallic nanostructured surfaces, for instance, has been used in combination with optimization algorithms to detect objects in on-chip lens-less imaging applications [80]. Despite using the visible light for imaging, the weak scattering signals of radiating objects, due to interaction with nanostructured surface, limit the maximum resolution which can be achieved to micro-scale ranges. The spectral content of radiated fields has also been used in other studies for post-numerical analyses. Examples include spectral encoding of spatial frequency, for the characterization of nanoscale structures, and interferometric spectroscopy used to quantify the statistics of refractive index fluctuations of random dielectric medium [81, 82, 83]. However, there are simplifying physical assumptions for the samples being imaged in these approaches, limiting their applications to certain type of materials such as weakly scattering objects. In a recent study, it has been shown that using speckle correlation, high quality diffraction-limited imaging can be achieved. The study has been conducted for both lens-less imaging systems and those with illuminated samples accompanied by scattering layer(s) [84, 85, 41]. This technique is based upon the observation that the speckle images formed by different radiating point sources have minimal correlation over the image plane. Calculating the autocorrelation of measured intensity gives the same result as if an ideal, aberration-free lens is employed to image the object. Phase retrieval algorithms can be used, in the next step, to obtain the object's image [86, 87]. Making use of scattering properties of highly scattering media to achieve higher resolution has also been proposed by other studies. For example, a TR (time-reversal) based technique shows that in a rich scattering medium and in the presence of highly scattering microstructures, the information capacity of a communication system can be increased while the receiver antennas are located at sub-wavelength distances from each other [42]. The requirement for having a rich scattering medium limits the application and the maximum achievable resolution by this type of methods. While these techniques are performed under the assumption that sufficient number of measurements is recorded over the interested region, it has been shown that, when combined with a suitable optimization algorithm, scattering medium can also improve the resolution of sparse images with fewer number of samples over the image plane [88]. In a similar approach, using optimization algorithms, the combination of broadband illuminating sources with resonant structures and/or disordered medium is employed to realize high resolution imaging [89, 90, 91]. Introducing a novel approach based on engineered scattering medium which is capable of imaging beyond the diffraction limit and investigating the fundamental limitations imposed by various physical parameters of imaging system are clearly needed. Our goal is directed at such an approach in this chapter.

Random systems exhibiting highly transmitting channels, known as open channels, have attracted considerable attention for creating new possibilities for a wide range of applications from biomedical imaging to energy-efficient ambient lighting and optical information systems [92, 93, 94, 95]. While their main goal has been to compensate for the effects of multiple-scattering through controlling the incident wave, and consequently, to increase the transmitted power through such media, our focus, in this work, is on taking advantage of scattering effects in electrically thin scattering structures to increase the number of transmitting channels which are capable of carrying information to the far-field region. This is done through decomposing signals into orthogonal channels (modes) and maximizing the transmitted power of the highest order mode to the receiver side. In this chapter, we reveal the possibility of extracting sub-wavelength information of illuminating sources from their far-field image distribution. To this end, we employ the SVD (singular value decomposition) technique to extract the information of all possible transmitting channels.

Our approach is based on modifying the higher orders transmission channels by introducing disorder-based engineered all-dielectric lens structures in front of the illuminated samples or transmitting sources. The presented method paves the way towards realizing structures with remarkably enhanced scattering features. This is done through following a systematic design approach where we exploit the high degrees of freedom inherent in disordered strongly scattering media. Our results demonstrate a significant improvement in achieved resolutions (very small fraction of the wavelength), and computational complexity, compared to similar approaches reported previously, which require using techniques like the employment of self-assembled nanolenses and large processing time for sub-wavelength sensing [96]. The introduced scattering structures are composed of dielectric scatterers and combine two major features. The first feature is the enhancement of the transmitted power of the highest order mode signals to the far field region due to the interaction of incident fields emitted from the illuminating sources with the dielectric objects. The illuminated dielectric objects re-radiate the incident electromagnetic waves which, in combination with the primary fields emitted from the sources, can lead to an average enhancement of the received power at the far field region. As demonstrated, the maximal transmission through lossless random structures can be achieved by minimizing the reflection [97]. In the present work, however, we directly maximize the transmitted power of interested modes emitted from the source region by optimizing the configuration of dielectric objects. The second feature is the reduction of the correlation between the radiated signals emitted from adjacent point sources which can be enhanced by exploiting the disorder realized by sub-wavelength dielectric inclusions. The point spread functions (PSF) of the proposed structured lenses possess modified space-variant property leading to significant reduction of correlation between the images formed by point sources located at sub-wavelength distances from each other. Based on the PSFs of radiating point sources and using the SVD technique, orthogonal basis vectors (modes) on both source (object) and image vector spaces can be obtained. The orthogonal basis vectors (modes) which we refer to as the orthogonal transmission channels can be used to expand the single-shot measured image to resolve the sub-diffractional features of objects. Moreover, these orthogonal basis vectors can be used to combine information signals at the transmitter and restore the information from the received signal at the receiver side. The improvement achieved for the resolution due to the scattering medium and the enhancement of the information capacity are studied and discussed. This chapter is organized as follows. In Section 2, we present the analysis and design procedure of the proposed structures. The proposed method is applicable to any type of scattering medium, however, without loss of generality, in this chapter we investigate scattering media composed of dielectric wires in more details. In Section 3, we apply our proposed method to design structures with modified scattering features and investigate how the presence of different designed structures affects the scattering properties of illuminating sources. The resultant improvements of features such as the resolution, and the maximum number of resolvable point sources, in a given imaging or communication system with a known SNR (signal to noise ratio) and numerical aperture (NA), are studied. The last Section is the conclusion.

3.2 Analysis and design of scattering features of disordered all dielectric medium

In this Section, the analysis and design of a disordered all-dielectric medium are explained. We consider a general configuration shown in Fig. 3.1. Dielectric cylinders with refractive index $\sqrt{\epsilon_r}$ and radius a are confined within a rectangular region. The structure is illuminated by a collection of point sources located over the source (object) region at a specific distance from the scattering medium. The transmitted fields are measured (amplitude and phase) at points over the image region which is located at a far distance from both the sources and the scattering structure.

3.2.1 The analysis

We employ a full-vectorial approach to rigorously solve the Maxwells equations and calculate the scattered field from the dielectric objects at an arbitrary location. To obtain the total electromagnetic field at any point in space, the incident, internal and scattered fields are expanded in terms of cylindrical harmonics for each dielectric cylinder and the boundary conditions are imposed on the surface of wires [98]. Assuming that the dielectric wires are infinite in y-direction, for a TM incident wave we can formulate the electromagnetic problem in terms of the y component of the electric field. The scattered field by a dielectric wire due to a unity amplitude plane wave incident at an angle ϕ_i can be written as

$$E^y = \sum_{m=-\infty}^{+\infty} j^{-m} C_m H_m^{(2)}(k_0\rho) e^{jm(\phi-\phi_i)}, \tag{3.1}$$

where C_m are the mode coefficients for the scattered fields and can be expressed as [99]

$$C_m = \frac{\frac{\eta_0}{\eta_d} J_m(k_0a) J'_m(k_da) - J'_m(k_0a) J_m(k_da)}{J_m(k_da) H_m'^{(2)}(k_0a) - \frac{\eta_0}{\eta_d} J'_m(k_da) H_m^{(2)}(k_0a)}. \tag{3.2}$$

Assuming that the radius of wires are much smaller than the wavelength of the fields in the free space and the dielectric medium, higher order modes can be neglected and only C_0 is used to describe the scattered fields. If we have 'L' number of dielectric wires, the incident waves exciting the k^{th} dielectric wire can be written as

$$E^y_{k,inc} = E^y_{externalsources}(\mathbf{r}_k) + \sum_{l=1,l\neq k}^{L} E^y_l(\mathbf{r}_k) = \sum_{n=1}^{N} s_n H_0^{(2)}(k_0|\mathbf{r}_k - \mathbf{r}_n|) + \sum_{l=1,l\neq k}^{L} E^y_l(\mathbf{r}_k), \tag{3.3}$$

where E^y_l denotes the y component of the scattered field from the l^{th} dielectric wire, $\mathbf{r}_k$ is the location of the k^{th} dielectric wire, $\mathbf{r}_n$ is that of the n^{th} point source, and s_n represents the excitation coefficient of the n^{th} point source ($s_n = -\omega\mu s'_n/4$). Using Eq. 3.1, E^y_k can be described by a linear combination of both incident fields due to external sources and the scattered fields by other dielectric wires. A system of 'L' equations can be formed and solved for the unknown ($k = 1, 2, ..., L$). Once the scattered field by each wire is obtained, the total field can be computed at desired points in space.

Considering N radiating point sources over the object plane and M samples (here we assume $M \geqslant N$) over the image plane (Fig. 3.1), we can construct the transmission matrix as

$$[E_{image}] = [t][E_{source}], \tag{3.4}$$

where $[E_{source}]$ is a matrix presenting the complex (real and imaginary) excitation coefficients (s_n) of point sources, and $[t]$ is an matrix where t_{mn} relates the field transmission from the n^{th} radiating point source to the m^{th} sample over the image plane where the measured fields are expressed as $[E_{image}]$. Decomposing the transmission matrix, $[t]$, gives

$$[t] = [U]\Sigma[V]^T. \tag{3.5}$$

Here $[V] = [V_1|V_2|...|V_N]$ and $[U] = [U_1|U_2|...|U_M]$ are $N \times N$ and $M \times M$ unitary matrices, respectively. The column vectors of $[V]([U])$ are called the source (image) eigenchannels (functions). Σ is an $M \times N$ non-negative real diagonal matrix containing the eigenchannel transmission coefficients, $\sigma_n = \sqrt{\tau_n}$, where τ_n are the eigenvalues of $[t]^T[t]$ and $\sigma_1 > \sigma_2 > \sigma_3 > ... > \sigma_N$. Multiplying $[E_{source}]$ by $[V]^T$ maps any arbitrary distribution of excitation coefficients of point sources to eigenchannel vectors which are the columns of $[V]$. The n^{th} column represents one transmission channel and provides the required complex (amplitude and phase) excitation coefficients for each radiating point source so when combined and the radiated fields are transmitted through the structure and the medium, after measured at the pre-specified points, gives the corresponding eigenfunction over the image plane (the n^{th} column of $[U]$) with transmittance of τ_n. The fact that the column vectors of $[V]$ and $[U]$ are orthonormal can be used to extract source information ($[E_{source}]$) from the image signal ($[E_{image}]$).

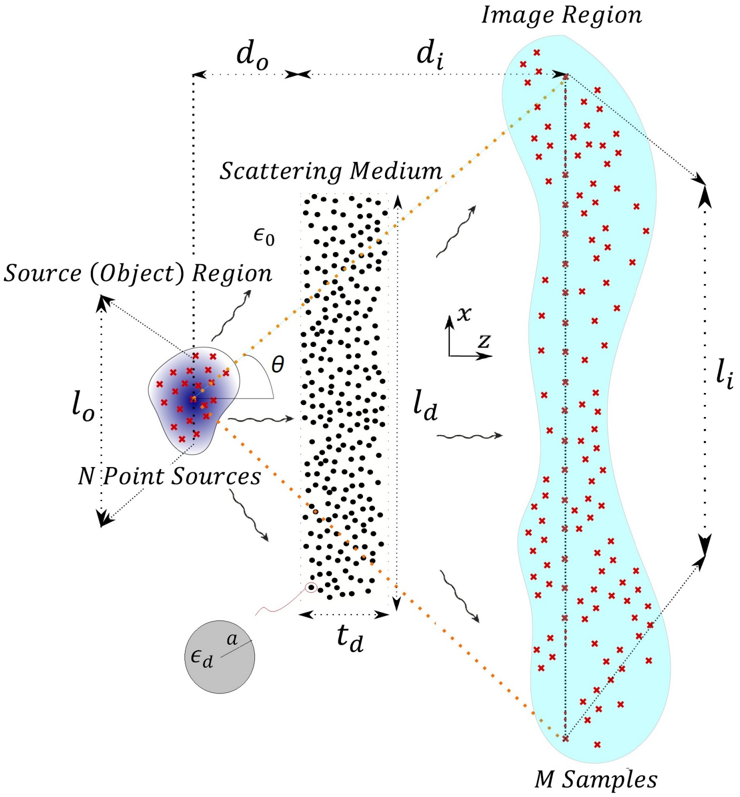

Figure 3.1: The geometry of problem. The radiated fields emitted from N point sources inside the source region propagate through the engineered scattering structure which is composed of a plurality of dielectric wires with radius a and dielectric constant of ϵ_d distributed inside a rectangular region with side length of t_d and l_d. The field measurement is performed at M points over the image region which is located at far-field region. In this work, we only consider the case where the point sources and measurement samples are located on two lines with length of l_o and l_i, located at d_o and d_i from the scattering medium, respectively.

For the N point sources and M samples over the image plane, $[E_{image}]$ can be written as

$$[E_{image}] = \sum_{n=1}^{N} \sigma_n U_n (V_n^T [E_{source}]) = \sum_{n=1}^{N} \sigma_n U_n E_{source}^n, \tag{3.6}$$

where $V_n(U_n)$ represents the n^{th} column vector of $[V]([U])$ and $V_n^T[E_{source}](= E_{source}^n)$is the projection of the source signals onto the basis vectors V_n, which can be used to expand the source excitation coefficients as

$$[E_{source}] = \sum_{n=1}^{N} (V_n^T [E_{source}]) V_n = \sum_{n=1}^{N} E_{source}^n V_n. \tag{3.7}$$

Multiplying both sides of Eq. 3.6 by U_n^T/σ_n and using the orthonormality of U_n, E_{source}^n can be extracted. In the next step, source distribution can be computed using the expansion of Eq. 3.7.

As it is clear, the larger the value of σ_n is, the more signal power of the n^{th} mode will be transferred through the corresponding eigenchannel and received by the detectors. Our goal, in this chapter, is to design scattering structures to maximize the transmittance of the highest order eigenchannels (modes). This is to increase the number of channels with acceptable power level for a receiver with a known SNR to detect. As the exact extraction of source signals is limited by the receiver ability to detect the weakest signals which correspond to the lowest transmittances in the SVD formulation (Eq. 3.5), by increasing the transmittance of the higher order modes, for a given level of noise power or SNR at the receiver, we increase the number of modes which can be detected. The more number of modes can be detected, the more detailed information can be extracted from the received signals. In imaging application, this means the enhancement of resolution by detecting higher order signals emitted from illuminating sources which are associated with the fine features of the object being imaged. Various parameters affecting the transmittance include the number of point sources and the distance between them, the number of samples over the image plane and the distance between them, the distance between the object plane and the image plane, and the scattering property of the medium the radiated signals are propagating through. The latter include the property of both the scattering structure and the free space. In this chapter, we propose a new approach to design scattering structures in such a way that when they interact with the electromagnetic fields emitted from the point sources or illuminated object they increase the transmittance of the highest order mode. Before that, in this Section, we investigate how other parameters can affect the transmission of highest order signals through a given scattering medium.

As an example, we consider a structure consisting of 340 dielectric wires ($\epsilon_d = 4.61$, $a = 0.02\lambda$) (Fig. 3.2). We change the number of point sources (N) distributed uniformly over a given region (l_o) on source (object) plane and for each case we take M equally spaced samples over a given region (l_i) on the image plane. The distances between the source (object) plane and the structure and between that to image plane are denoted by d_o and d_i, respectively. Using Eq. 3.5 the transmittance of the last mode (the N^{th} mode) is calculated. As mentioned earlier, this is an indication of the resolution can be achieved in a given imaging or communication system. Larger transmittance is associated with higher SNR and accordingly higher resolution for the corresponding mode.

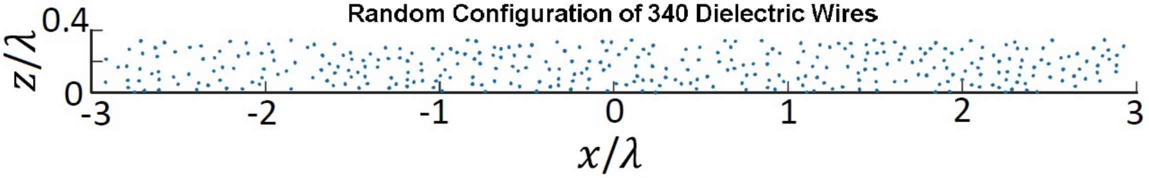

Figure 3.2: The location map of a randomly configured structure composed of 340 dielectric wires.

First, we set $d_i = 20\lambda$, $d_o = 0.16\lambda$, and $l_i = 400\lambda$. Changing l_o, the transmittance (τ_n) is calculated as a function of N (number of point sources) and M (number of samples). As expected, with the same number of point sources (N), the transmittance increases as the distance between the point sources becomes larger (Fig. 3.3). This is mainly due to the fact that the images obtained by different radiating sources located at farther distances are less correlated than those located at closer distances; thereby higher transmittance in SVD formulation is obtained. As the number of samples over the image plane increases, higher level of signal power is expected. However, this dependency is not linear and the rate of power change becomes very small in larger sampling points. The size of image region, where the samples are taken from, also affects the measured transmittance (Fig. 3.4). With fewer numbers of samples, smaller sampling regions near the source region show higher transmittance. By increasing the number of sample points, however, larger sampling areas (over the image region) are superior in terms of transmittance. This confirms that the interaction of the incident field with the scattering structure results in diffracted fields which contain information over larger sampling region on the image plane. We define the NA (numerical aperture) as the angle seen from the centre of the source region to the sampling region over the image plane (Fig. 3.1). For two identical systems, with a fixed NA, the changes in the distance between image and source (object) planes, while the image plane is in the far distance from the scattering medium, results in inversely proportional to distance (r) changes in the highest order mode transmittance (Fig. 3.5) verifying that the measurements are performed at the far-field regions where the evanescent fields are largely absent. The highest order modes contain information about sub-diffractional features of radiating sources. The presence of scattering structure can lead to the enhancement of the transmittance of these modes and our ability to resolve sub-wavelength information of the illuminated objects or radiating sources. In the next Section, we investigate the effect of scattering structures on the enhancement of the higher order modes transmittances. We propose a new approach in designing all dielectric scattering medium and demonstrate how they can lead to the enhancement of sub-wavelength information transfer. Although the proposed method is applied to scattering media composed of dielectric wires, it can be generalized and used, also, to design scattering structures composed of three dimensional dielectric scatterers.

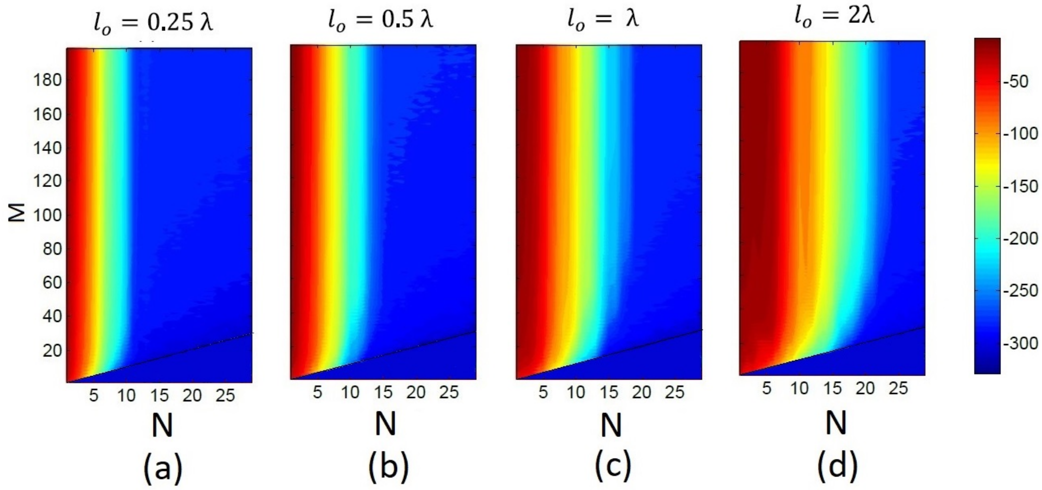

Figure 3.3: The highest order transmittance (dB) as a function of N and M ($M \geqslant N$) and $d_i = 20\lambda$, $l_i = 400\lambda$. For (a) $l_o = 0.25\lambda$, (b) $l_o = 0.5\lambda$, (c) $l_o = \lambda$, and (d) $l_o = 2\lambda$.

3.2.2 Engineered disordered all dielectric medium

As mentioned in the previous Section, scattering medium can enhance the transmission of high resolution information to the far-field region. In this Section, we investigate this in more details and propose a new design approach for engineering the scattering properties of medium. This is done through designing structures composed of dielectric wires which are

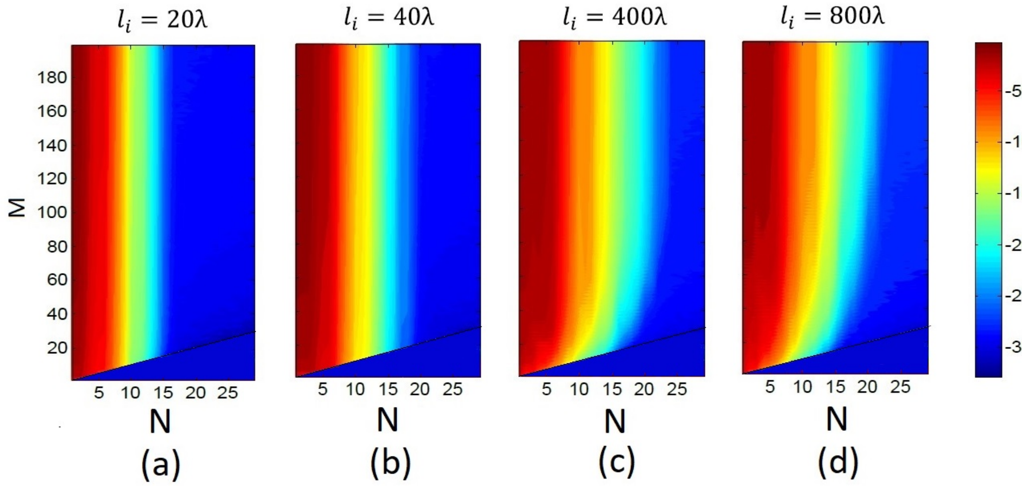

Figure 3.4: The highest order transmittance (dB) as a function of N and M ($M \geqslant N$) for $d_i = 20\lambda$, $l_o = 2\lambda$. For (a) $l_i = 20\lambda$, (b) $l_i = 40\lambda$, (c) $l_i = 400\lambda$, and (d) $l_i = 800\lambda$.

.

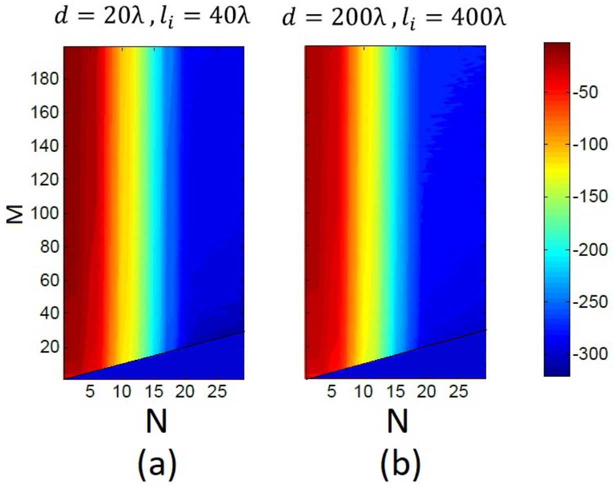

Figure 3.5: The highest order transmittance (dB) as a function of N and M ($M \geqslant N$) and $l_o = 2\lambda$. For (a) $d = d_i + d_o = 20\lambda$, $l_i = 40\lambda$, and (b) $d = d_i + d_o = 200\lambda$, $l_i = 400\lambda$. The two cases, (a) and (b), represent the results for a same numerical aperture.

.

located within a confined specified region. The proposed devices provide a rich scattering medium maximizing the transfer of waves associated with the highest order radiating modes of the illuminated objects/ radiating sources to the receiver side located at the far-field region. It is important to note that the optimization problem we define here, like most problems in topological designs, is not convex which typically means that there are several different local maxima (minima), or non-unique solutions. The proposed methods known as topology optimization are based on the method of gradient descent where initial solutions are iteratively optimized to obtain a local maximum (minimum). On the other hand, due to the large number of variables, most global optimization methods cannot handle this type of problems efficiently [100]. In this Chapter we propose and employ a new stochastic-based optimization approach which is capable to search for the global solutions based on defined constraints and design parameters.

In this work, we assume the physical characteristics of dielectric wires including the radius and the dielectric constant (refractive index) are known. The designed structures, which consist of a plurality of identical dielectric wires, are confined within a rectangular region with known values for the length and the thickness. The optimization problem is defined to maximize the highest order mode transmittance for a set of radiating point sources located at known locations over the source (object) plane. This can be achieved through introducing dielectric wires at proper locations within the specified region by following our proposed procedure explained in this Section.

If we have a set of point sources with known positions radiating in free space, introducing an individual dielectric wire perturbs the scattered fields in the far field region. Depending on the position of the scattering object (a dielectric wire in this work) with respect to the radiating sources, the correlation between the captured radiated fields from adjacent point sources may differ by certain values. As mentioned previously, it is desired to have lower values for the correlation which is equivalent to higher values for the transmittance of higher order modes (See the SVD formulation, Eq. 3.5). Our proposed algorithm is based on finding a proper location for adding one dielectric wire so that for a given scattering medium, it maximizes the power of highest order radiating modes over the far-field region. Adding dielectric wires is continued until the transmittance of highest order radiating mode cannot be further enhanced or the preset maximum number of dielectric wires is reached. Controlling the design procedure is done through defining a number of parameters. The most important one is called the transmittance threshold. This determines the criterion for adding one new dielectric wire at a new location randomly selected by a computer simulator. The numerical value for this threshold is set using the statistical property of structure in a given physical configuration. For a given imaging or communication system, with known physical parameters and locations for radiating point sources, the average value of the highest order transmittance is calculated for different numbers of dielectric wires distributed randomly inside the specified rectangular region. We change the number of dielectric wires from one to an arbitrary maximum number ($n_d = 1, 2, 3, ..., N_d$), and for each case the average value of transmittance is calculated for a large number of randomly configured dielectric wires generated inside the specified region. The result, which indicates the statistical property of structure, describes the average changes in the transmittance in terms of the number of dielectric wires and provides the required information about the effect of adding one dielectric wire to an existing scattering structure with n_d dielectric wires. This can be understood from the slope of the graph at a point which corresponds to the number of dielectric wires (n_d) in an existing scattering medium. Depending on the number of dielectric wires, the initial value for the transmittance threshold, which is the key parameter in our design procedure, is chosen to be an integer multiple of the slope calculated at the corresponding point on the graph. Two other parameters used in the algorithm are denoted by M_t and N_t. M_t is used to control the maximum number of iterations in finding a proper location to add one new dielectric wire to an existing configuration. N_t determines the number of successive tries after which the value of transmittance threshold is modified in order to improve the efficiency of algorithm in selecting the best locations for dielectric wires leading to an overall remarkable enhancement of the transmittance of the highest order radiating mode at the end of design procedure.

The flowchart shown in the Appendix B describes our proposed algorithm for designing a dielectric medium with enhanced scattering properties. It starts with an initial configuration of dielectrum wires located inside the region which provides a relatively good choice between many candidate configurations with the same number of dielectric wires. It is obtained either by running a large number of simulations generating random configurations and choosing the best one among them or choosing a known configuration which has been obtained previously. Depending on the initial number of dielectric wires in the primary configuration, the transmittance threshold is set to be significantly larger than the average change of transmittance due to adding one dielectric wire to the existing configuration. This can be done using the statistical property obtained previously by extracting the slope at a proper point. After choosing an initial configuration of dielectric wires, where the locations are shown by $\{(x, y)\}$, the cost function, denoted by C, which is set to be the highest order transmittance for a given locations of point sources is calculated. The parameters including the transmittance threshold, M_t, and N_t are initialized to proper values. A new set of temporary dielectric wire locations is defined which is represented by $\{(x, y)_t\}$. This set includes the candidate locations to add one new dielectric wire to the existing configuration denoted by $\{(x, y)\}$. Adding one dielectric wire at each location which is saved in $\{(x, y)_t\}$, will change the transmittance to a new value which is recorded in a new set denoted by $\{C_t\}$. The design procedure starts by adding one temporary (test) dielectric wire at a random location (x_r, y_r) inside the specified region. The transmittance of the new configuration is calculated and is saved in C_r. If the enhancement in C is larger than the current transmittance threshold, the new location and corresponding transmittance are saved in $\{(x, y)_t\}$ and $\{C_t\}$, respectively. This step is repeated for M_{tmax} times after which the best location in $\{(x, y)_t\}$, corresponding to the maximum transmittance saved in $\{C_t\}$, is chosen for the location of one new dielectric wire to be added to the current configuration $(\{(x, y)\})$. This procedure is repeated for N_{tmax} times after which a maximum number of N_{tmax} dielectric wires can be added to the initial configuration. Depending on whether the number of dielectric wires has been changed (increased) or none of the random locations were selected for adding dielectric wires to the previous configuration, the value of transmittance threshold will be updated. If any dielectric wire has been added to the structure, the threshold is increased by some coefficient which can be set by user. This makes more stringent condition for adding new dielectric wires in the next iterations. This is continued until no dielectric wire can be added to enhance the transmittance greater than the updated threshold. At this point, we will gradually decrease the threshold (through one or successive iterations) so that at least one dielectric wire can be added to the current configuration. Although this can lead to a temporary, typically small reduction (depending on the threshold value and the current configuration), in the transmittance in a situation that we have a close to optimum structure (near one local maximum of the cost function), the new configuration, which includes the latest dielectric wire, can be improved (in the next steps) to obtain a more optimum configuration than the best configuration obtained so far in the previous steps. This process can be repeated until the maximum transmittance for the highest order radiating signal illuminating the designed structure is obtained, or the user can stop the process for any other reason such as reaching to the preset number of dielectric wires (the complexity of structure). More information on the proposed algorithm is provided in the Appendix B.

Now, we consider the application of the proposed algorithm in a few examples. The effectiveness of our approach in designing the engineered structures can be seen through comparison with those which have periodic or totally random configurations.

3.3 Numerical results

3.3.1 Design examples

We consider a rectangular region like the one shown in Fig. 3.1, with the length sides of $t_d = 0.34\lambda$ and $l_d = 5.85\lambda$. The region is going to be populated with dielectric wires having a radius of 0.02λ and refractive index of 3. They are illuminated by point sources with known locations over the source (object) plane. The purpose is to design a structure composed of sufficient number of dielectric wires within the rectangular region to significantly increase the transmission of the highest order modes of the source signals to the far-field region. In the present examples we assume that the distance between the source (object) plane and the rectangular region is about one over sixth of the wavelength of illuminating sources ($d_o = 0.16\lambda$) and that between the rectangular region and the image plane is twenty times the wavelength ($d_i = 20\lambda$). The field is sampled over a region with length of $l_i = 400\lambda$ and the total number of sample points is two hundred ($M = 200$). Two groups of sources will be considered here. The first group is composed of ten ($N = 10$) equally-spaced point sources distributed over a region with length of $l_o = 0.58\lambda$. In the second group, we increase the number of point sources to fifteen ($N = 15$) distributed over the same region. The design procedure starts with calculating the average transmittance of the structure for $n_d = 1, 2, 3, ..., 900$ number of dielectric wires. To this end, for each n_d, we run a large number of simulations with random configurations and take the average of the calculated highest order transmittance for each simulation. The calculated values give an estimate of how much, on average, the highest order mode transmittance is increased if we add one new dielectric wire to a given configuration which consists of a total of n_d dielectric wires. As mentioned before, the slope of the resulting graph is used to set the initial value for the transmittance threshold in the optimization process. Figure 3.6 demonstrates the results for the two groups of sources.

The next step is to initialize the parameters in the algorithm and to define an initial configuration of dielectric wires as the starting point in the process of optimization. We set $M_{tmax} = 20$, $N_{tmax} = 5$ and the transmittance threshold to be 10 times larger than the average value it increases when one dielectric wire is added to an existing initial configuration (this value can be obtained from the graphs shown in Fig. 3.6). For a given configuration, and transmittance threshold, the algorithm chooses the best location for adding one new dielectric wire among a maximum $M_{tmax}(= 20)$ randomly selected locations improving the highest order transmittance by at least the value set by the transmittance threshold. It repeats this process for $N_{tmax}(= 5)$ times. Therefore, a maximum number of $N_{tmax}(= 5)$ dielectric wires can be added. If no wire is added, the threshold will be decreased by a factor of two, i.e. if the threshold is positive the new threshold becomes the multiplication of the previous one by half and if the threshold is negative, the updated threshold is the previous one multiplied by two. Otherwise, if at least one dielectric wire has been added, the threshold will be increased by the same factor, i.e. if the threshold is positive, the updated threshold becomes two times the previous one and if the threshold is negative, the updated threshold becomes the multiplication of the current threshold by half. As can be

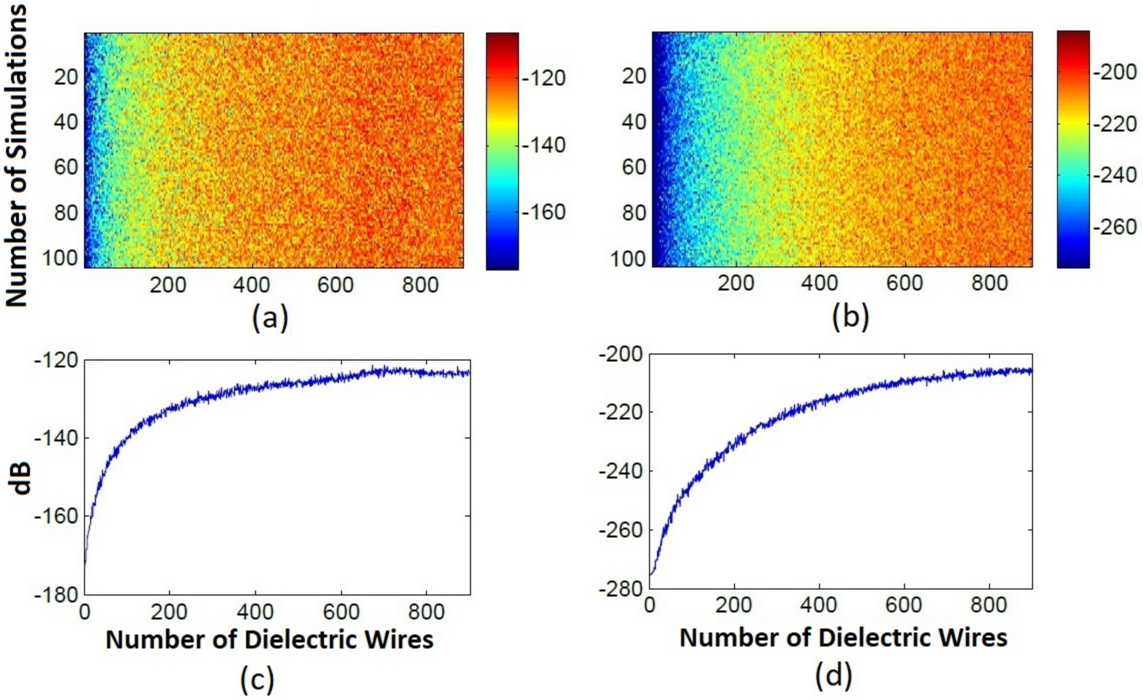

Figure 3.6: (a) and (b) show the highest order transmittance (dB) of 10 and 15 point sources, respectively, distributed uniformly on $l_o = 0.58\lambda$ when illuminating random scattering structures. The horizontal axis shows the number of dielectric wires in the structure which are randomly configured in a rectangular region of side lengths $t_d = 0.34\lambda$ and $l_d = 5.85\lambda$. The calculations are performed for a large number of random configurations, each denoted by a number on the vertical axis (number of simulations). (c) and (d) demonstrate the average value of the transmittance calculated in (a) and (b), respectively.

seen, the value of threshold can become very close to zero at some point. In this case, we define a crossover value which we set to be the initial threshold multiplied by 1e-7. If in the process of updating, the value of threshold becomes smaller than this value, the algorithm changes the sign of the new threshold. This way, both positive and negative values for the threshold can be obtained (more detailed information about the algorithm is provided in the Appendix B).

There are different options to set the initial configuration of dielectric wires. One can choose to start with an arbitrary number (n_d) of dielectric wires. For this, a large number of simulations can be performed, at each simulation, n_d numbers of dielectric wires are randomly distributed inside the region and the best one which has the largest highest order transmittance among others can be chosen as the initial configuration. To highlight the efficiency of our design method, we also consider starting with a periodic configuration. For this purpose, we calculate the transmittance of the highest order mode for all periodic configurations which can be defined within the specified rectangular region (Fig. 3.7). We choose the best periodic configuration with the highest transmittance as the initial configuration for each group of point sources. For the case of 10 point sources, the best periodic configuration is that of 9×41 and for the case of 15 point sources the periodic configuration of 9×63 gives the best highest order transmittance. Following the steps of the proposed algorithm which was described previously, we finally obtain structures composed of dielectric wires arranged in such a way that maximize the highest order transmittance of radiating sources. Figure 3.8 (a) and (b) show the final configurations for two cases of ten and fifteen point sources, respectively. Although the structures have been designed for particular source locations, we characterize the final structures in terms of the

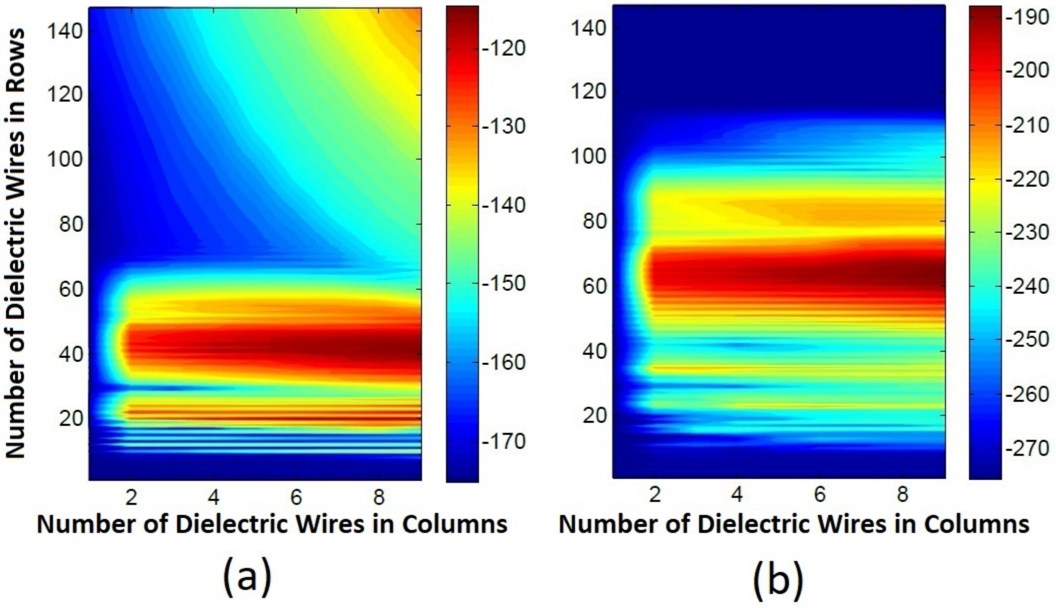

Figure 3.7: The highest order transmittance (dB) for (a) 10 point sources and (b) 15 point sources distributed uniformly on $l_o = 0.58\lambda$ when illuminating scattering structures populated uniformly by periodic configuration of dielectric wires. The horizontal and vertical axis shows the number of dielectric wires at each column and row, respectively.

.

highest order transmittance for different number of point sources distributed on different line scales. As compared to the free space where no scattering medium is present, the disorder-based engineered structures not only can significantly improve the information transmission of the particular sets of source locations they have been designed for, but also they can lead to considerable enhancement of the transmission of highest order signals for other combinations of point sources ((III) of Fig. 3.8). This is important to mention that depending on the configuration of point sources, the maximum achievable enhancement varies. In other words, although the achieved enhancements for other source configurations might be larger than the maximum enhancement we achieved for the particular set of point sources, they do not necessarily correspond to their optimum values which can be reached through the optimization process. To comply with the state-of-the-art fabrication techniques [101, 102], here we have assumed multilayer structures where the freedom in choice of dielectric wire locations is limited in one axis (z axis) while there is no limit to the freedom for the placement of dielectric wires in the horizontal axis (x axis). Nevertheless, there exist more regular types of structures with predefined locations for the dielectric wires in both axes which have less number of degrees of freedom as compared to our generally defined configuration. Various global optimization techniques such as genetic algorithm or simulated annealing [1] can be employed for the design of regular structures similar to works done previously for optical nanoantenna structures [94, 60].

Now we investigate multilayer structures where the initial configurations are not periodic. Starting with a randomly configured 200 dielectric wires featuring the best transmittance among hundreds of randomly generated configurations, we obtain structures shown in Fig. 3.8 (c) and (d). If we let the algorithm put the dielectric wires anywhere along both axes (x and z axis), we can obtain completely disordered structures (Fig. 3.8 (e) and (f)), although they might be more complicated in terms of fabrication [103]. Comparing the results indicates that designing structures with more general configurations can lead to the almost the same level of enhancement with less number of scatterers in the structures (Fig. 3.8 (c) to Fig. 3.8 (f)). Any point on the 2D plots of Fig. 3.8 represents a particular number of point sources uniformly distributed over a specific length on the source (object) plane. The tangent of the angle (ϕ) formed by the line connecting any point on these plots to the origin indicates the resolution we require to successfully image all the corresponding point sources. The color of these plots ((I) and (II)) shows the transmittance of the highest order mode signal emitted from corresponding point sources which determines the required SNR of the receiver. As can be seen, by introducing the engineered scattering medium, we can obtain the same level of transmittance with larger number of point sources distributed over the same length on the source plane. In other words, the points pertaining to the same color on (II) make smaller angle (higher resolution) than corresponding points on (I).

Thus far, we assumed the designed metalenses are composed of dielectric inclusions with negligible loss. However, concerning the practical situations, it is worth to investigate how loss would affect the scattering features of designed structures shown in Fig. 3.8. Assuming that the structures are illuminated by monochromatic radiating sources, the imaginary part of refractive index ($\sqrt{\epsilon_d} = n - j\kappa$) is changed from zero to 4, i.e. $n = 3$, $0 \leqslant \kappa \leqslant 4$, and for each value, the transmittance of all modes are computed (see Fig. 3.9). In addition, we calculate the average value of transmittances of all modes in the presence of designed structures with respect to that of propagating through the free space (relative average transmittance). As expected and is evident from Fig. 3.9, by increasing the loss of dielectric wires the transmittances of all modes will decrease. However, the rate of changes is not the same for different modes in various configurations. In general, for small values of loss, i.e. $0 \leqslant \kappa < \kappa' \approx 0.5$, the transmittances of modes drops faster as compared to higher values of loss. Comparison between the results of engineered structures for ten and fifteen point sources (the left and right columns of plots in Fig. 3.9, respectively) reveals the higher susceptibility of the formers modes transmittances to the changes of loss. In other words, the transmittances of the modes associated with ten point sources (including the highest order mode (10^{th} mode) which determines the ultimate resolution in our method) drop faster as loss increases in this range ($0 \leqslant \kappa \leqslant 4$). For large values of κ (not shown here), however, the transmittances approach to constant values. It can also be seen from the Fig. 3.9 that, as loss increases, after some threshold, the rate of changes of relative average transmittances becomes significantly small and approaches a constant value which is smaller in structures with larger number of dielectric wires.

In the next Section, we consider one of the designed structures and show how they can be used to enhance the transmission of information in a given imaging/communication system.

3.3.2 Information enhancement using modified orthogonal transmission channels

In this Section, we explain how the engineered scattering structures improve the transfer of information in an imaging/communication system. Regarding the communication systems, modulated radiating point sources (defined through excitation coefficients; s_n) can be used to transmit information signals. Similarly, from the imaging systems perspective, the scattered fields from illuminated objects can be expanded in terms of radiating point sources with excitation coefficients related to unknown object(s) physical features [104]. In either case, the problem is formulated as described by Eq. 3.3 and our goal is to retrieve the unknown excitation coefficients from the measured signals over the far-field region. As an example, we consider the designed structure of Fig. 3.8 (c) which is optimized for the ten point sources located over the described source (object) plane. According to the SVD formulation (Eq. 3.5), any distribution for the excitation coefficients of ten point sources can be described as a linear combination of ten orthogonal basis vectors (the columns of $[V]$). In other words, the orthogonal source basis vectors can be used to construct any distribution for the point source excitation coefficients. As mentioned previously, the main role of the designed scattering medium is to maximize the highest order transmittance of the modified orthogonal source basis vectors due to the presence of scattering medium. The modified orthogonal basis vectors, which we refer to as modified transmission channels, can be used to excite the point sources for efficient information transfer in the communication systems. Each vector of the source basis vectors corresponds to one particular vector on the receiver side (one column of $[U]$). Similar to the point source expansion in terms of orthogonal vectors on the transmitter side, these vectors (the columns of $[U]$) can be used to construct any field distribution due to the source excitation, over the image plane. The highest order transmittance, which is maximized in the presence of the designed structure, corresponds to the transmission of the source basis vector with the highest spatial frequency which is also related to the high resolution information of radiating sources/illuminated object(s). Figures 3.10 and 3.11 demonstrate the source basis vectors and the associated eigenvalues (square root of transmittance), before and after the scattering medium is introduced, respectively. As can be seen, the imaginary parts of the source basis vectors assume nonzero values when the scattering medium is introduced and become larger for higher order signals. This reveals that by applying proper phase shifts between source signals, the multiple scattering events that signals experience as they propagate through the scattering medium are compensated, leading to an improved transmission of sub-wavelength information to the far-field region. Similar phenomenon has been observed and exploited to achieve perfect optical focusing through disordered structures [34]. It is important to mention that the improvement in resolution comes at the expense of decreased average total transmittance which for the designed scattering medium is about 55% of that of the free space medium. This is attributed to the multiple scattering occurring inside the structure also causing some reflection from the medium. Figure 3.12 shows the total electric field distribution after exciting the highest order mode for both free space and the designed scattering structure. As it is clear, the scattering medium significantly improves the signal level at the far field region. Depending on the noise level, or SNR, the accurate extraction of the source information is limited by the power of the highest order mode which is the weakest component of the transmitted signals. According to Eq. 3.6, as mentioned before, each component can be obtained using the orthogonality property of basis vectors. However, the added noise is not cancelled in this process and has the maximum effect on reducing the SNR of the weakest component of the signal.

As an example we consider ten random source signals ($N = 10$) with excitation coefficients ($s_n, n = 1, 2, ..., 10$) lying on the perimeter of circle $r = (1/\sqrt{10})$ over the complex (amplitude and phase) plane. To extract the source signals from the measured signal in Eq. 3.6, we discard terms with transmittance level lower than the noise level of the receiver. We add white Gaussian noise (WGN) with the SNR changing from 50 dB to 180 dB and take the average of root mean square (RMS) errors between hundreds of source distributions and the corresponding retrieved images. Comparing the results for propagation through the free space and the engineered scattering medium, we can observe the significant improvement in restoring the source signals (Fig. 3.13). By introducing the engineered scattering structure of Fig. 3.8 (c), with the same level of SNR, the source signals can be extracted more accurately. As can be seen from Fig. 3.13, even for lower SNRs the engineered structure reduces the RMS error. However, the significant improvement takes place once the SNR becomes close to or larger than 100 dB (blue curve in Fig. 3.13). The reason can be understood by comparing the transmittances of highest order modes in Fig. 3.10 and Fig. 3.11. The highest order transmittance of the modified source basis vectors, which is about -96.1 dB, determines the required minimum SNR to accurately retrieve the information signals. The same procedure can be done for the case of seven point sources ($N = 7$) distributed uniformly over the same region, with excitation coefficients ($s_n, n = 1, 2, ..., 7$) lying on the perimeter of circle $r = (1/\sqrt{7})$ over the complex (amplitude and phase) plane. The modified highest order transmittance for seven point sources is about -67.5 dB which set the minimum SNR for accurate extraction of information signals (green curve in Fig. 3.13). From the communication point of view, if we were to send ten pieces of information signals through the ten point sources radiating in free space and located at sub-wavelength distances (0.064λ in this case), higher order modes get strongly attenuated as they propagate towards the receiver. Unless we have a very large value for the SNR, which is not practically possible, we are not able to restore all the source signals from the received signal. However, for the same level of SNR, the engineered scattering medium is capable to enhance the level of transmitted power of higher order modes so that the number of received signals (channels) increases. Depending on the SNR, the modified orthogonal transmission channels with acceptable level of transmittance can be used to modulate and combine more information signals which can be restored with minimum error. For example, if the SNR level at the receiver side is 70 dB (or 100 dB), according to the level of transmittances shown in Fig. 3.11, the first seven (or ten) independent modified basis vectors can be used to modulate information signals. For digital binary communication, that means a realization of 2^7 (or 2^{10}) pieces of information, which is a two(eight)-fold enhancement as compared to the propagation through the free space, where the first six (or seven) channels of acceptable transmittance levels, which is equivalent to the realization of 2^6 (or 2^7) pieces of information, can be chosen to modulate signals.

3.4 Conclusion and perspective

We proposed a new approach for enhancing the transmission of high resolution signals emitted from point sources located at ultra sub-wavelength distances which leads to an enhanced imaging resolution and information capacity in communication systems. Our method is based on employing disordered engineered scattering structures. The high degrees of freedom inherent in such disordered medium enable us to come up with structures which have superior functionality as compared to their periodic and random counterparts. We demonstrated that the disorder in such structures can be exploited to significantly minimize the correlation between the radiated signals emitted from adjacent point sources at ultra sub-wavelength distances. An SVD technique is used to describe the transmittance of the highest order signals emitted from a given source region. We applied our proposed global optimization method to design scattering structures with high degrees of freedom to increase the highest order transmittance. Comparison with completely random and periodic configuration verifies the effectiveness of our method. We studied one particular example of ten point sources located at sub-wavelength distances from each other where the designed scattering medium significantly improves the level of accuracy in restoring the source signals for a given level of SNR at the receiver. Although the analysis and design procedure were performed for 2D structures and scattering medium with specific physical properties for scattering inclusions (dielectric wires with specific diameters and dielectric constants), the proposed approach can be applied to more general 3D structures with more stringent physical constraints which comply with available fabrication techniques and obtain even more improvements by introducing stronger scattering inclusions (higher dielectric constant) within the structure. Moreover, as it is shown, significant improvement on resolution can be achieved for other configuration of point sources or at different locations for image plane which, depending on the receiver SNR level, can further enhance the effectiveness of the method.

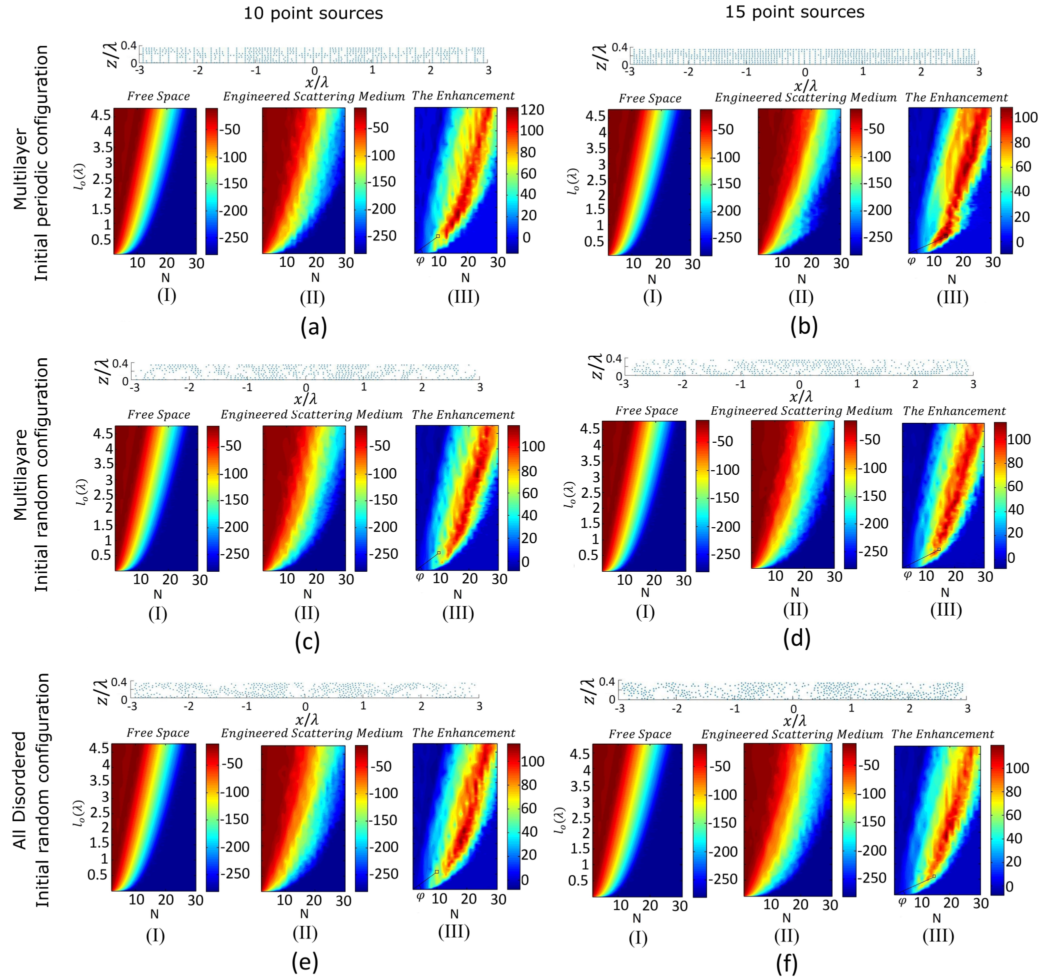

Figure 3.8: The highest order transmittance (dB) for disordered metalenses designed for 10 [(a), (c), (e)] and 15 [(b), (d), (f)] point sources distributed uniformly over $l_o = 0.58\lambda$. (I) The highest order transmittance for $N = 1, 2, ..., 30$ and $0.003\lambda < l_o < 4.57\lambda$ when there is no scattering medium introduced. (II) The highest order transmittance when the engineered scattering medium composed of 692, 888, 530, 520, 507, and 512 dielectric wires ($\epsilon_r = 9, a = 0.02\lambda$), for (a) - (f), respectively, is introduced in front of the radiating point sources. (III) The enhancement achieved for the transmittance of the highest order radiated fields. The black square shows the target point in our design where an enhancement of about 78 dB, 100 dB, 80 dB, 90 dB, 78 dB, and 85 dB, for (a) - (f), respectively, is achieved. tan (ϕ) indicates the corresponding resolution, which is near 0.064λ [(a), (c), (e)] and 0.041λ [(b), (d), (f)] for 10 and 15 point sources, respectively.

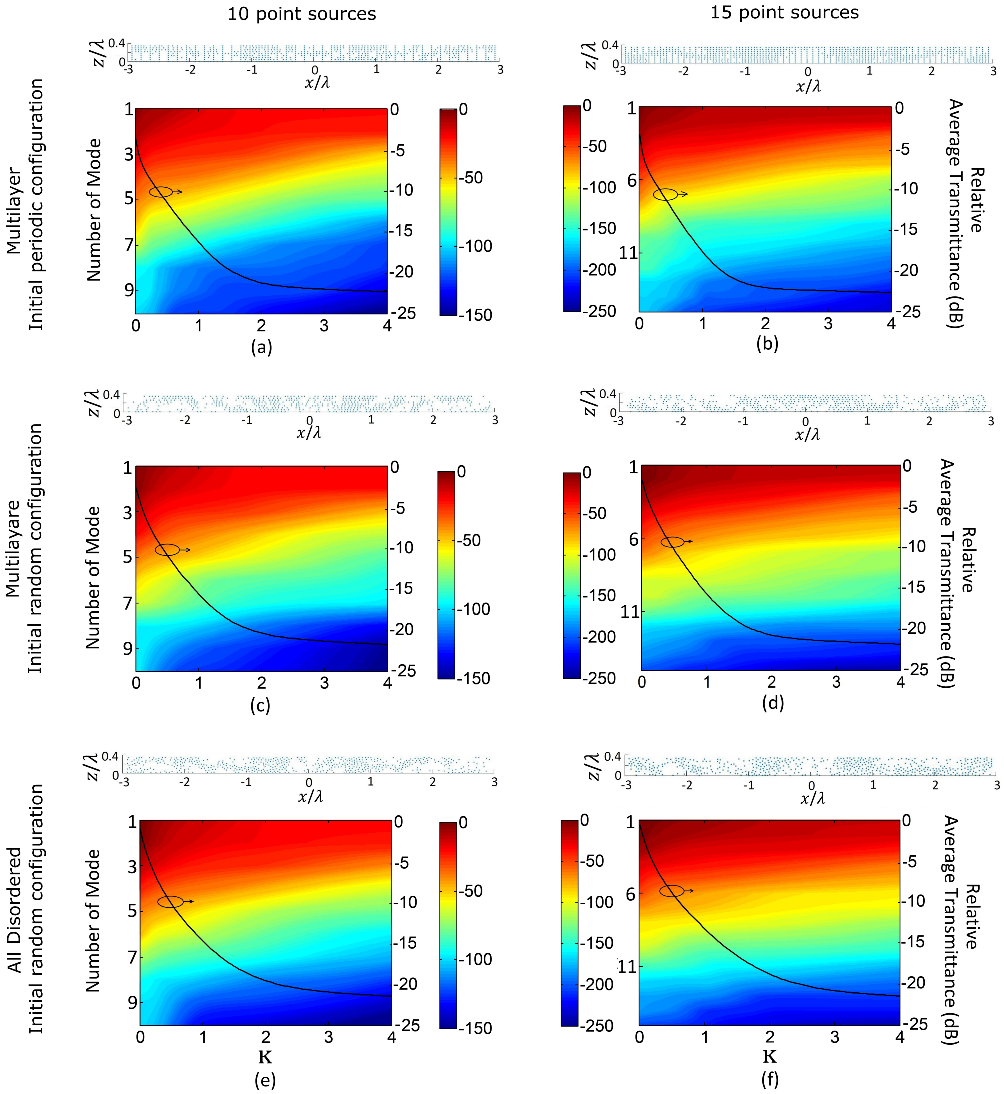

Figure 3.9: The transmittance (dB) of radiating modes versus the extinction coefficient (κ) of dielectric constant (the horizontal axis) for $n = 3$. (a), (c), and (e) correspond to the structures of Fig. 3.8 (a), (c), and (e), respectively, designed for the ten point sources (ten modes) , while (b), (d), and (f) correspond to those of Fig. 3.8 (b), (d), and (f), respectively, designed for the fifteen point sources (fifteen modes). The black solid lines are the relative average transmittances (dB) for each configuration, the value of which can be read from the right vertical axes in the plots (a) - (f).

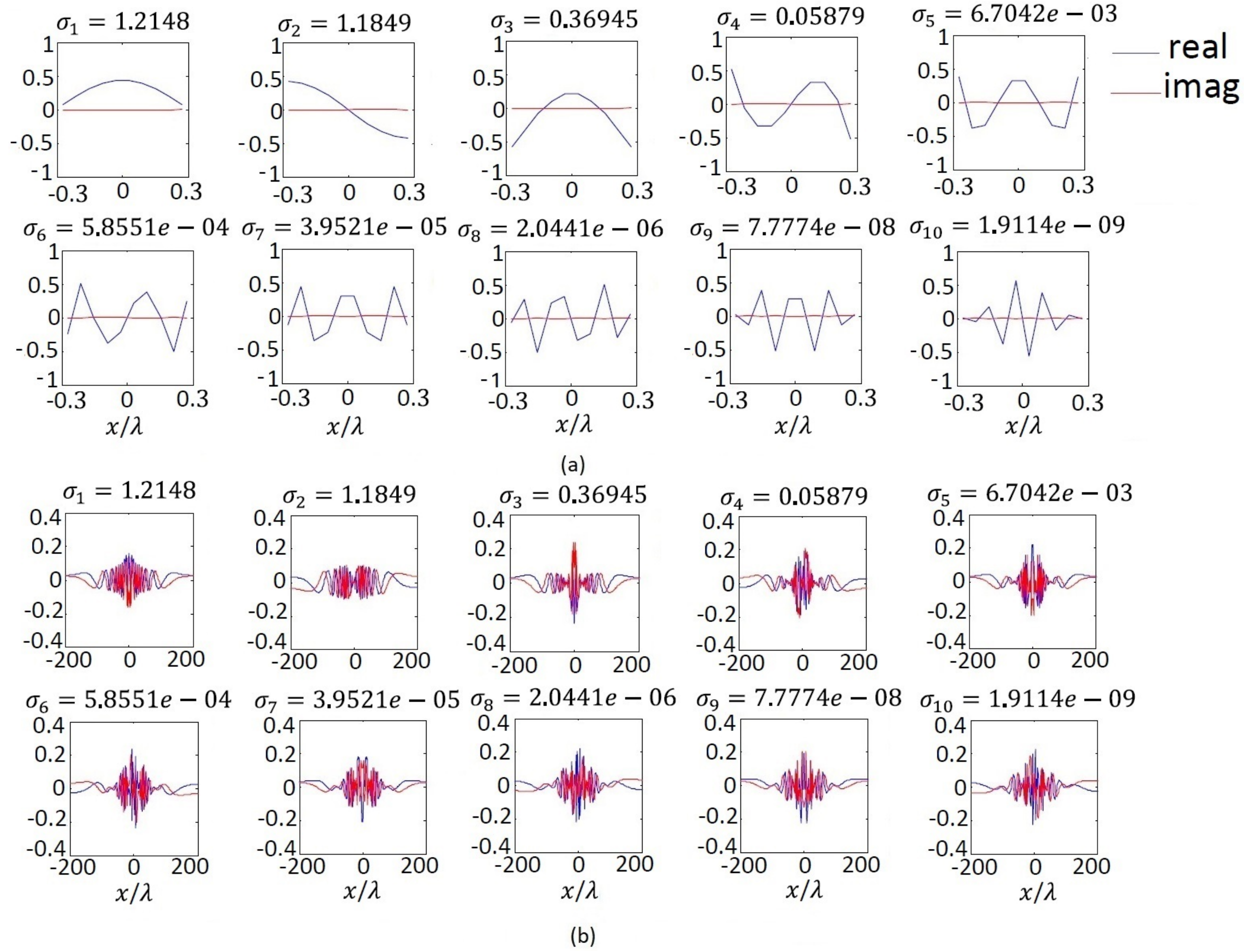

Figure 3.10: (a) Orthogonal source basis vectors for 10 numbers of point sources distributed uniformly over $l_o = 0.58\lambda$ and $d_o = 0.16\lambda$, when there is no scattering medium introduced. The field measurements are performed at $M = 200$ points over the image plane of $l_i = 400\lambda$ and $d_i = 20\lambda$. (b) The corresponding orthogonal basis vectors over the image plane.

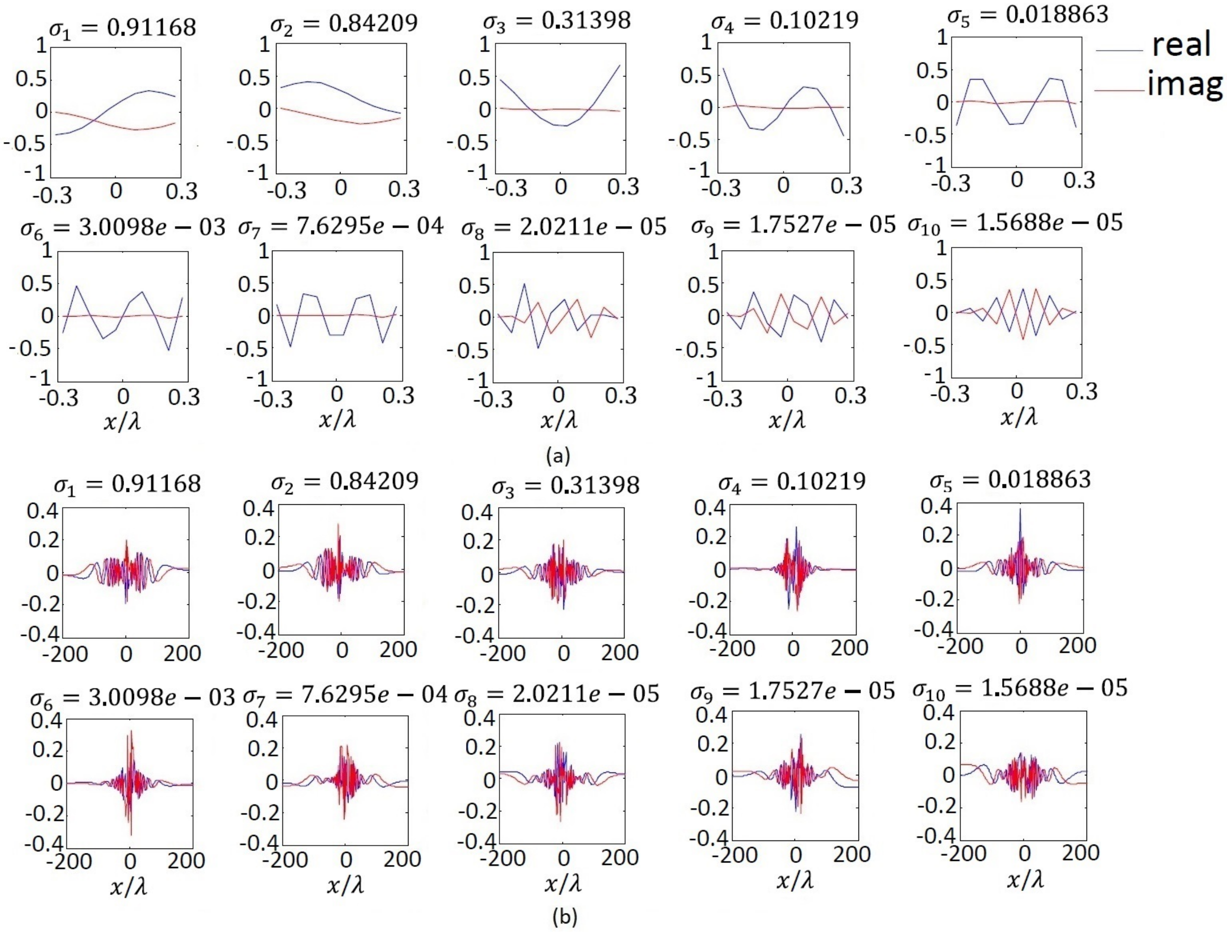

Figure 3.11: (a) The modified orthogonal source basis vectors for 10 numbers of point sources distributed uniformly over $l_o = 0.58\lambda$ and $d_o = 0.16\lambda$, when the scattering medium of Fig. 3.8 (c) is introduced. The field measurements are performed at $M = 200$ points over the image plane of $l_i = 400\lambda$ and $d_i = 20\lambda$. (b) The corresponding modified orthogonal basis vectors over the image plane.

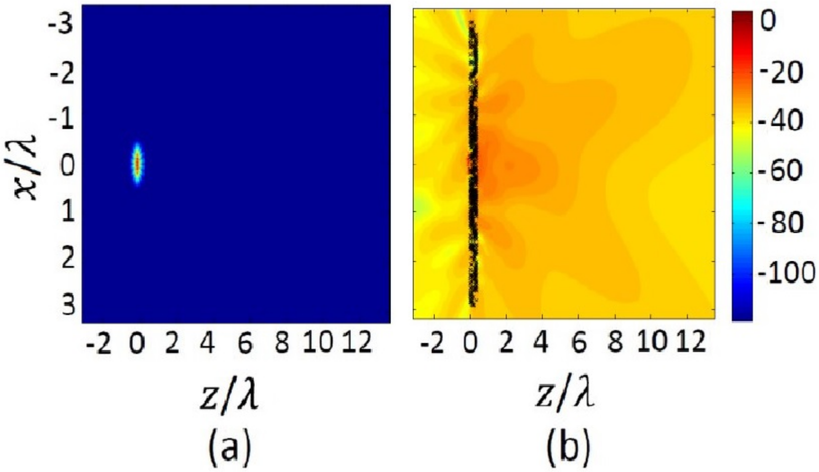

Figure 3.12: The electric field distribution (absolute value) (dB) for exciting (a) the highest order mode in free space and (b) the modified highest order mode in the presence of designed scattering structure (Fig. 3.8 (c)).

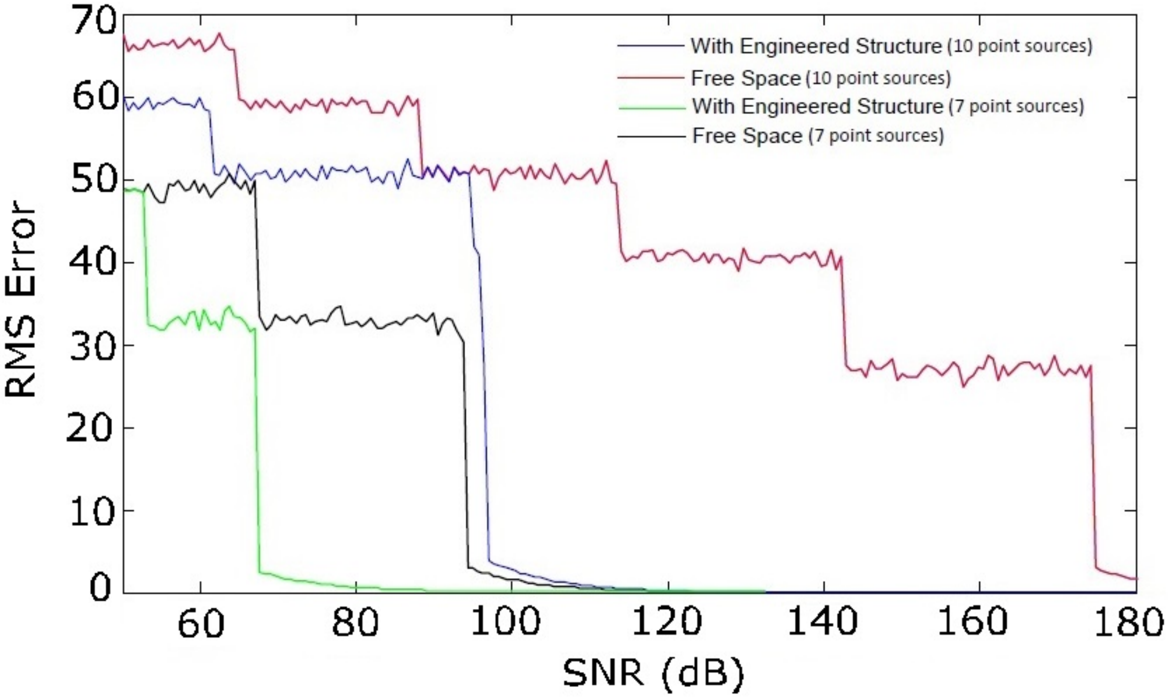

Figure 3.13: The root mean square error versus the SNR of receiver for propagation through both free space (red and black) and engineered scattering structure (blue and green) of Fig. 3.8 (c). The results show the average values taken over hundreds of random source distributions for both 10 point sources and 7 point sources distributed uniformly over $l_o = 0.58\lambda$ and $d_o = 0.16\lambda$. The field measurements are performed at $M = 200$ points over the image plane of $l_i = 400\lambda$ and $d_i = 20\lambda$.

Chapter 4

High performance electromagnetic devices enabled by near-invisible disordered nanowires

Emerging demands on efficient electromagnetic devices require the design and employment of invisible structures enhancing their performance without disturbing the incident electromagnetic fields. In this Chapter, we demonstrate that coatings of disordered silver nanowires (AgNWs) create an electrically conductive film that preserve the radiation characteristics of the original sources over a remarkable range of the frequency spectrum from 75 GHz to 110 GHz. This allows an effective integration of such medium with radiating structures where near-invisible electrodes can be used to significantly enhance the efficiency in designs operating based on tunable materials. As one specific application, we investigate the integration of AgNWs with graphene layer to control the millimeter-wave transmission through graphene. Employing layers of near-invisible AgNWs across the device increases the effective capacitance formed by graphene layer and conductive electrodes used to tune the conductivity of graphene. Theoretical and experimental results demonstrate more than 4-fold enhancement in broadband modulation depth as compared to previous approaches.

4.1 Introduction

Tunable electromagnetic structures have been employed as indispensable parts in imaging, optoelectronics and communication systems. The underlying principle is based on changing the geometrical parameter(s) and/or the materials properties through applying controlling signals to affect the response of the system in desired ways. Electrodes made up of conductive materials play a critical role in the operation of many of such systems. Depending on the application and particular use of electrodes, they should satisfy a combination of physical properties including electrical/thermal conductivity, mechanical flexibility, and electromagnetic transparency. A common approach in antenna radiating systems, for example, is to use these conductors as both controlling electrodes and functional structures such as reflector or radiating elements where high conductivity of electrodes is of particular importance. Although, in many areas like optoelectronics, eg. liquid crystal displays (LCDs), touch screens, organic light emitting diodes (OLEDs) and photovoltaics, the visible light transparency is an essential requirement in addition to electrical conductivity. A variety of materials have been employed to realize electrodes featuring the desired properties in the intended frequency ranges. Examples include doped metal oxides such as indium tin oxide (ITO), graphene [105], metallic grids [106], nanopatterned metals [107], carbon nanotubes [108], conductive polymers [109] and AgNWs [110, 111]. From the proposed options, AgNWs have attracted lots of attention and are considered one of the most promising candidates in optoelectronics. The conductivity and transparency of AgNW electrodes in the visible light, for example, is comparable or even higher than many alternative materials such as ITO. In addition, AgNWs are mechanically flexible, inexpensive, and can be deposited in atmosphere at room temperature using high-throughput deposition methods [112]. Thanks to their high conductivity and flexibility, AgNWs have also been used in wearable and reconfigurable antenna structures at lower frequency ranges (below 4 GHz) as radiating elements [113].

While the transparency of electrodes is a necessary condition in many applications, this does not suffice in certain devices such as spatial modulators and antenna systems operating in various frequency ranges, where conventional metallic electrodes disturb the electromagnetic design. Undesired effects such as the attenuation of the incident fields and scattering effects arise from the interaction of electromagnetic fields with conductive electrodes and therefore, care must be taken in such devices. Employing invisible structures over the intended frequency ranges, on the other hand, provides a more effective option for electrodes which are essential to highly tunable devices. In addition, maintaining the invisibility feature of such electrodes over large scale devices as well as high electrical/heat conductivity are clearly needed. New procedures, therefore, should be used for realizing structures which satisfy the aforementioned features. In this Chapter, our goal is to develop such an approach.

With a wide range of applications such as noninvasive probing and sensors, making objects invisible to impinging electromagnetic waves has been of significant scientific and technological interest. A variety of techniques have been proposed to realize invisibility through engineered structures known as metamaterials. Methods based on transformation optics or scattering cancellation have been utilized extensively to design and realize different forms of invisibility cloaks from microwave to optical range of frequencies [43, 44, 45]. With the aid of metamaterials and employing the concept of transformation optics and conformal mapping techniques, an anisotropic medium with required spatial distributions for permittivity and permeability can be realized. However, realizing negative permittivity/permeability and the required spatial variations over the desired frequency bandwidth are challenging, especially for configurations which make use of resonant elements. There is also performance degradation due to losses associated with the metallic inclusions of the structure. To alleviate these limitations, all dielectric structures have been proposed. Some examples are carpet cloaking [46], methods based on refractive index engineered structures [114], and photonic-crystal- based cloaking devices [115]. In these approaches either a large number of dielectric inclusions are utilized to achieve the required profile for the refractive index and dispersion property in photonic crystals or objects with curved surfaces are used [116, 117]. Simplifications are made to facilitate the fabrication of such structures, however, it is at the expense of leaving some residual scattering which can become large due to small imperfections [118, 119]. On the other hand, relying on non-resonant cancellation, residual scattering can be more efficiently controlled in the scattering cancellation approach [47]. Using engineered cover layers such as multilayer dielectrics and plasmonic covers, this approach aims at canceling out the dominant scattering harmonics in the multipole expansion of the scattered fields. As the number of dominant scattering terms grows, however, more complex structures are required to maintain the performance. This usually happens when the size of the scattering object(s) becomes larger as compared to the wavelength. Although this might not be an issue in a variety of applications such as cloaked sensors, alternative methods are needed to eliminate this limitation for broader range of applications [120].

Recently, self-cloaked structures based on thoroughly different approaches have been proposed. In a recent study, it is shown that using the well-known Kramers-Kronig relations, the complex (real and imaginary part) dielectric constants can be determined so that the object, without any external cloak, can be rendered invisible [48]. Similar to transformation optics approach, however, fabrication of the resultant dielectric profiles are challenging, as there is a requirement for employing loss or gain materials. In an alternative approach, using Hilbert transform, it is shown that by employing isotropic materials, the spatial Fourier spectrum of the susceptibility of the given arbitrary object can be manipulated to engineer the scattering features in desired ways [49]. Nevertheless, the application of this method for larger objects leads to larger variations in the required refractive index profile making practical realization more difficult. Moreover, being made of dielectric materials, they are not suitable for applications where high electrical and heat conductivity are demanding. Another study proposed the usage of corrugated metallic wires to accomplish self invisibility [50]. However, being dependent upon the resonance characteristics of wires, the ideal performance is limited to a narrow frequency bandwidth. The realization of broadband, conductive and self-cloaked structures are clearly needed. Not only can they be of practical importance in non-invasive probes or cloaked sensors, but also in optical and microwave radiating systems where the required invisible regions can be much larger than the wavelength of the emitting sources.

In this Chapter, we theoretically and experimentally show that disordered networks of AgNWs with proper geometrical parameters can have near-minimal interaction with impinging electric fields in a wide range of frequencies. The mathematical description of scattering of impinging waves by such structures reveals the excitation of both localized and non-localized modes. Making the inclusions (nanowires) smaller leads to decoupling of the excited modes. Consequently, as we will show in next Section, the overall scattering is remarkably reduced and a near-invisible network of conductive nanowires is achieved. Another important benefit of using smaller nanowires is the higher uniformity which can be achieved in the deposition process [121]. This is highly essential in particular applications, like the one which we study in this work, where the AgNWs are employed to provide uniform electric fields over some specified regions. Also, the uniformity of applied electric fields by AgNWs is significantly enhanced by employing smaller nanowires [122].

As a particular example, we present an application where AgNWs are used to tune the conductivity of graphene in a designed multilayer structure. The employment of near-invisible AgNWs allows an effective application of gate voltage across the multilayer device. This way, the conductivity of graphene can be adjusted more efficiently than other approaches where usual metallic electrodes are used to apply gate voltage. We achieve a wideband modulation depth of about 70% which is a significant improvement to the performance of similar structures where a modulation depth of about 15% can be achieved using common metallic electrodes [123].

4.2 Operating principle

The multiple scattering of electromagnetic waves due to the interaction with strongly coupled objects can be described in terms of the fields scattered by each isolated element. This is mathematically modeled by the matrix operation as $[E_t]_{N\times 1} = [S]_{N\times N}[E_{isolated}]_{N\times 1}$, where N denotes the number of scattering elements and $[S]$ relates the total scattered fields by each object, $[E_t]$, to those by isolated objects, $[E_{isolated}]$, when there is no coupling between elements. This matrix model is used to describe or calculate the total field at any spatial location after the incident wave undergoes multiple scattering inside the structure. In the present work, we consider networks of highly coupled AgNWs. The optical waves interactions with AgNWs have been studied extensively. The main focus of these researches has been centered around the optical transparency, haze, and electrical conductivity of AgNW films with various physical properties including the geometrical sizes and orientations of wires. Here, considering the vectorial nature of incident and scattering waves, we investigate how the multiple scattering can affect not only the transmission of waves through the AgNWs, but also the vectorial characteristics of the scattered waves. We more specifically focus on electromagnetic sources with a frequency range lying in the 75-110 GHz band and their interactions with AgNWs with different geometrical parameters. Widely known as W-band, this range of frequencies enables high capacity point-to-point communication links. The scattering matrix, denoted by $[S]$, comprises all inter-element couplings described by sub-matrices $[s]_{i,j\ (i,j=1,2,\ldots,N)}$ in a given structure and features the mathematical properties of symmetrical and random band matrices. The singular value decomposition (SVD) of $[S]=[U][\Sigma][V]^T$, where $[V]^T=[U]^{-1}$, describes the total electric field in terms of the orthogonal eigenvectors where each vector indicates a particular field distribution inside a system of N coupled elements.

For a network of periodically arranged coupled nanowires the eigenvectors exhibit a significantly large number of non-zero elements, expanding over the whole length of the vectors. In other words, based on a measure introduced for the localization of chaotic eigenvectors [2], the multiple scattering of waves inside a periodic or ordered configuration of nanowires do not exhibit localized modes. The incident waves' interaction with such ordered structures results in scattered electric fields expanding over a large area of nanowires. On the other hand, by introducing randomness in the system, which can be done by changing the location and/or the orientation of wires in a random way, the localization length of eigenvectors starts to decrease significantly (Fig. 4.1). The distribution of eigenvalues (diagonal elements of $[\Sigma]$) is changed through modifying the scattering strength of individual elements, for example, by increasing/decreasing the physical size of AgNWs. Introducing stronger scattering elements leads to the enhancement of eigenvalues for the lower order modes (Fig. 4.2). Thus, the incident waves' interaction with percolated networks made up of wires with larger physical sizes (thicker wires) leads to stronger localized scattering fields. A similar effect is exploited in random lasers where random strongly scattering elements enhance the localization of the incident fields [7, 124]. Weaker scattering elements which can be realized by employing smaller (thinner) wires, on the other hand, reduce the localization or the strength of the localized scattering fields.

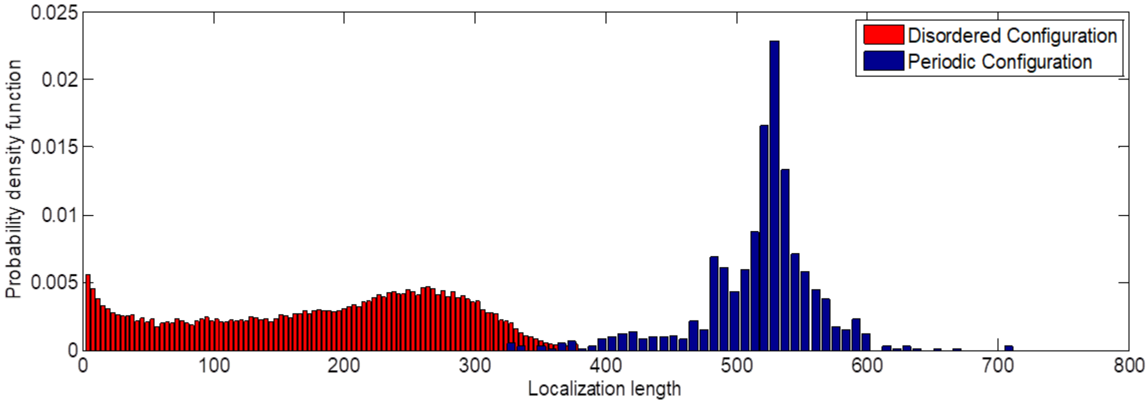

Figure 4.1: The graphs demonstrate the probability density function (PDF) of the localization length which is proportional to the effective number of nonzero components of eigen-vectors defined as [2]: $\exp(\mathbf{H})$, where $\mathbf{H}(\mathbf{u}_1, ..., \mathbf{u}_N) = -\Sigma_{i=1}^{N}|\mathbf{u}_i|^2 ln|\mathbf{u}_i|^2$, $\Sigma_{i=1}^{N}|\mathbf{u}_i|^2 = 1$ for each eigen-vector $(\mathbf{u}_1, ..., \mathbf{u}_N)$. The red graph shows the PDF of the localization length obtained for hundreds of randomly configured realizations each consists of 1000 silver nanowires (35 nm thick diameter and 15 μm length) dispersed over a square area of 80 μm by 80 μm. The blue graph shows the distribution of the localization length for a periodic configuration with the same number of wires.

Weaker scattering elements result in more uniform distribution for the eigenvalues (Fig. 4.2). In other words, the coupling between the induced modes described by $[V]([U])$ is reduced as the elements become smaller and scatter more weakly. Consequently, the total scattered fields become closer to the summation of those by isolated elements. Random orientation of AgNWs reduces the average coupling of the incident waves to such networks. Physically smaller elements, additionally, further reduces the scattered fields by isolated nanowires. The combined effect significantly reduces the scattering cross-section of percolated networks of small (thin) AgNWs, thus making them near invisible to the incident waves with sufficiently large wavelength.

In the next Section, we experimentally characterize the scattering features of the two groups of AgNWs using a standard W-band electromagnetic source. It is shown that sufficiently small AgNWs provide minimal coupling and exhibit negligible interaction with electromagnetic sources making them a perfect candidate for integration with such radiating devices.

Made of carbon atoms arranged in a mono-layer honeycomb lattice, graphene is known for its unprecedented combination of mechanical, electrical, and optical properties [125,

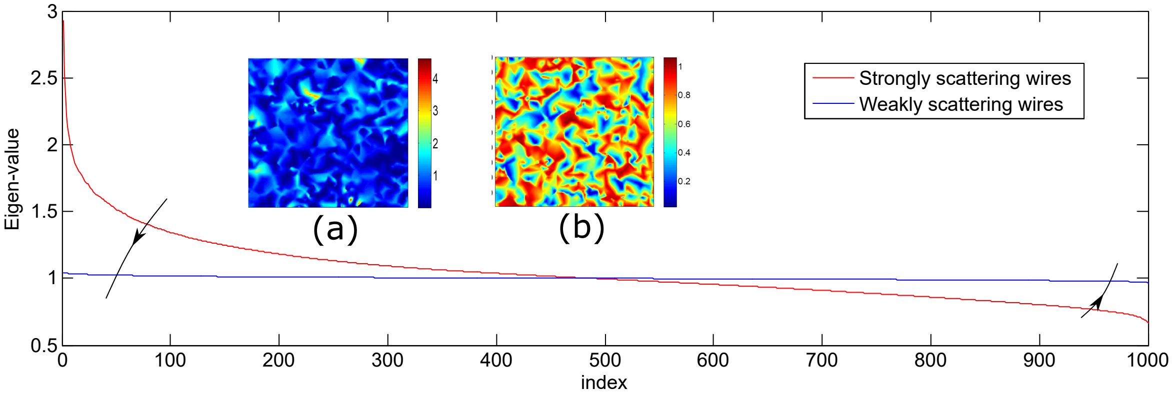

Figure 4.2: The distributions of eigen-values, diagonal elements of $[V]$, averaged over hundreds of randomly configured realizations each consists of 1000 silver nanowires. Strongly scattering wires exhibit a more localized distribution for the eigen-values. As a result, the interaction of incident fields reveals localized field distribution inside the network of such media. (a) shows the normalized scattered field intensity after the x-polarized incident field interacts with a percolated network of silver nanowires with 140 nm thick diameter and 15 μm length. (b) is the field distribution for a percolated network of silver nanowires with 35 nm thick diameter and 15 μm length.

126, 127, 128]. This has opened new avenues in developing novel graphene-based devices for emerging applications. An important characteristic of graphene is its tunable complex conductivity which is described by the Kubo formula [129, 130]:

$$\sigma(\omega,\mu_c,\Gamma,T)=\frac{je^2(\omega-j2\Gamma)}{\pi\hbar^2}\Big[\frac{1}{(\omega-j2\Gamma)^2}\int_0^\infty \varepsilon\Big(\frac{\partial f_d(\varepsilon)}{\partial\varepsilon}-\frac{\partial f_d(-\varepsilon)}{\partial\varepsilon}\Big)d\varepsilon \\ -\int_0^\infty \frac{f_d(-\varepsilon)-f_d(\varepsilon)}{(\omega-j2\Gamma)^2-4(\varepsilon/\hbar)^2}d\varepsilon\Big], \qquad (4.1)$$

where ω is the angular frequency of the interacting waves, μ_c is the chemical potential, Γ is the phenomenological scattering rate, and $f_d(\varepsilon)=(e^{(\varepsilon-\mu_c)/k_BT}+1)^{-1}$ is the Fermi-Dirac distribution. The conductivity of graphene can also be expressed as $\sigma(\omega)=\sigma_{intra}(\omega)+\sigma_{inter}(\omega)$. While the optical conductivity of graphene is dominated by carrier inter-band transition (described by the second term), at lower frequencies (millimeter-wave range) the intra-band transitions (described by the first term) determine the conductivity. The intra-band contribution can be described by an expression similar to that of a simple Drude model as $\sigma(\omega,\mu_c)=\sigma(\omega=0,\mu_c)/(1+j\omega\tau)$ where $\tau=1/2\Gamma$ is the carrier momentum scattering time. As $\omega\tau \ll 1$ in the frequency spectrum below the THz, the conductivity of graphene can be approximated by that in DC ($\omega = 0$) which can be controlled by changing μ_c. The chemical potential of graphene, μ_c, can be tuned through chemical doping [129] and/or by application of a gate voltage [131] or a magnetostatic field via the Hall effect [130]. For an isolated graphene sheet the chemical potential is related to the carrier density, n_s, through $n_s = \frac{2}{\pi\hbar^2 v_F^2}\int_0^\infty \varepsilon(f_d(\varepsilon) - f_d(2\mu_c + \varepsilon))d\varepsilon$ [129], where $v_F \simeq 9.5 \times 10^5$m/s is the Fermi velocity and the carrier density can be changed electrically or chemically.

In this chapter we demonstrate that near-invisible networks of AgNWs can play a prominent role in attaining highly tunable electromagnetic structures. We fabricated a millimeter-wave tunable radiating structure. A single layer graphene with a size of about 1 cm × 1 cm is employed as the tunable media. Using a gate voltage approach to tune graphene conductivity, terahertz modulation depth ranging from 15 % to 64 % are reported [123, 132, 133, 134]. However, the bandwidth is reduced by increasing the modulation depth in these works. Recent attempts to increase the modulation depth, without sacrificing the bandwidth, require the employment of strongly scattering structures to modify the field interactions with graphene [135]. The design and fabrication complexity of these approaches makes them too expensive to be generalized to broad range of applications. However, in this work, employing AgNWs to apply gate voltage has proven to be an effective low-cost approach. To support the structure and avoid the attenuation of incident electromagnetic fields, a high resistivity silicon wafer is used as the substrate. A gate voltage is applied to AgNW films at both sides of the graphene layer, and aluminum oxide (Al_2O_3) is employed as a low loss dielectric spacer [136] and a passivation layer which is effective in stabilizing the graphene characteristics over several months in ambient atmosphere [137]. The relationship between gate voltage and the chemical potential can be obtained according to gate capacitance [138] as $C_d\Delta V_g = A_d(e\Delta n_s)$, where C_d is the capacitor formed by the layers of AgNWs and graphene with Al_2O_3 between them and A_d is the surface area of the capacitor. Changing V_g will induce charge on the surface of graphene. The induced charge is associated with a change in carrier density which is related to the chemical potential and the conductivity of graphene.

Adopting proper AgNWs not only preserves the desired radiation characteristics of antennas but also provides more freedom in enhancing other designs characteristics. Increasing per unit area capacitance, in the presented application, enables high tunability of carrier density in the graphene sheet and thus a higher dynamic range in the modulation depth. In the next Sections, we explain both the AgNWs and design characteristics.

4.3 Results and Discussion

4.3.1 AgNWs' characteristics

To evaluate the electromagnetic field interaction with AgNWs, two groups of AgNWs with average diameters of 35 nm and 90 nm with average lengths of 15 μm and 25 μm, respectively, are investigated. The nanowires, dispersed in ethanol, were supplied by Blue Nano Inc (Charlotte, NC). Using the Mayer rod coating method [139], the AgNWs are uniformly deposited on two 2 cm × 2.5 cm polyethylene terephthalate (PET) substrates and annealed at 150 °C for 15 minutes to reduce the junction resistance between nanowires and thus reduce the overall sheet resistance. The sheet resistance of the samples was measured using the 4-point probe method. A 10 nm gold layer was sputtered on the samples for scanning electron microscopy (SEM) imaging. The fill factor of the AgNWs was determined by image processing of the SEM images and calculating the ratio of the covered area. When coated on a plastic substrate and dried, the resultant film is a percolated network of AgNWs. Sufficient number of nanowires leads to a highly conductive film which is as a result of overlapping AgNWs (Fig. 4.3). For both types of prepared samples, an areal coverage of 8±2 % and an average sheet resistance of 45 ±5 Ω/sq were obtained.

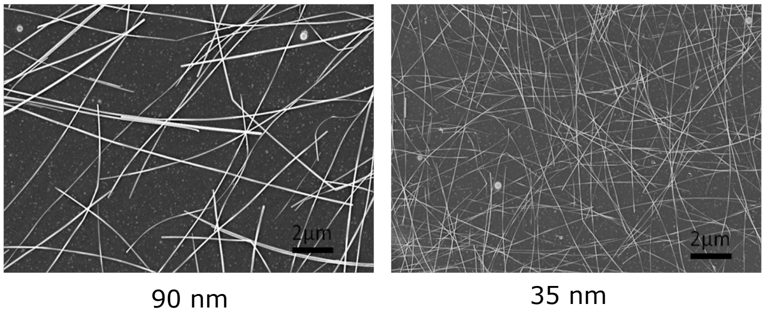

90 nm

35 nm

Figure 4.3: Electrodes made from AgNWs with different diameters.

To characterize the AgNW networks in the millimeter wave portion of the electromagnetic radiation spectrum, a measurement setup shown in Figure 4.4 was used. A standard gain horn antenna (SGH) in the frequency range of 75 GHz to 110 GHz, provided by Nearfield Systems Inc. (NSI) [140], with an aperture size of 2.46 cm ×1.88 cm is used as a standard millimeter wave radiating source. An open-waveguide probe is used to measure the radiated electric field tangential components, x and y, over a scan window at a distance of 8 cm from the aperture of antenna over an area of 30 cm × 30 cm. The resolution is chosen to be 0.2 cm in both x and y directions. We performed the measurements in three steps. The first step is to calibrate the system. To test the correctness of the calibration step, the radiated field of the SGH is measured before the samples are placed in front of the SGH. The measurement results of the SGH for frequency points of 85 GHz and 100 GHz are summarized in Appendix C. As expected and can be seen, the measured radiation patterns are in good agreement with those presented by analytic formulations [141]. In the second step, in order to distinguish the effect of the AgNWs themselves, it is necessary to measure the combined effects of the bare plastic substrate and the paperboard holder, with respect to which, the scattered fields in the presence of coated samples will be studied. The same measurement setup should be used for the coated substrates. With an uncoated substrate in front of the antenna, the measurement results are shown in Figure 4.5 (for 85 GHz) and Appendix C. The results are not as symmetric as those of isolated SGH. This is mainly because of the asymmetry in the paperboard holder. The presence of the substrate leads to a small reduction in the side-lobe levels, especially at higher frequencies.

The last step is to repeat the previous measurements with coated substrates. The results of 35 nm and 90 nm AgNWs are summarized in Figure 4.5 (for 85 GHz) and Appendix C. Comparison between the measured data confirms that increasing the electrical size of nanowires leads to stronger scattering fields and therefore larger deviation from the desired radiation characteristics of the isolated standard antenna. For the group of nanowires with an average diameter of 35 nm, the results reveal a successful realization of a near-invisible film featuring very negligible interaction with the radiated fields of the SGH. Figure 4.5 shows the results for 85 GHz with an average error of less than 1% introduced by AgNWs. Based on this, in the next Section we choose the 35 nm AgNWs with an 8±2 % filling factor as investigated above, to control the conductivity of graphene in the millimeter-wave range of frequencies from 75 GHz to 110 GHz.

4.3.2 Graphene-based radiating structure characteristics

Figure 4.6 shows the fabricated device. The graphene, which is electrically accessible through two gold contacts, is sandwiched between two low loss dielectric (alumina) layers with 175 nm thickness. The substrate is 500 μm thick high resistivity silicon wafer with bulk resistance of about 10^5 Ωcm at room temperature ($T = 300$ K). The top and bottom layer of the structure is coated with AgNWs (average diameter and length of 35 nm and 15 μm, respectively, and 8±2 % filling factor) and serve as near-invisible controlling electrodes.

Applying a voltage, ranging from 0 to 20 V, to the top and bottom silver contacts, with the mid layer contact grounded, the conductivity of graphene changes from 6 mS to 0.72

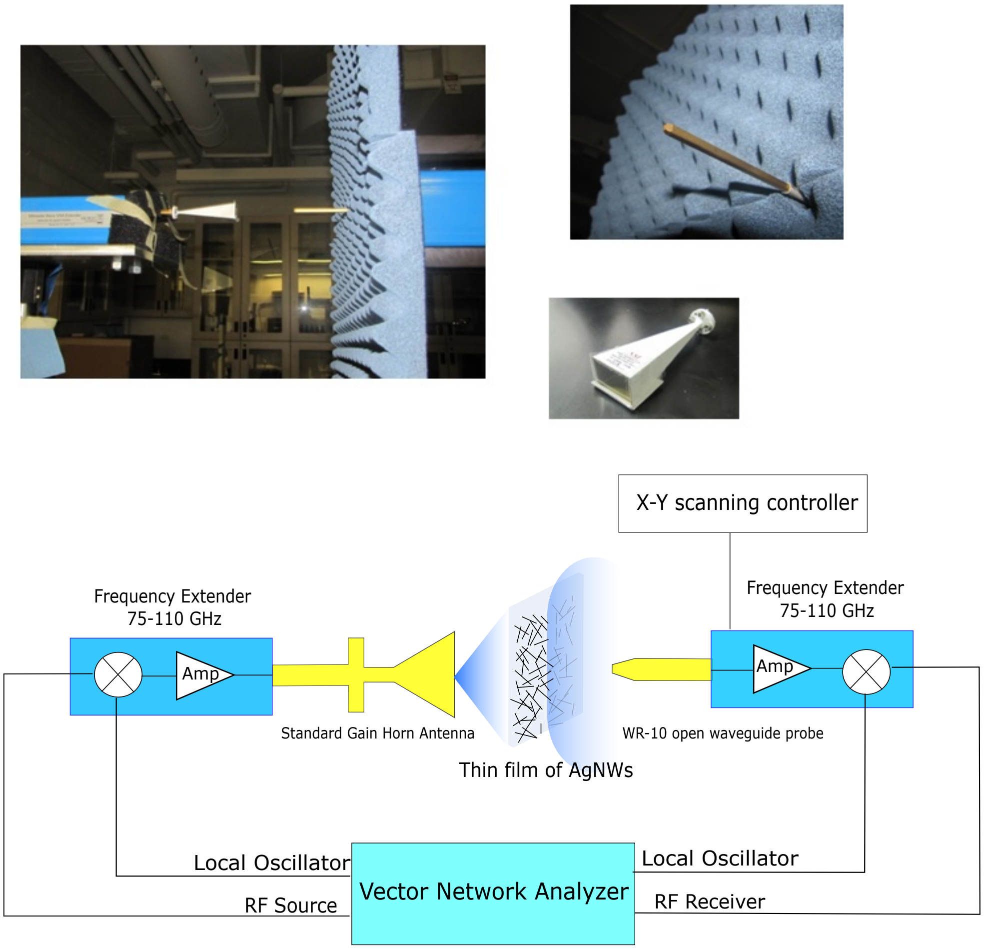

Figure 4.4: Near-field measurement setup. A standard gain horn (SGH) antenna in the frequency range of 75 GHz-110 GHz is used as a radiating source. Samples are placed in front of antenna using a paperboard holder. An open-waveguide is used as a probe to measure the radiated fields over the scan window with specified resolutions.

mS and consequently the transmission of the waves passing through the structure will be affected accordingly (Fig. 4.7(a)). As a result of increasing the voltage, the conductivity of graphene decreases and the reduced conductivity leads to a minimal change in the received signal captured by a receiver probe antenna located on the other side of the device. On the other hand, for low voltages, the increased conductivity of graphene increases atten-

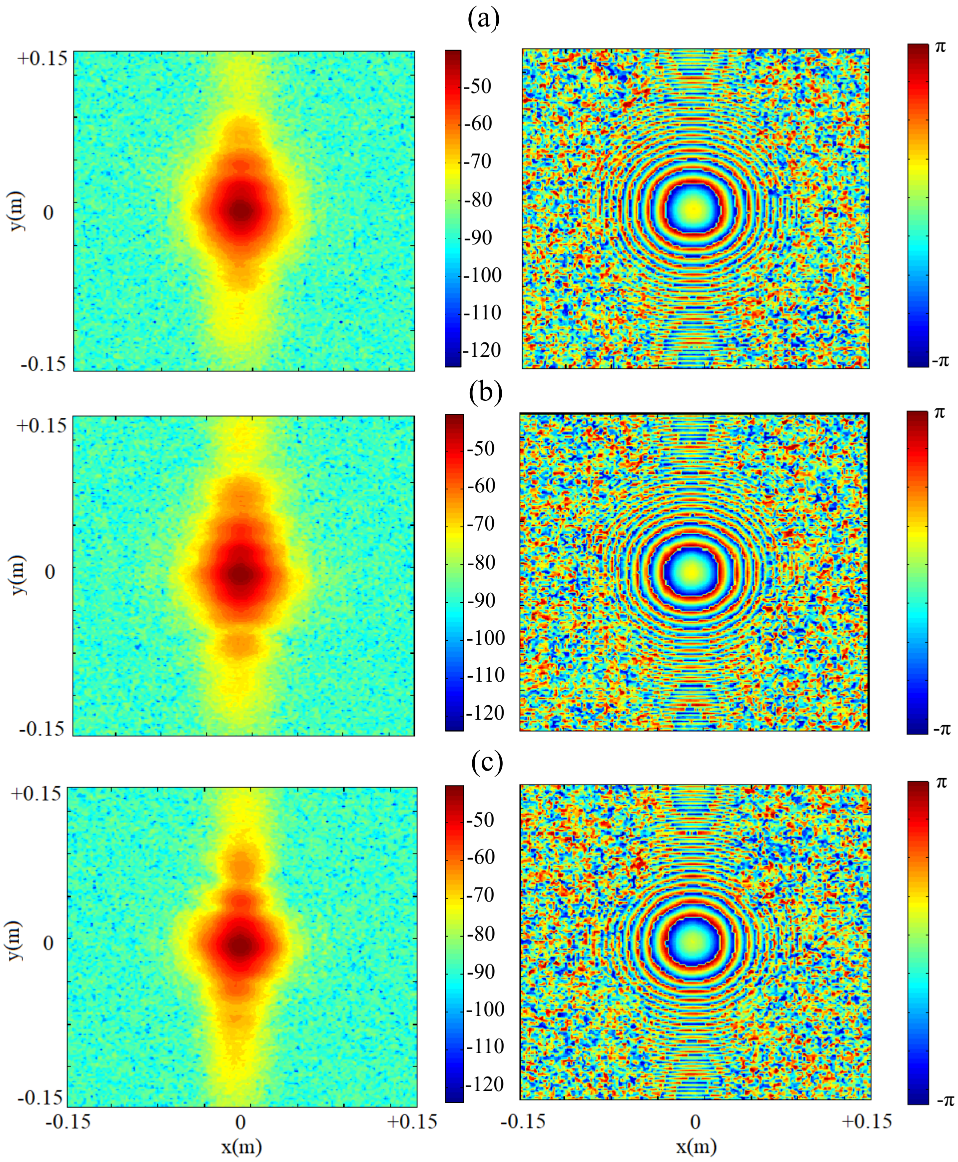

Figure 4.5: The measured electric fields (intensity (dB) and phase (rad)) at 85 GHz in the presence of AgNWs with average diameters of 35 nm (b), and 90 nm (c). Comparison with the radiated fields from the SGH in the presence of bare (non-coated) plastic substrate, (a), reveals superior performance of 35 nm AgNWs in not disturbing the initial incident field (less than 1 percent error with respect to (a)).

uation and modulates the transmitted waves through the device. There is an oscillatory response in the transmission which is partially attributed to the Fabry-Perot resonances of the structure and that of the facing measurement probe antennas. To maintain uniform illumination of the sample and to eliminate the resonance effects, we limit the frequency window of measurement to 80-84 GHz. Within this bandwidth, the transmission characteristics in the absence of sample indicates a close to flat response. It is important to note that not all the power captured by the receiver antenna stemmed from the interacting waves with graphene. This effect, which is frequency dependent, can be estimated as an average attenuation constant in the difference in power received for $Vg = 0$ with respect to $Vg = 20$ V. This is in excellent agreement with both the measured and simulated results where we consider the experimentally determined parameters. Removing the effect of the substrate in the normalized data, the attenuation imposed on the transmitted field through the graphene layer can be calculated (Fig. 4.7(d)). As expected, a near constant value is obtained confirming the underlying theoretical assumptions of the simple Drude model for graphene and previous experimental observations in the terahertz range of frequencies [123]. Figure 4.7 summarizes the results. As it is shown, a modulation depth (defined as $|(T(20\text{ V})\text{-}T(0\text{ V}))/T(20\text{ V})|$) of 72% in the range of 80-84 GHz is achieved. Although the measurements are performed and reported in a limited frequency range, which is mainly due to the measurement setup limitations, high modulation depth over a broader range of frequencies is achievable as both the AgNWs near-invisibility feature and graphene characteristics remain the same at lower and higher frequency ranges. Regarding the modulation speed, which is not the focus of the presented application of near-invisible nanowires, it is important to mention that due to the chosen fabrication process, the resistance of the AgNW network at the exposed area on the edge over the bottom layer is significantly higher than the remainder of the electrode. This area, which is left uncoated for the sake of convenience in the measurement process, is exposed to liquids in the process of wet transfer of the graphene sheet on top of the first dielectric layer. This leads to resistances in the order of hundreds of kΩ which for the current device with the total capacitance of approximately 0.05 μF gives RC time constants corresponding to the modulating frequency range of 100 to 363 Hz. To overcome this drawback, for the same fabrication process, the exposed area on the edge can be covered by uniform silver paste which can be done in the first step of fabrication (see the fabrication process). Moreover, decreasing the area of device reduces the capacitance and thus increases the maximum frequency of modulation.

4.3.3 The fabrication process

A 500 micrometer thick high resistivity silicon wafer (10^5 Ωcm at $T = 300$ K) is used as the substrate. Layers of AgNWs, graphene and aluminum oxide are deposited as described below.

- The bare silicon substrate was coated with the first layer of AgNWs with average diameter of 35 nm and length of 15 μm in the same manner as on the plastic substrates with an average sheet resistance of 45 ±5 Ω/sq. To lower the sheet resistance of the NW film the sample was heated to 150 °C for 15 minutes.
- Using an e-beam evaporator, aluminum oxide with a thickness of 175 nm is deposited over the selected area on top of the AgNWs using a shadow mask. A narrow strip is left uncoated on top of the AgNWs. This strip served as one of the metallic contacts.
- A 1 cm × 1 cm single layer graphene sheet, purchased from ACS Material, is transferred onto the middle of the aluminium oxide layer. Following the instructions provided by the vendor [142], after the wafer is dried and baked at 100 °C for 30 minutes and 20 minutes, respectively, it is immersed into acetone to remove the PMMA layer on top of the graphene sheet for about 30 minutes.
- After the wafer is dried, two gold contacts are deposited to provide the connection of graphene layer with ground. Using the e-beam evaporator, a 5 nm thick film of titanium (Ti) is first deposited to cover the area specified by the shadow mask, then gold with a thickness of 70 nm is deposited on top of the titanium. Titanium serves as the adhesion layer below the gold contacts.
- Using the e-beam evaporator, aluminum oxide with a thickness of 175 nm is deposited over the selected area on top of the graphene and gold contacts. The exterior parts of gold contacts are left uncoated to provide the external connections.
- Finally, on top of the aluminum oxide layer deposited in the previous step, a second layer of AgNWs with the same characteristics as the AgNWs of the first layer, is deposited over the specified area. This layer serves as the top surface of the capacitor.

The fabricated sample is shown in Fig. 4.6. For the measurement setup a printed circuit board was designed to extend the metallic contacts to make the measurement process easier.

4.4 Conclusion

Networks of disordered nanowires can support EM modes with reduced localization lengths. The scattering strengths of particles determine how localized the scattered fields can become. Sufficiently small particles lead to the uniform excitation of decoupled orthogonal modes, thus the total scattered field becomes the summation of those by isolated particles. Based on this fact, we demonstrated that percolated networks composed of randomly oriented AgNWs with proper geometrical sizes introduce negligible disturbance to the incident EM fields, from 75 GHz to 100 GHz, and thus a near-invisible electrode is achieved. As a particular example, the application of such structures in a radiating tunable device is investigated. A graphene-based modulator is experimentally studied where high tunability (72 % modulation depth) is achieved. This is a 4-fold enhancement with respect to other approaches reported previously. Although the bandwidth of the measurements carried out in this work is not very large due to the limitation imposed by the measurement setup, the desired features of invisibility of AgNWs and tunability of graphene are expected to exist over wider range of frequencies.

4.5 Statement of contributions

Mohammad Haghtalab developed the concept, designed the structure and performed the e-beam evaporations, experiments and simulations. Mohsen Raeiszadeh provided help in the design, fabrication and transferring the graphene layers. Hadi Hosseinzadeh provided and characterized the AgNW samples, coated the fabricated devices by AgNWs, and performed the SEM imaging of electrodes. Gholamreza.Z Rafi provided help in near-field measurements of AgNW samples. Aidin Taeb fabricated the shadow masks. Hussam Al-Saedi fabricated the PCB. Jared Sisler drew the graphics of Fig. 4.6. Michele Tamagnone provided help in analysing the measurement results. Mohammad Haghtalab acknowledges the technical supports provided by Professor Irene Goldthorpe.

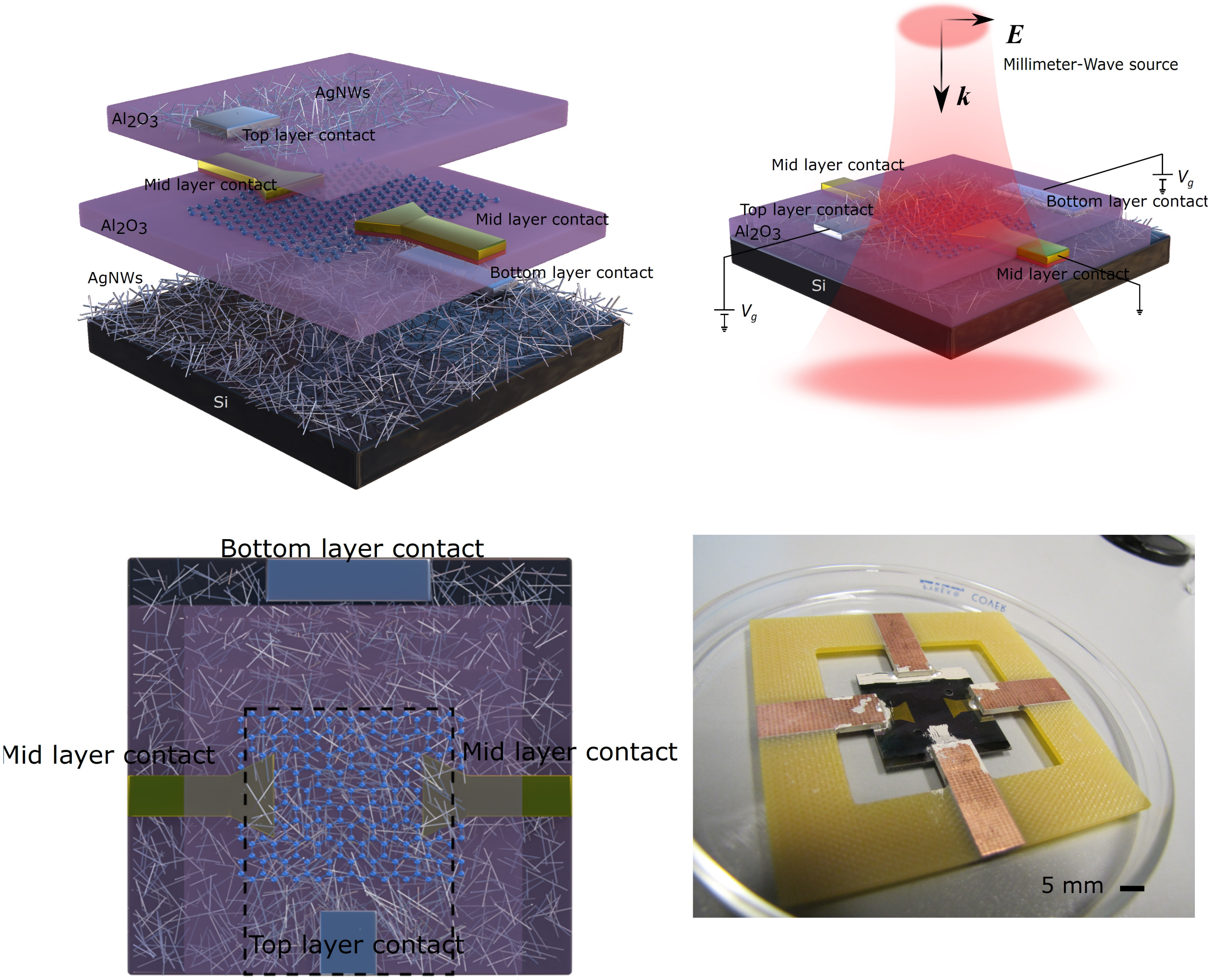

Figure 4.6: The schematic of the graphene-AgNW based tunable device. (a) shows the constituent layers: high resistivity silicon is employed as the substrate for depositing the first layer of AgNWs. The two mid layer contacts are used both to measure the conductivity of graphene located between the layers and to provide a path for electrons flowing to/from the graphene sheet. The second layer of AgNWs is deposited on top to cover the area occupied by graphene. The top and bottom layer contacts are used to apply the controlling voltage. (b) shows the top view, (c) illustrates the device under illumination, and (d) is a photograph of the fabricated device where a printed circuit board (PCB) is used to provide external connections to the metallic contacts.

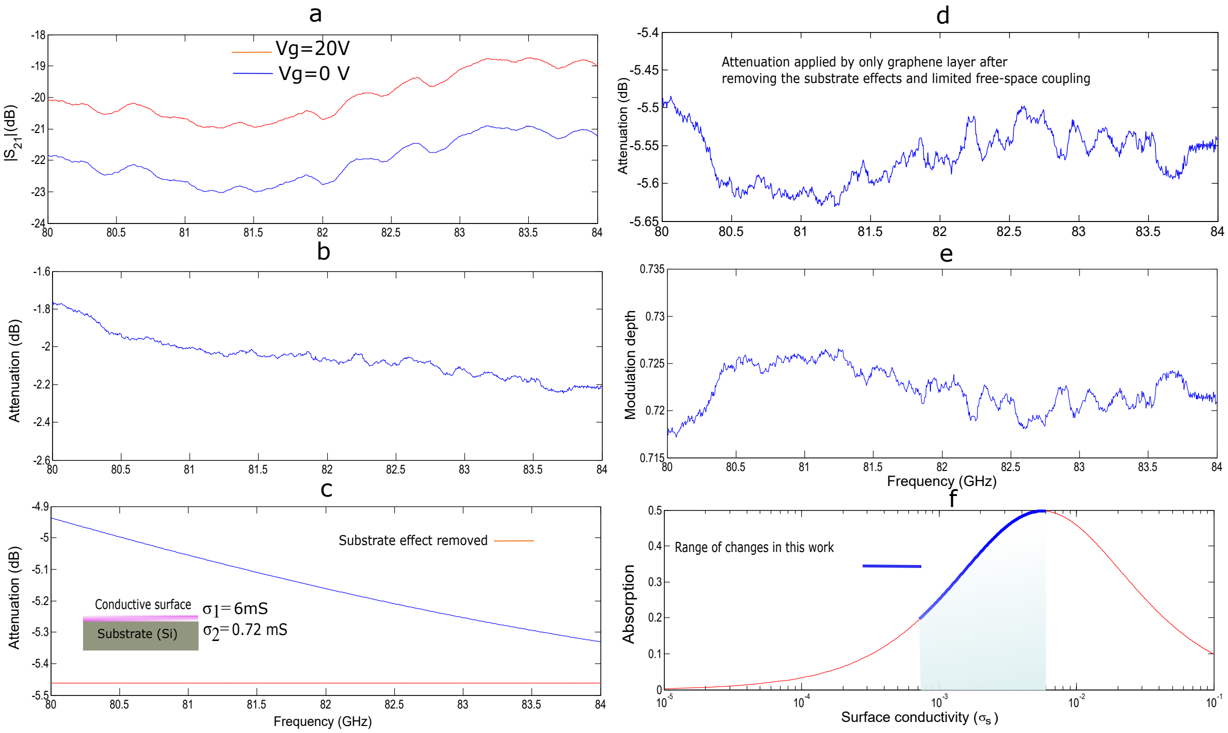

Figure 4.7: The measurement results. (a) shows the insertion loss ($|S_{21}|$ (dB)) measured for $V_g = 0\ V$ and $V_g = 20\ V$. (b) indicates the measured attenuation applied on the input signal form the port 1. This is obtained by subtracting the $|S_{21}|$ of two measured signals in (a). In the next step, based on the measured conductivities, the effect of substrate is removed (c). Finally, considering the effect of limited coupling of the input signal from the port 1 to the graphene sheet, which is appeared as an average attenuation constant over the limited frequency range of 80 GHz-84 GHz, the attenuation applied by "only" graphene layer is calculated and shown in (d). This corresponds to a modulation depth of approximately 72 % over the graphene sheet(e). (f) shows the range of conductivity change measured in this work and the corresponding absorption by graphene sheet.

Chapter 5

Self focusing disorder engineered metastructures by near optimal freeform inverse design (NOFID) approach

Demands for new classes of metastructures featuring multifunctionality as well as high efficiency require the employment of designs with high degrees of freedom. Due to large number of variables, using the conventional global optimization methods is not efficient in such structures. To overcome this challenge, we employ the novel optimization approach, developed in Chapter three, which allows us to efficiently explore electrically large and geometrically complex structures. We investigated geometrically complex disorder engineered metastructures with applications from super-resolution imaging and communication to near-invisibility electromagnetic cloaks. In this Chapter, based on the proposed stochastic-based algorithm, we explore self focusing structures composed of ultra subwavelength metallic wires. The proposed structures and approach hold promise for a wide range of applications such as random lasers.

5.1 Introduction

Metastructures have enabled unprecedented engineering of light-matter interaction through designs which are composed of arrays of sub-wavelength-scale scatterers. Not only have they been shown to be perfect alternatives to the conventional bulky optical devices [35], but also, new functionalities have been demonstrated [36, 94] which are either impossible or difficult to achieve through conventional devices. These breakthroughs are made possible by the ability to manipulate the phase and the amplitude of the incident fields over each unit cell of these structures independently; thereby controlling the wavefront in desired manners. The proposed design approaches are based on engineering the interaction of incident fields with the coupled scattering elements within each unit cell and can be classified by the type of the elements utilized in these structures, namely resonant or non (weakly)-resonant elements. Depending on the type of the elements of choice, there are limitations in terms of the maximum efficiency which can be achieved in designs with various specifications. These limitations are imposed either due to the undesired inter-cell couplings throughout the structure or the intrinsic resonant characteristics of the resonating elements employed in the design. As such, new techniques for designing metasurfaces with higher efficiencies have been proposed [143, 38]. Thus far, the most common type of the proposed metasurfaces operate based on introducing abrupt changes of optical/electromagnetic properties at an interface utilizing dielectric or metallic nanostructures [144]. The collective effect of all unit cells leads to the desired functionalities such as lensing over a desired region in space. While the inter-cell coupling is not desired and can cause significant drop in efficiency in these designs, new proposed approaches take advantage of strong inter-element couplings throughout the structure to alleviate the fundamental limitations of conventional designs. These approaches require the consideration and optimization of the coupling between large numbers of elements. Different methods have been utilized to overcome this challenge by introducing/employing new optimization approaches.

Achieving novel functionalities and/or enhanced efficiencies through modifying existing devices or developing new designs require making use of large degrees of freedom in the design space. Some of the proposed designs feature geometrically complicated structures providing high dimensional solution spaces to explore, however, at the expense of large computational complexity. In addition to the large number of variables, one of the properties of such problems is the existence of multiple (non-uinique) solutions. As such, proposed methods like those based on topology optimizations make use of the method of gradient descent where the initial solutions are iteratively modified to reach to an optimum solution appearing in the form of local minimum or maximum in the solution space. On the other hand, large number of variables prevents the efficient implementation of the conventional global optimization techniques.

In Chapter three, we proposed a novel approach to optimize geometrically complex disordered structures for super-resolution imaging and communication. The method takes a new stochastic-based approach which is based upon a series of controlled iterative perturbations and modifications to the solutions which ultimately converge to a near-optimum design. Starting from an initial state (solution), the primary solution undergoes probabilistic changes through an iterative approach. This process is controlled by defining different parameters which ultimately leads to the optimization of the defined cost function(s). As shown in Chapter three, the proposed technique exploits infinitely large degrees of freedom in positioning scattering dielectric objects to fulfill the desired functionality in the ultimate design. Comparison between the performances of the designed structures with respect to their regular (periodic) counterparts reveals the significant improvement which can be achieved by engineering disorder.

Engineering disorder has become a powerful approach in various applications such as omnidirectional anti-reflection coatings, imaging through complex media, spatial light modulator (SLM) assisted super-resolution optical lenses, and optical coding through disordered nanoantennas. Random lasers are among the most well-known applications of disordered structures where the enhanced amplifications of incident fields through localized modes triggered by multiple scattering process is harnessed for lasing. Despite the advantages offered by random lasers such as being inexpensive and easy to fabricate, there exist a number of issues regarding the controllability of the direction of emitted lights as well as the spatial profile of the excited modes [7]. New strategies have been proposed which aim at engineering the excited localized modes to enhance both the directionality and the spectral stability of emission. It has been shown that through reducing the effective physical dimension of the region where the incident fields undergo multiple scattering, the excitation of localized modes can be enhanced and controlled for improving the emission characteristics. Here we address this problem through designing disorder in a general three dimensional structure. It is shown that the infinite degrees of freedom in positioning and selecting the orientation of scattering elements can be exploited to achieve multi-functional high performance devices. We investigate the most general form of three dimensional disordered metastructures composed of subwavelength wires arranged and stacked in a multilayer fashion. Choosing small wires provides more control over the polarization of the scattered fields by each particle within the structure. In the following Section, an example of a designed structure is investigated in more details.

5.2 Results

We assume metallic wires with length of 6 mm and diameter of 200 μm. Using the NOFID algorithm, the wires are aligned and placed at different locations inside a square region with the side length of 3 cm. A multilayer scheme is assumed; this means that in the vertical direction which is normal to the plane of the square region, the wires are located at specified equi-spaced planes (25 μm apart). Considering a wavelength of 10 cm, the cost function in the optimization process is defined to maximize the localization (both the strength and the spatial extent) of the incident electric fields for a range of polarizations changing from x-polarized to y-polarized illuminations. The final design consists of 295 wires arranged in 7 layers as shown in Fig. 5.1. The magnitude of total fields are plotted in Fig. 5.2. As it is shown high concentration of fields can be achieved for both polarization of incident fields. The localization length in both x and y direction is approximately $\lambda/50$ with an enhancement factor (defined as the ratio of the total field with respect to the incident field) of 65 and 30, for x and y polarized incident fields, respectively.

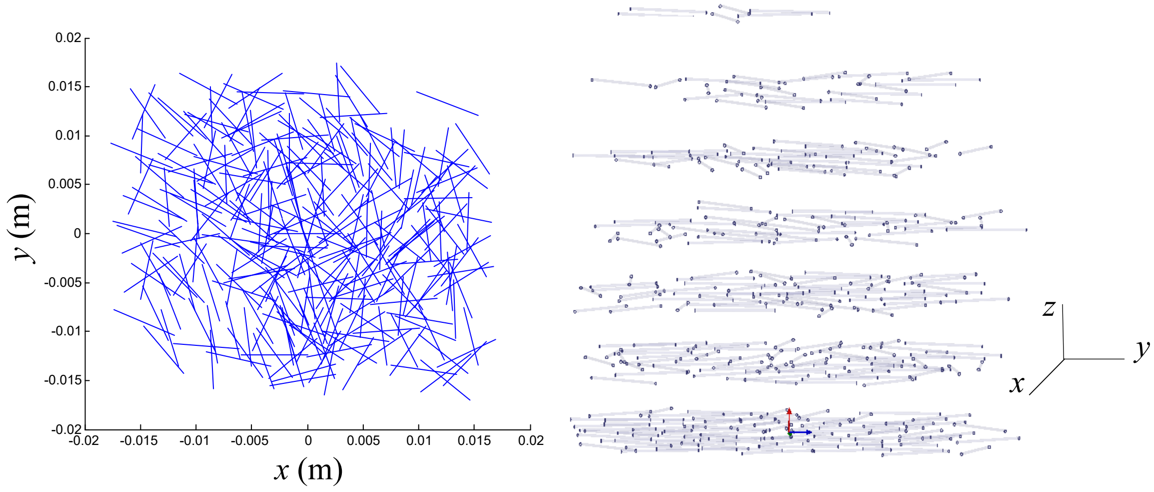

(a)

(b)

Figure 5.1: (a) and (b) show the top and side views, respectively, of the designed structure consisting of 295 wires.

5.3 Conclusion

The observed results reveal the high potential of disorder engineered structures in achieving design characteristics which are difficult, if not impossible, to obtain through regular structures. As an example, we designed a complex metallic wie medium featuring self-focusing for incident waves with different polarizations using the developed algorithm. We foresee the application of such an approach in the design procedure of future devices.

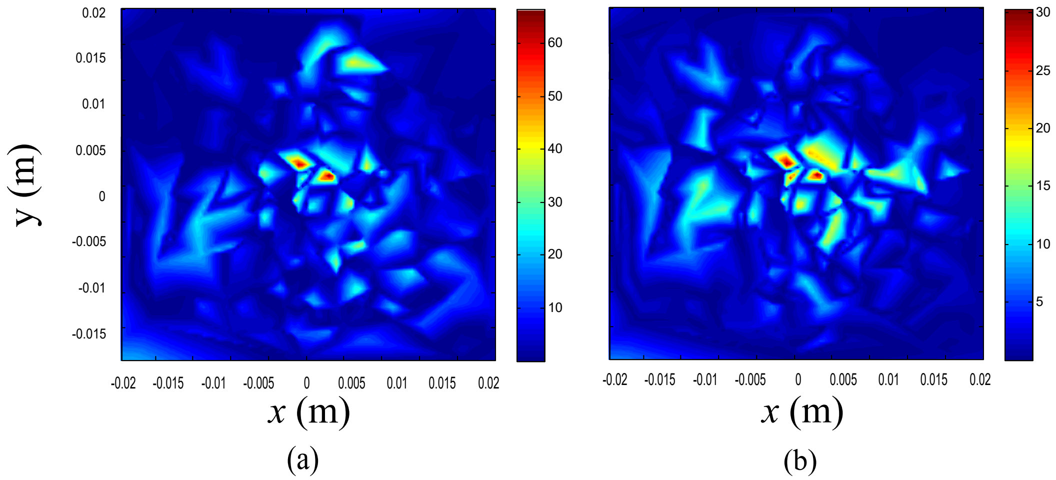

Figure 5.2: (a) and (b) show the magnitude of the total fields in the close vicinity of the designed structure consisting of 295 wires for x and y polarized incident fields, respectively.

Chapter 6

Future Work

We presented some new applications/concepts realized through disorder engineered electromagnetic devices. In optical range of frequencies, we introduced a new scheme for multiplexing which is based on disordered optical nanoantenna structures. All dielectric structures were also investigated to realize super-resolution imaging/communication. Structures composed of strongly coupled metallic wires have been investigated. In the millimeter wave frequencies, we designed and fabricated a preliminary silver nanowire/Graphene based multilayer structure. The near invisibility feature provided by the selected type of silver nanowire conducting films is used to control the conductivity of graphene without affecting the radiation characteristics of radiating sources. Networks of strongly coupled larger metallic wires have been designed to realize self-focusing devices for incident fields with arbitrary polarization.

The general outline for the future work can be summarized as follows:

- Adapting fast and accurate computational methods for analysis and optimization of field interaction with disordered structures composed of a large number of nonidentical scattering objects.
- Extending the introduced concept of orthogonal transmission channels realized by disordered optical nanoantennas both theoretically and experimentally.
- Modification of silver nanowire/graphene based structure.
- Extending the designed one dimensional disordered dielectric structures to three dimensions and experimental verification and implementation.
- The application of NOFID in design optimization of future devices.

6.1 Fast and accurate computational methods for the analysis and optimization of field interaction in multiple scattering problems

Disordered structures, in general, may consist of a large number of scatterers, each with different physical properties. Analysis of field interaction with such complex systems is a challenging process which makes the design optimization process more difficult. The development of a fast and accurate numerical technique which, firstly, is capable of solving large scattering problems using fewer number of unknowns and, secondly, provides a fast numerical approach to calculate the inverse matrix which appears in the integral equation formulation in these types of problems is highly demanded. Figure 6.1 shows a general configuration in a multiple scattering problem. The resultant matrix equation has a form of

$$\mathbf{E_i} = [A]\mathbf{E_t}, \tag{6.1}$$

where $\mathbf{E_i}$ is the incident electric field and $\mathbf{E_t}$ represents the total electric field at the location of scatterers. As it was also shown in the previous Chapters, to obtain the total field, the inverse of $[A]$ should be calculated. If the properties of some scatterers are changed, normally, the matrix $[A]$ and its inverse should be calculated for the updated system. The development of a method which makes the recalculation process of matrix inversion faster in a multiple scattering problem will significantly accelerate the analysis and the subsequent design optimization process.

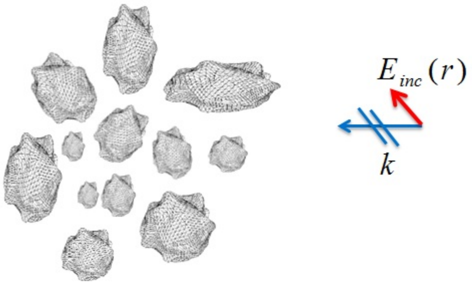

Figure 6.1: The general configuration of a multiple scattering problem with a large number of nonidentical objects.

6.2 Disordered optical nanoantennas

In the second Chapter, we showed that for a given arbitrary configuration of coupled nanoantennas, orthogonal transmission channels can be found and implemented. However, depending on the configuration, the maximum number of channels might be limited for a fixed given structure. The question is how we can implement larger number of orthogonal channels using more than one antenna pattern each occupying a given area with a different configuration. When illuminated by phase modulated incident fields, the field distribution over the output planes of these configurations should be orthogonal to form orthogonal sets of antenna configurations. As a part of the future work is to investigate the implementation of orthogonal channels using more than one configuration instead of one.

6.3 Disorder engineered dielectric structures

In the third Chapter, we studied one dimensional dielectric structures. The modification of the study to the three dimensional dielectric structures is straightforward and important for practical scenarios.

6.4 Near invisible networks of metallic wires

In the fourth Chapter, we investigated the design and fabrication of a controllable spatial wave modulator in the millimeter wave range of frequencies. Near invisible films of silver nanowires were employed to increase the efficiency in tuning the designed modulator. As also mentioned before, one drawback of such structures could be the high resistivity of the silver nanowire films. This can be modified through modifying the fabrication process or employing thicker nanowires. The latter, however, comes at the expense of imposing stronger attenuation on the incident waves or introducing unwanted scattering fields. To overcome these issues, at least in lower frequencies, we can employ the optimization algorithms to “ design” such networks of wires to minimize the undesired effects and, at the same time, maintain the invisibility feature to enhance some design characteristics such as the tunability.

6.5 Ultimate metastructures using NOFID

We presented a few applications of the developed algorithm, NOFID, to design new devices with various functionalities. This approach can be used to design broader range of structures, where new functionalities and improved efficiencies can not be achieved through conventional approaches/ structures. Examples include multifunctional and/or non-reciprocal electromagnetic devices.

APPENDICES

Appendix A

Orthogonal transmission channels in disordered optical nanoantennas

A general configuration of nanoantennas is shown in Fig. 2.1. The gold nanoantennas with arbitrary shape are placed on the interface between region 1 and region 2 (substrate). The antenna is illuminated by an electromagnetic plane wave coming from the region 2. The incident fields undergo phase modulation at the location of nanoantennas over the input plane shown in Fig. 2.1 (a). If we have "N" number of pixels defined on both input and output planes, mathematically, the values of the amplitude and phase of incident field at each pixel over the input plane can be obtained so that the same number (N) of orthogonal vectors are realized at pre-specified regions over the output plane. This can be expressed in a matrix form as

$$[E]_{Output} = [T][E]_{Input} \tag{A.1}$$

$[E]_{input}$ is a N×1 vector where each entry is a complex (amplitude and phase) value of one sample of the incident field over the input plane at the location of defined pixels. $[T]$ is a N× N transmission matrix and $[E]_{output}$ is a N×1 vector which contains the values of electric field at N points over the output plane. Multiplying both sides by the inverse of $[T]$, one can obtain the required incident field over the input plane which gives rise to desired values for the field over the output plane at the specified points. Each column of the inverse matrix $[T]^{-1}$ corresponds to one specific pixel on the output plane and gives the required amplitude/phase modulation over the input plane to excite that point while the values of field at all other points (on output plane) are zero. In other words, each column corresponds to a specific point on the output plane while the values of electric field at all those points are given by $[E]_{output}$.

We are interested in finding the orthogonal channels each excited by a specific phase-only modulated electric field. Each column of $[T]^{-1}$ consists of N complex numbers (excitation elements) giving the samples of incident field over the input plane to excite one channel. If the excitation elements have the same magnitude, the corresponding point (region) over the output plane is considered as one of the orthogonal channels which can be excited by a phase modulated electric field. But, in a general structure, not all the columns have this property. Linear combination of those columns which have elements with different magnitudes, can lead to a new group of excitation elements which is desired , i.e. all the elements have the same magnitude. In other words, the corresponding points (regions) (associated to the combined columns) on the output plane are excited simultaneously. Depending on the distances between these excited points (regions) a "non-localized" or "localized" transmission channel is formed.

As explained in Chapter 2, to identify the possible channel regions, the results of a large number of simulations are analyzed. The phase value at each pixel near the gold nanoantennas is randomly drawn from the uniform distribution function on the interval $[0, 2\pi]$. Accumulating the absolute values of electric fields over the output plane indicates the regions where the diffracted fields are most likely to focus (Fig. 2.8 (b)). The high intensity regions are associated with resonating local nanoantennas and are candidates for the localized transmission channels. As we have shown in Chapter 2, the field strength near a local resonating nanoantenna is mostly influenced by the nearby elements. Optimizing the phase distribution over the input plane can be performed in such a way that we achieve to a maximized value (better than 40 dB in our work) for the ratio of electric field at a desired channel spot to that at other channels locations. Repeating this procedure for all channels we obtain a set of phase distributions $\{\exp(j\phi_{i(x',y')}); i = 1, ..., N\}$ which can be used to multiplex/demultiplex signals (Fig. 2.1(b)). Shown in Fig. 2.9 are the realized localized channel's field distribution over the output plane. Each spot shown by a circle in Figure 2.8 (b) represents a localized transmission channel carrying the corresponding information symbol. If we choose to increase the number of channels by selecting a low intensity region shown by a red circle in Figure A.1 (a), a non-localized channel is obtained. Not being associated with any local resonating nanoantenna, as can be seen in Figure A.1 (b), the field expands over larger area. This indicates that adding non-localized transmission channels to the existing localized channels is limited by the area of nanostructure and suggests there are fewer number of this type of channels that can be added before the output channels are no longer isolated. Making the area of structure larger, while keeping the filling factor fixed, larger number of channels can be realized.

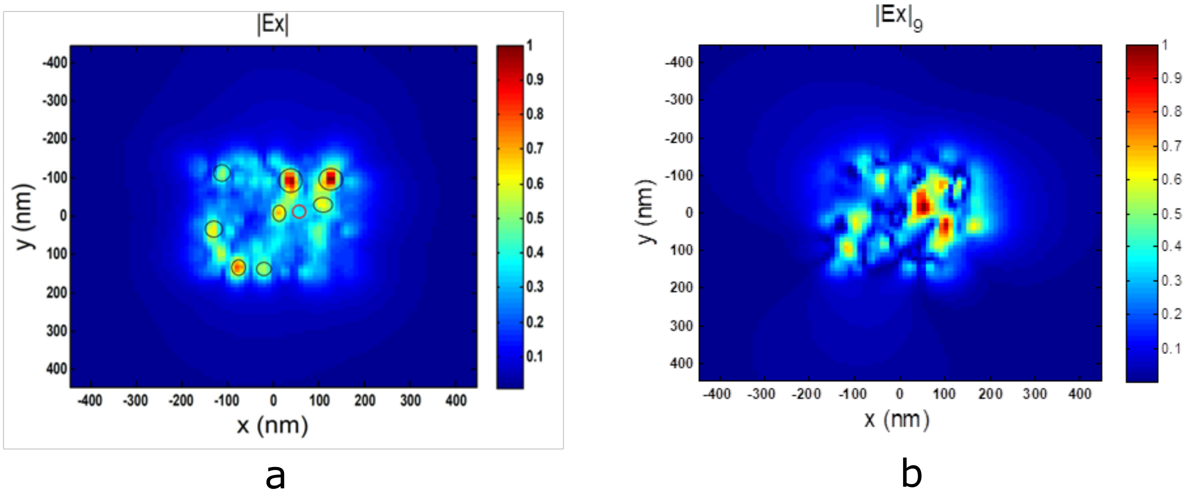

Figure A.1: (a) shows the candidate channels over the output plane. The red circle corresponds to a non-localized channel. (b) is the electric field distribution corresponding to the chosen non-localized channel.

Appendix B

Near Optimal Freeform Inverse Design (NOFID)

The flowchart shown in Fig. B.1 summarizes the devised algorithm used to design disordered structures composed of coupled subwavelength scattering elements. It consists of a few main steps:

1. **Initialization**
    (a) An initial configuration for scattering elements is chosen. The initial configuration features the best value for the cost function among hundreds of random configurations with the same number of scatterers.
    (b) The threshold is initialized. The value should be larger than the expected (average) value that the cost function will be increased due to adding one new scattering element to the existing structure which consists of n_d elements.
    (c) The controlling parameters, M_t and N_t, are set to one. M_{tmax} determines the maximum number of tries to find the best location for adding one new scattering element. N_{tmax} determines the maximum number of iterations before the threshold is updated. Each iteration consists of M_{tmax} tries to add one element to the existing configuration. In addition, N_{tmax} represents the maximum number of scattering elements which can be added all satisfying the condition of increasing the cost function at least by the threshold, which is constant during the N_{tmax} iterations.

   (d) New sets are defined for the temporary locations which are candidates for the location of one new scattering element, and the corresponding enhancements in the cost function, as $\{(x, y)_t\}$ and $\{C_t\}$, respectively

2. **Random Location**

   One random location for adding one temporary new dielectric inclusion is chosen within the structure. The location and resultant cost function in the new configuration are denoted by (x_r, y_r), and C_r, respectively.

3. **Temporary Selection Criterion**

   If the new cost function is larger than the previous one at least by the current value of the threshold, (x_r, y_r) and C_r will be added to $\{(x, y)_t\}$ and $\{C_t\}$, respectively. M_t is increased by one and the algorithm starts from step 2, unless M_t is equal to M_{tmax}.

4. **Final Selection**

   After steps 2 and 3 are repeated for M_{tmax} times, the initial (current) configuration is updated by adding one new scattering element (if any) at the best location in $\{(x, y)_t\}$, which is associated with the maximum value in $\{C_t\}$. The two sets, $\{(x, y)_t\}$ and $\{C_t\}$, are reset and M_t is set to one. N_t is increased by one and the algorithm starts from step 2, unless N_t is equal to N_{tmax}.

5. **Updating Threshold**

   The threshold is updated after N_{tmax} repetitions of steps 2 and 3, where a maximum number of N_{tmax} scattering elements could be added to the initial configuration. However, depending on the configuration or the value of threshold, the number of scattering elements that have been added to the initial configuration varies. Two cases are, first, at least one element has been added and, second, no location has been selected in previous steps to add one new element. Depending on the case, the threshold is updated as follows

$$\begin{aligned} Threshold_{new} &= \gamma \times sign(|\gamma| - Crossover\,value), \\ \gamma &= (n - 1 + \alpha^{\beta}) \times Threshold_{old}, \\ \alpha = (1/n + 1 - n), \beta &= \frac{1 \pm sign(Threshold_{old})}{2}, \\ (+(-) : No\,(at\,least\,one)\,&scattering\,element\,added). \end{aligned} \tag{B.1}$$

   n is a coefficient which is used to update the threshold by multiplying the current threshold by $1/n$ or n which depends on the situation (two cases outlined before).

The numerical value of this parameter affects how the configuration of dielectric inclusions is updated and how long it will take the algorithm to reach to the final configuration. Larger value may accelerate the process of optimization, however, the efficiency of algorithm in finding the best configuration might be negatively affected. This is due to the fact that the value of threshold becomes negative before sufficient number of iterations has been tried to find better locations for adding new dielectric inclusions maximizing the transmittance by larger values. On the other hand, smaller coefficients lead to longer process, because of the longer time it takes the algorithm to update the threshold to lower values to let one new scattering element be added to the configuration. This happens in a situation where the configuration represents a local maximum (minimum) in the solution space. In this work we assume a constant value for n. The *Crossover value* is chosen to be a very small number (close to zero). As the threshold becomes smaller than this value, its sign will change. This avoids getting stuck on local maximum (minimum) and allows the algorithm to search for global maximum (minimum) in the solution space. This is done through accepting new dielectric inclusions into the locally optimum configuration making the cost function slightly lower (or higher for minimizing cost function) temporarily. However, according to Eq. B.1, threshold will be updated, afterwards, in such a way that the algorithm looks for locations to add new scattering elements in the new configuration which ultimately leads to a maximum enhancement of the cost function larger than what has been obtained so far.

6. **Stopping Criterion**

   The previous steps will be repeated until a desired value for the cost function is obtained or the user stops the process for any other reason such as reaching to the preset number of scattering elements.

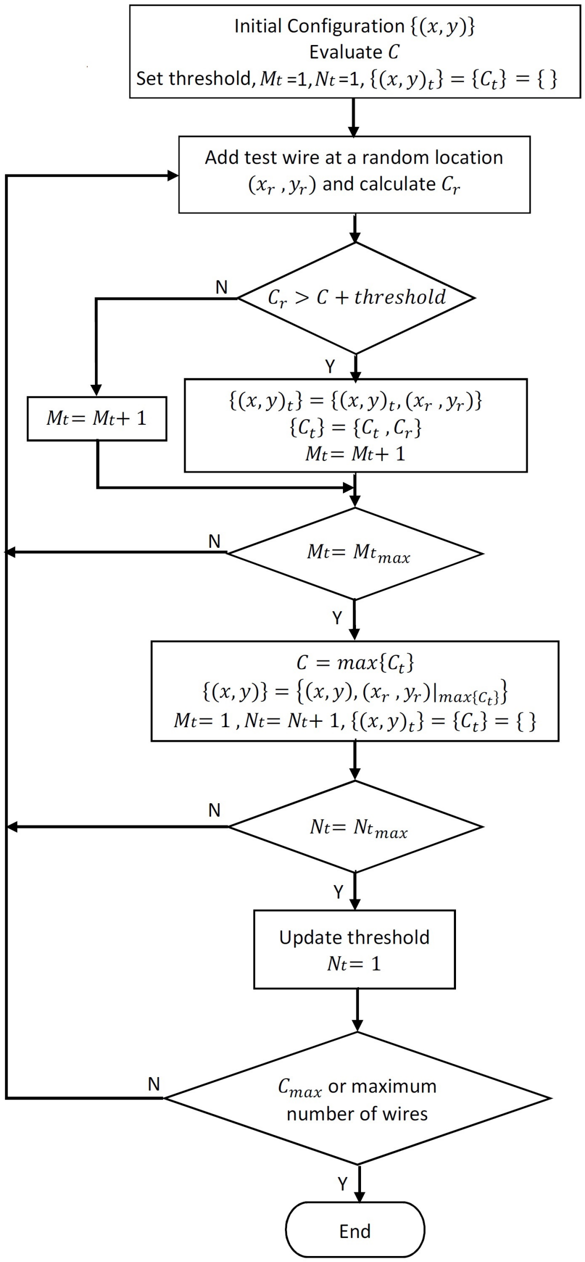

Figure B.1: The flowchart of the proposed algorithm used for engineering the scattering features of a “disorder engineered” medium.

Appendix C

Near field measurements of silver nanowires (AgNWs)

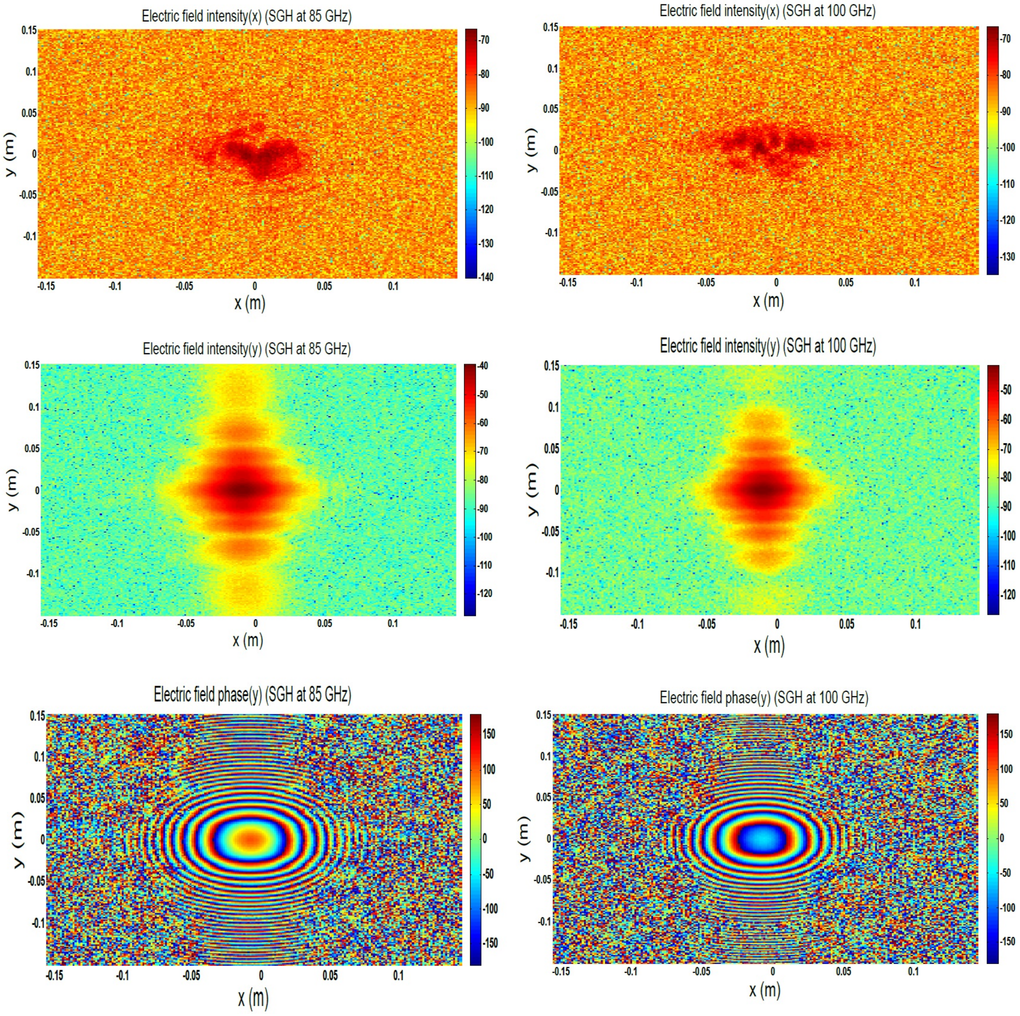

Figure C.1: The measured signals representing the radiated electric field tangential components (x and y) by the SGH in 85 GHz and 100 GHz.

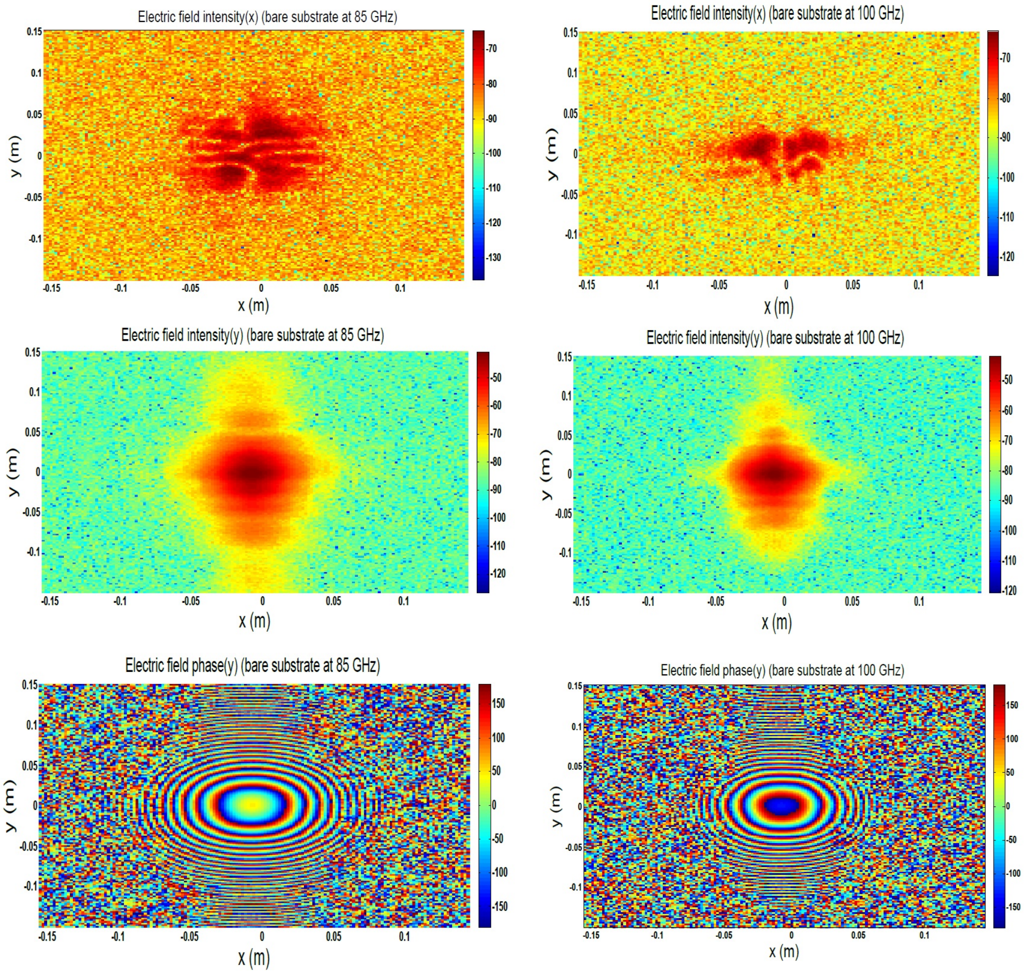

Figure C.2: The measured signals representing radiated electric field tangential components (x and y) by the SGH in the presence of bare plastic substrate over the scan window in 85 GHz and 100 GHz.

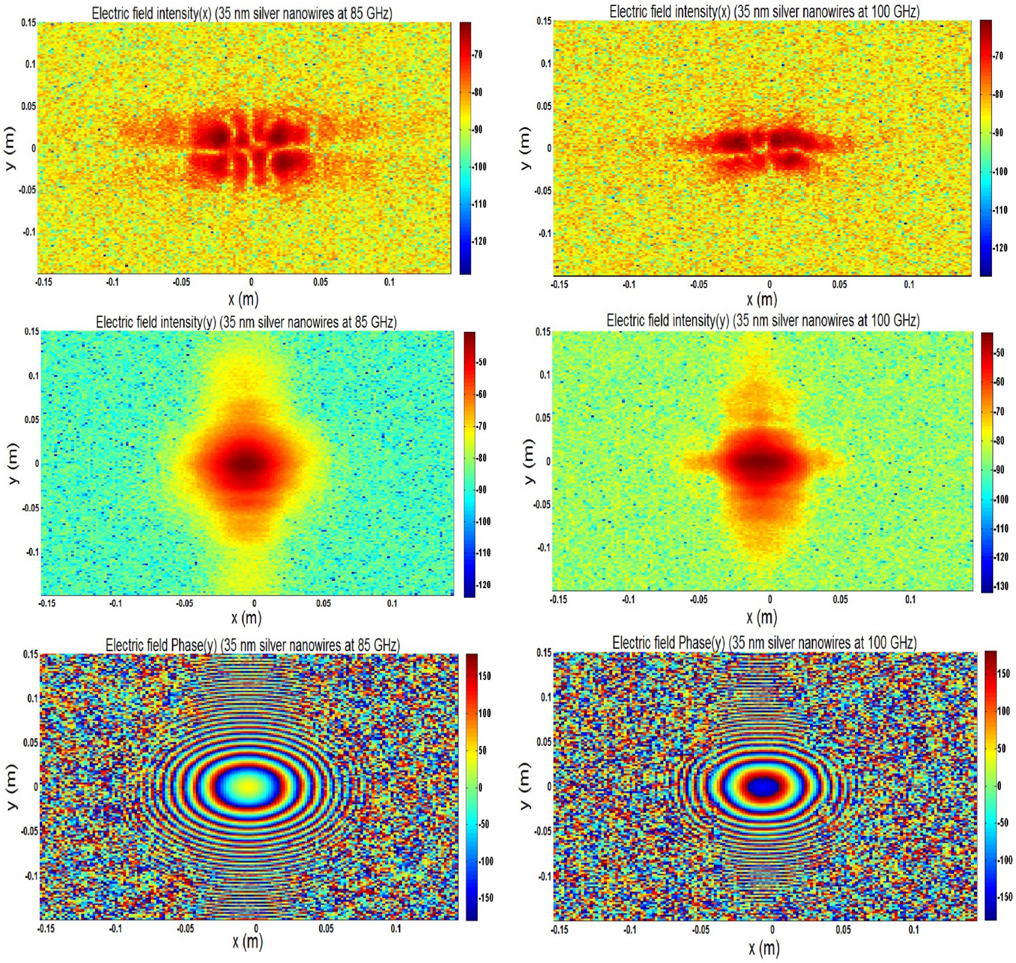

Figure C.3: The measured signals representing radiated electric field tangential components (x and y) by the SGH in the presence of the plastic substrate coated with silver nanowires with diameter of 35 nm and average length of 15 μm over the scan window in 85 GHz and 100 GHz.

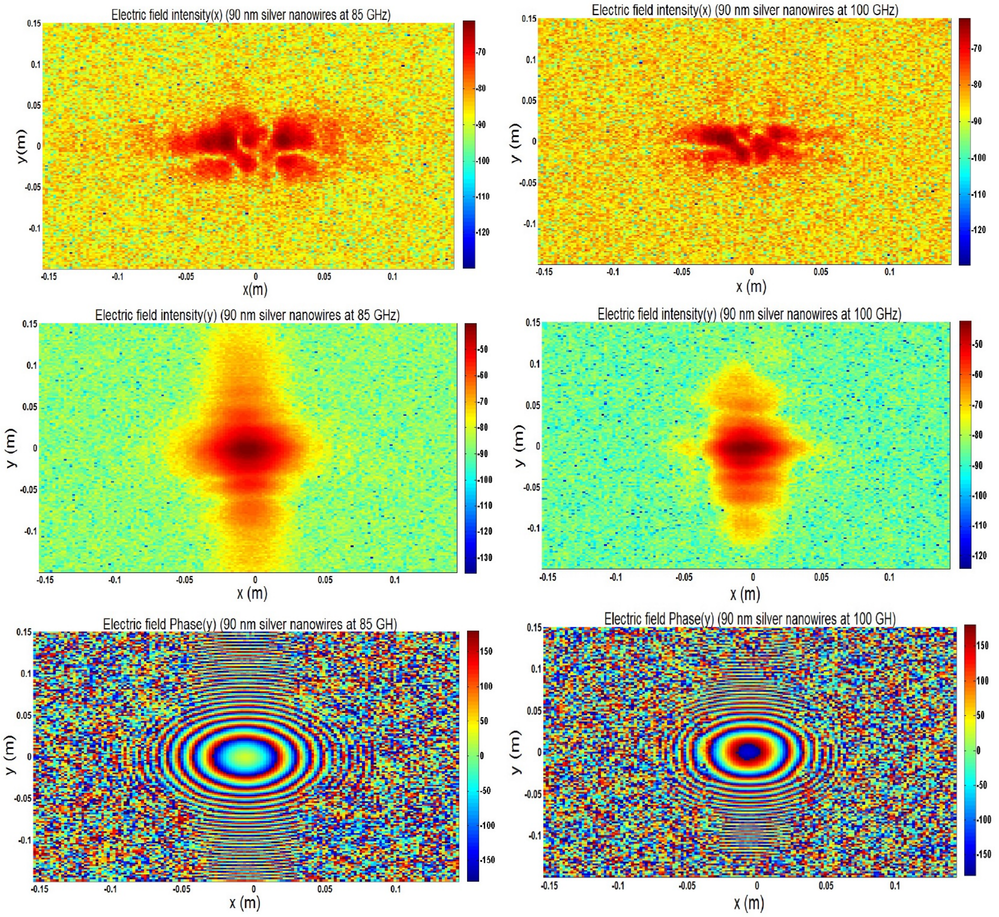

Figure C.4: The measured signals representing radiated electric field tangential components (x and y) by the SGH in the presence of the plastic substrate coated with silver nanowires with diameter of 90 nm and average length of 15-20 μm over the scan window in 85 GHz and 100 GHz.

References

[1] A. Corana, M. Marchesi, C. Martini, and S. Ridella, "Minimizing multimodal functions of continuous variables with the simulated annealing algorithm corrigenda for this article is available here," *ACM Transactions on Mathematical Software (TOMS)*, vol. 13, no. 3, pp. 262–280, 1987.

[2] G. Casati, L. Molinari, and F. Izrailev, "Scaling properties of band random matrices," *Physical review letters*, vol. 64, no. 16, p. 1851, 1990.

[3] P. A. Martin, *Multiple scattering: interaction of time-harmonic waves with N obstacles.* Cambridge University Press, 2006, no. 107.

[4] "Disordered times," *Nature Photonics*, vol. 7, no. 161, 2013.

[5] P. W. Anderson, "Absence of diffusion in certain random lattices," *Physical review*, vol. 109, no. 5, p. 1492, 1958.

[6] A. Lagendijk, B. van Tiggelen, and D. S. Wiersma, "Fifty years of anderson localization," *Phys. Today*, vol. 62, no. 8, pp. 24–29, 2009.

[7] D. S. Wiersma, "The physics and applications of random lasers," *Nature physics*, vol. 4, no. 5, pp. 359–367, 2008.

[8] M. Gaio, M. Peruzzo, and R. Sapienza, "Tuning random lasing in photonic glasses," *Optics letters*, vol. 40, no. 7, pp. 1611–1614, 2015.

[9] W. Z. W. Ismail, E. M. Goldys, and J. M. Dawes, "Extended emission wavelength of random dye lasers by exploiting radiative and non-radiative energy transfer," *Applied Physics B*, vol. 122, no. 2, pp. 1–9, 2016.

[10] A. G. Ardakani and P. Rafieipour, "Investigation of one-dimensional raman random lasers based on the finite-difference-time-domain method: Presence of mode competition and higher-order stokes and anti-stokes modes," *Physical Review A*, vol. 93, no. 2, p. 023833, 2016.

[11] Q. Baudouin, N. Mercadier, V. Guarrera, W. Guerin, and R. Kaiser, "A cold-atom random laser," *Nature physics*, vol. 9, no. 6, pp. 357–360, 2013.

[12] J. Topolancik, B. Ilic, and F. Vollmer, "Experimental observation of strong photon localization in disordered photonic crystal waveguides," *Physical review letters*, vol. 99, no. 25, p. 253901, 2007.

[13] R. Dalichaouch, J. Armstrong, S. Schultz, P. Platzman, and S. McCall, "Microwave localization by two-dimensional random scattering," 1991.

[14] M. Segev, Y. Silberberg, and D. N. Christodoulides, "Anderson localization of light," *Nature Photonics*, vol. 7, no. 3, pp. 197–204, 2013.

[15] M. D. Kelzenberg, S. W. Boettcher, J. A. Petykiewicz, D. B. Turner-Evans, M. C. Putnam, E. L. Warren, J. M. Spurgeon, R. M. Briggs, N. S. Lewis, and H. A. Atwater, "Enhanced absorption and carrier collection in si wire arrays for photovoltaic applications," *Nature materials*, vol. 9, no. 3, pp. 239–244, 2010.

[16] T. Strudley, T. Zehender, C. Blejean, E. P. Bakkers, and O. L. Muskens, "Mesoscopic light transport by very strong collective multiple scattering in nanowire mats," *Nature Photonics*, vol. 7, no. 5, pp. 413–418, 2013.

[17] S. Skipetrov, "Information transfer through disordered media by diffuse waves," *Physical Review E*, vol. 67, no. 3, p. 036621, 2003.

[18] C. E. Shannon, "Bell system tech," *Bell System Tech. J*, vol. 27, p. 623, 1948.

[19] S. H. Simon, A. L. Moustakas, M. Stoytchev, and H. Safar, "Communication in a disordered world," *Physics Today*, vol. 54, no. 9, pp. 38–43, 2001.

[20] E. N. Lorenz, "Deterministic nonperiodic flow," *Journal of the atmospheric sciences*, vol. 20, no. 2, pp. 130–141, 1963.

[21] R. Matthews, "On the derivation of a chaotic encryption algorithm," *Cryptologia*, vol. 13, no. 1, pp. 29–42, 1989.

[22] C. W. Wu and L. O. Chua, “A simple way to synchronize chaotic systems with applications to secure communication systems,” *International Journal of Bifurcation and Chaos*, vol. 3, no. 06, pp. 1619–1627, 1993.

[23] C. Gmachl, F. Capasso, E. Narimanov, J. U. Nöckel, A. D. Stone, J. Faist, D. L. Sivco, and A. Y. Cho, “High-power directional emission from microlasers with chaotic resonators,” *Science*, vol. 280, no. 5369, pp. 1556–1564, 1998.

[24] K. Aihara, “Chaos engineering and its application to parallel distributed processing with chaotic neural networks,” *Proceedings of the IEEE*, vol. 90, no. 5, pp. 919–930, 2002.

[25] A. Sundaramurthy, P. J. Schuck, N. R. Conley, D. P. Fromm, G. S. Kino, and W. Moerner, “Toward nanometer-scale optical photolithography: utilizing the near-field of bowtie optical nanoantennas,” *Nano letters*, vol. 6, no. 3, pp. 355–360, 2006.

[26] M. F. Garcia-Parajo, “Optical antennas focus in on biology,” *Nature Photonics*, vol. 2, no. 4, pp. 201–203, 2008.

[27] P.-Y. Chen and A. Alù, “Optical nanoantenna arrays loaded with nonlinear materials,” *Physical Review B*, vol. 82, no. 23, p. 235405, 2010.

[28] T. H. Taminiau, F. D. Stefani, and N. F. van Hulst, “Enhanced directional excitation and emission of single emitters by a nano-optical yagi-uda antenna,” *Optics express*, vol. 16, no. 14, pp. 10 858–10 866, 2008.

[29] L. Shao, X. Zhuo, and J. Wang, “Advanced plasmonic materials for dynamic color display,” *Advanced Materials*, vol. 30, no. 16, p. 1704338, 2018.

[30] D. Rodrigo, A. Tittl, N. Ait-Bouziad, A. John-Herpin, O. Limaj, C. Kelly, D. Yoo, N. J. Wittenberg, S.-H. Oh, H. A. Lashuel *et al.*, “Resolving molecule-specific information in dynamic lipid membrane processes with multi-resonant infrared metasurfaces,” *Nature communications*, vol. 9, no. 1, p. 2160, 2018.

[31] H. Abediasl and H. Hashemi, “Monolithic optical phased-array transceiver in a standard soi cmos process,” *Optics express*, vol. 23, no. 5, pp. 6509–6519, 2015.

[32] J. Sun, E. Timurdogan, A. Yaacobi, E. S. Hosseini, and M. R. Watts, “Large-scale nanophotonic phased array,” *Nature*, vol. 493, no. 7431, p. 195, 2013.

[33] I. M. Vellekoop and A. Mosk, “Focusing coherent light through opaque strongly scattering media,” *Optics letters*, vol. 32, no. 16, pp. 2309–2311, 2007.

[34] I. Vellekoop, A. Lagendijk, and A. Mosk, “Exploiting disorder for perfect focusing,” *Nature photonics*, vol. 4, no. 5, pp. 320–322, 2010.

[35] M. Khorasaninejad, W. T. Chen, R. C. Devlin, J. Oh, A. Y. Zhu, and F. Capasso, “Metalenses at visible wavelengths: Diffraction-limited focusing and subwavelength resolution imaging,” *Science*, vol. 352, no. 6290, pp. 1190–1194, 2016.

[36] R. C. Devlin, A. Ambrosio, N. A. Rubin, J. B. Mueller, and F. Capasso, “Arbitrary spin-to–orbital angular momentum conversion of light,” *Science*, vol. 358, no. 6365, pp. 896–901, 2017.

[37] Z. Shi, M. Khorasaninejad, Y.-W. Huang, C. Roques-Carmes, A. Y. Zhu, W. T. Chen, V. Sanjeev, Z.-W. Ding, M. Tamagnone, K. Chaudhary *et al.*, “Single-layer metasurface with controllable multiwavelength functions,” *Nano letters*, vol. 18, no. 4, pp. 2420–2427, 2018.

[38] Z. Lin, B. Groever, F. Capasso, A. W. Rodriguez, and M. Lončar, “Topology-optimized multilayered metaoptics,” *Physical Review Applied*, vol. 9, no. 4, p. 044030, 2018.

[39] L. Waller and L. Tian, “Computational imaging: machine learning for 3d microscopy,” *Nature*, vol. 523, no. 7561, p. 416, 2015.

[40] X. Lin, Y. Rivenson, N. T. Yardimci, M. Veli, Y. Luo, M. Jarrahi, and A. Ozcan, “All-optical machine learning using diffractive deep neural networks,” *Science*, vol. 361, no. 6406, pp. 1004–1008, 2018.

[41] O. Katz, P. Heidmann, M. Fink, and S. Gigan, “Non-invasive single-shot imaging through scattering layers and around corners via speckle correlations,” *Nature photonics*, vol. 8, no. 10, p. 784, 2014.

[42] G. Lerosey, J. De Rosny, A. Tourin, and M. Fink, “Focusing beyond the diffraction limit with far-field time reversal,” *Science*, vol. 315, no. 5815, pp. 1120–1122, 2007.

[43] J. B. Pendry, D. Schurig, and D. R. Smith, “Controlling electromagnetic fields,” *science*, vol. 312, no. 5781, pp. 1780–1782, 2006.

[44] U. Leonhardt, “Optical conformal mapping,” *Science*, vol. 312, no. 5781, pp. 1777–1780, 2006.

[45] D. Schurig, J. Mock, B. Justice, S. A. Cummer, J. B. Pendry, A. Starr, and D. Smith, "Metamaterial electromagnetic cloak at microwave frequencies," *Science*, vol. 314, no. 5801, pp. 977–980, 2006.

[46] L. H. Gabrielli, J. Cardenas, C. B. Poitras, and M. Lipson, "Silicon nanostructure cloak operating at optical frequencies," *Nature Photonics*, vol. 3, no. 8, pp. 461–463, 2009.

[47] P.-Y. Chen, J. Soric, and A. Alù, "Invisibility and cloaking based on scattering cancellation," *Advanced Materials*, vol. 24, no. 44, pp. OP281–OP304, 2012.

[48] S. Longhi, "Bidirectional invisibility in kramers–kronig optical media," *Optics letters*, vol. 41, no. 16, pp. 3727–3730, 2016.

[49] Z. Hayran, H. Kurt, R. Herrero, M. Botey, K. Staliunas, and K. Staliunas, "All-dielectric self-cloaked structures," *ACS Photonics*, vol. 5, no. 5, pp. 2068–2073, 2018.

[50] D. Ye, L. Lu, J. D. Joannopoulos, M. Soljačić, and L. Ran, "Invisible metallic mesh," *Proceedings of the National Academy of Sciences*, vol. 113, no. 10, pp. 2568–2572, 2016.

[51] S. Schönhuber, M. Brandstetter, T. Hisch, C. Deutsch, M. Krall, H. Detz, A. M. Andrews, G. Strasser, S. Rotter, and K. Unterrainer, "Random lasers for broadband directional emission," *Optica*, vol. 3, no. 10, pp. 1035–1038, 2016.

[52] D. Dregely, R. Taubert, J. Dorfmüller, R. Vogelgesang, K. Kern, and H. Giessen, "3d optical yagi-uda nanoantenna array," *Nature communications*, vol. 2, p. 267, 2011.

[53] X. Ni, N. K. Emani, A. V. Kildishev, A. Boltasseva, and V. M. Shalaev, "Broadband light bending with plasmonic nanoantennas," *Science*, vol. 335, no. 6067, pp. 427–427, 2012.

[54] D. S. Wiersma, "Disordered photonics," *Nature Photonics*, vol. 7, no. 3, pp. 188–196, 2013.

[55] R. H. Siddique, G. Gomard, and H. Hölscher, "The role of random nanostructures for the omnidirectional anti-reflection properties of the glasswing butterfly," *Nature communications*, vol. 6, 2015.

[56] M. Kim, Y. Choi, C. Yoon, W. Choi, J. Kim, Q.-H. Park, and W. Choi, "Maximal energy transport through disordered media with the implementation of transmission eigenchannels," *Nature photonics*, vol. 6, no. 9, pp. 581–585, 2012.

[57] A. Alu and N. Engheta, “Input impedance, nanocircuit loading, and radiation tuning of optical nanoantennas,” *Physical review letters*, vol. 101, no. 4, p. 043901, 2008.

[58] Y. Zhao, N. Engheta, and A. Alù, “Effects of shape and loading of optical nanoantennas on their sensitivity and radiation properties,” *JOSA B*, vol. 28, no. 5, pp. 1266–1274, 2011.

[59] L. Novotny, “Effective wavelength scaling for optical antennas,” *Physical Review Letters*, vol. 98, no. 26, p. 266802, 2007.

[60] T. Feichtner, O. Selig, M. Kiunke, and B. Hecht, “Evolutionary optimization of optical antennas,” *Physical review letters*, vol. 109, no. 12, p. 127701, 2012.

[61] J. Borneman, K.-P. Chen, A. Kildishev, and V. Shalaev, “Simplified model for periodic nanoantennae: linear model and inverse design,” *Optics express*, vol. 17, no. 14, pp. 11 607–11 617, 2009.

[62] A. Taflove and S. C. Hagness, *Computational electrodynamics: the finite-difference time-domain method.* Artech house publishers, 2000.

[63] J. Hoffmann, C. Hafner, P. Leidenberger, J. Hesselbarth, and S. Burger, “Comparison of electromagnetic field solvers for the 3d analysis of plasmonic nanoantennas,” in *SPIE Europe Optical Metrology.* International Society for Optics and Photonics, 2009, pp. 73 900J–73 900J.

[64] H. Fischer and O. J. Martin, “Engineering the optical response of plasmonic nanoantennas,” *Optics express*, vol. 16, no. 12, pp. 9144–9154, 2008.

[65] Y. L. Chow, J. Yang, D. Fang, and G. Howard, “A closed-form spatial green’s function for the thick microstrip substrate,” *Microwave Theory and Techniques, IEEE Transactions on*, vol. 39, no. 3, pp. 588–592, 1991.

[66] W. C. Chew, *Waves and fields in inhomogeneous media.* IEEE press New York, 1995, vol. 522.

[67] J. M. Johnson and Y. Rahmat-Samii, “Genetic algorithms and method of moments (ga/mom) for the design of integrated antennas,” *Antennas and Propagation, IEEE Transactions on*, vol. 47, no. 10, pp. 1606–1614, 1999.

[68] H. Alaeian and R. Faraji-Dana, “A fast and accurate analysis of 2-d periodic devices using complex images green’s functions,” *Journal of Lightwave Technology*, vol. 27, no. 13, pp. 2216–2223, 2009.

[69] M. Haghtalab and R. Faraji-Dana, “Integral equation analysis and optimization of 2d layered nanolithography masks by complex images greens function technique in tm polarization,” *JOSA A*, vol. 29, no. 5, pp. 748–756, 2012.

[70] H. G. P.-o.-F. Mrsrnon, “Generalized pencil-of-function method for extracting poles of an em system from its transient response,” *IEEE Transactions on Antennas and Propagation*, vol. 37, no. 2, 1989.

[71] R. F. Harrington and J. L. Harrington, *Field computation by moment methods.* Oxford University Press, 1996.

[72] L. Wu, H. Chu, W. Koh, and E. Li, “Highly sensitive graphene biosensors based on surface plasmon resonance,” *Optics express*, vol. 18, no. 14, pp. 14 395–14 400, 2010.

[73] A. Kumar, K. Hsu, K. Jacobs, P. Ferreira, and N. Fang, “Direct metal nanoimprinting using an embossed solid electrolyte stamp,” *Nanotechnology*, vol. 22, no. 15, p. 155302, 2011.

[74] J. K. Yang and K. K. Berggren, “Using high-contrast salty development of hydrogen silsesquioxane for sub-10-nm half-pitch lithography,” *Journal of Vacuum Science & Technology B*, vol. 25, no. 6, pp. 2025–2029, 2007.

[75] Z. Liu, H. Lee, Y. Xiong, C. Sun, and X. Zhang, “Far-field optical hyperlens magnifying sub-diffraction-limited objects,” *science*, vol. 315, no. 5819, pp. 1686–1686, 2007.

[76] N. Fang, H. Lee, C. Sun, and X. Zhang, “Sub–diffraction-limited optical imaging with a silver superlens,” *Science*, vol. 308, no. 5721, pp. 534–537, 2005.

[77] S. W. Hell, “Far-field optical nanoscopy,” *science*, vol. 316, no. 5828, pp. 1153–1158, 2007.

[78] B. Huang, W. Wang, M. Bates, and X. Zhuang, “Three-dimensional super-resolution imaging by stochastic optical reconstruction microscopy,” *Science*, vol. 319, no. 5864, pp. 810–813, 2008.

[79] L. Tian, X. Li, K. Ramchandran, and L. Waller, “Multiplexed coded illumination for fourier ptychography with an led array microscope,” *Biomedical optics express*, vol. 5, no. 7, pp. 2376–2389, 2014.

[80] B. Khademhosseinieh, I. Sencan, G. Biener, T.-W. Su, A. F. Coskun, D. Tseng, and A. Ozcan, "Lensfree on-chip imaging using nanostructured surfaces," *Applied physics letters*, vol. 96, no. 17, p. 171106, 2010.

[81] S. A. Alexandrov, S. Uttam, R. K. Bista, K. Staton, and Y. Liu, "Spectral encoding of spatial frequency approach for characterization of nanoscale structures," *Applied physics letters*, vol. 101, no. 3, p. 033702, 2012.

[82] L. Cherkezyan, I. Capoglu, H. Subramanian, J. Rogers, D. Damania, A. Taflove, and V. Backman, "Interferometric spectroscopy of scattered light can quantify the statistics of subdiffractional refractive-index fluctuations," *Physical review letters*, vol. 111, no. 3, p. 033903, 2013.

[83] H. Subramanian, P. Pradhan, Y. Liu, I. R. Capoglu, J. D. Rogers, H. K. Roy, R. E. Brand, and V. Backman, "Partial-wave microscopic spectroscopy detects subwavelength refractive index fluctuations: an application to cancer diagnosis," *Optics letters*, vol. 34, no. 4, pp. 518–520, 2009.

[84] A. Porat, E. R. Andresen, H. Rigneault, D. Oron, S. Gigan, and O. Katz, "Widefield lensless imaging through a fiber bundle via speckle correlations," *Optics express*, vol. 24, no. 15, pp. 16 835–16 855, 2016.

[85] J. Bertolotti, E. G. van Putten, C. Blum, A. Lagendijk, W. L. Vos, and A. P. Mosk, "Non-invasive imaging through opaque scattering layers," *Nature*, vol. 491, no. 7423, p. 232, 2012.

[86] J. R. Fienup, "Phase retrieval algorithms: a comparison," *Applied optics*, vol. 21, no. 15, pp. 2758–2769, 1982.

[87] H. Stark, *Image recovery: theory and application.* Elsevier, 1987.

[88] A. Liutkus, D. Martina, S. Popoff, G. Chardon, O. Katz, G. Lerosey, S. Gigan, L. Daudet, and I. Carron, "Imaging with nature: Compressive imaging using a multiply scattering medium," *Scientific reports*, vol. 4, p. 5552, 2014.

[89] L. Li, F. Li, and T. J. Cui, "Feasibility of resonant metalens for the subwavelength imaging using a single sensor in the far field," *Optics Express*, vol. 22, no. 15, pp. 18 688–18 697, 2014.

[90] L. Li, F. Li, T. J. Cui, and K. Yao, "Far-field imaging beyond diffraction limit using single sensor in combination with a resonant aperture," *Optics Express*, vol. 23, no. 1, pp. 401–412, 2015.

[91] L. Li, "Subwavelength imaging of sparse broadband sources in an open disordered medium from a single antenna," *IEEE Antennas and Wireless Propagation Letters*, vol. 13, pp. 1461–1464, 2014.

[92] Z. Yaqoob, D. Psaltis, M. S. Feld, and C. Yang, "Optical phase conjugation for turbidity suppression in biological samples," *Nature photonics*, vol. 2, no. 2, p. 110, 2008.

[93] W. L. Vos, T. W. Tukker, A. P. Mosk, A. Lagendijk, and W. L. IJzerman, "Broadband mean free path of diffuse light in polydisperse ensembles of scatterers for white light-emitting diode lighting," *Applied optics*, vol. 52, no. 12, pp. 2602–2609, 2013.

[94] M. Haghtalab, R. Faraji-Dana, and S. Safavi-Naeini, "Design and analysis of disordered optical nanoantenna structures," *Journal of Lightwave Technology*, vol. 34, no. 11, pp. 2838–2847, 2016.

[95] A. Boniface, M. Mounaix, B. Blochet, R. Piestun, and S. Gigan, "Transmission-matrix-based point-spread-function engineering through a complex medium," *Optica*, vol. 4, no. 1, pp. 54–59, 2017.

[96] A. Ozcan and E. McLeod, "Lensless imaging and sensing," *Annual review of biomedical engineering*, vol. 18, pp. 77–102, 2016.

[97] S. F. Liew, S. M. Popoff, A. P. Mosk, W. L. Vos, and H. Cao, "Transmission channels for light in absorbing random media: from diffusive to ballistic-like transport," *Physical Review B*, vol. 89, no. 22, p. 224202, 2014.

[98] L. Tsang and J. A. Kong, *Scattering of electromagnetic waves: advanced topics*. John Wiley & Sons, 2004, vol. 26.

[99] R. F. Harrington, *Time-harmonic electromagnetic fields*. McGraw-Hill, 1961.

[100] M. Bendsoe, "Sigmund, topology optimization-theory, methods and applications," 2003.

[101] J. A. Lewis, "Novel inks for direct-write assembly of 3-d periodic structures," *Mater. Matters*, vol. 3, no. 1, pp. 4–7, 2008.

[102] M. Lis, M. Plaut, A. Zai, D. Cipolle, J. Russo, J. Lewis, and T. Fedynyshyn, "Polymer dielectrics for 3d-printed rf devices in the ka band," *Advanced Materials Technologies*, vol. 1, no. 2, p. 1600027, 2016.

[103] S. Peng, R. Zhang, V. H. Chen, E. T. Khabiboulline, P. Braun, and H. A. Atwater, "Three-dimensional single gyroid photonic crystals with a mid-infrared bandgap," *ACS Photonics*, vol. 3, no. 6, pp. 1131–1137, 2016.

[104] S. Shahir, M. Mohajer, A. Rohani, and S. Safavi-Naeini, "Permittivity profile estimation based on non-radiating equivalent source (2d case)," *Progress In Electromagnetics Research*, vol. 50, pp. 157–175, 2013.

[105] S. Pang, Y. Hernandez, X. Feng, and K. Müllen, "Graphene as transparent electrode material for organic electronics," *Advanced Materials*, vol. 23, no. 25, pp. 2779–2795, 2011.

[106] J. Woerle and H. Rost, "Roll-to-roll production of transparent conductive films using metallic grids," *MRS bulletin*, vol. 36, no. 10, pp. 789–793, 2011.

[107] P. B. Catrysse and S. Fan, "Nanopatterned metallic films for use as transparent conductive electrodes in optoelectronic devices," *Nano letters*, vol. 10, no. 8, pp. 2944–2949, 2010.

[108] D. S. Hecht, A. M. Heintz, R. Lee, L. Hu, B. Moore, C. Cucksey, and S. Risser, "High conductivity transparent carbon nanotube films deposited from superacid," *Nanotechnology*, vol. 22, no. 7, p. 075201, 2011.

[109] D. Alemu, H.-Y. Wei, K.-C. Ho, and C.-W. Chu, "Highly conductive pedot: Pss electrode by simple film treatment with methanol for ito-free polymer solar cells," *Energy & environmental science*, vol. 5, no. 11, pp. 9662–9671, 2012.

[110] J. van de Groep, P. Spinelli, and A. Polman, "Transparent conducting silver nanowire networks," *Nano letters*, vol. 12, no. 6, pp. 3138–3144, 2012.

[111] L. Hu, H. S. Kim, J.-Y. Lee, P. Peumans, and Y. Cui, "Scalable coating and properties of transparent, flexible, silver nanowire electrodes," *ACS nano*, vol. 4, no. 5, pp. 2955–2963, 2010.

[112] H. H. Khaligh, K. Liew, Y. Han, N. M. Abukhdeir, and I. A. Goldthorpe, "Silver nanowire transparent electrodes for liquid crystal-based smart windows," *Solar Energy Materials and Solar Cells*, vol. 132, pp. 337–341, 2015.

[113] L. Song, A. C. Myers, J. J. Adams, and Y. Zhu, "Stretchable and reversibly deformable radio frequency antennas based on silver nanowires," *ACS applied materials & interfaces*, vol. 6, no. 6, pp. 4248–4253, 2014.

[114] B. Oner, M. Can, and H. Kurt, "Dual polarized broadband and all dielectric partial cloaking using stacked graded index structures," *Optics express*, vol. 22, no. 17, pp. 20 457–20 462, 2014.

[115] B. Oner, M. Turduev, and H. Kurt, "High-efficiency beam bending using graded photonic crystals," *Optics letters*, vol. 38, no. 10, pp. 1688–1690, 2013.

[116] M. F. Schumann, S. Wiesendanger, J. C. Goldschmidt, B. Bläsi, K. Bittkau, U. W. Paetzold, A. Sprafke, R. B. Wehrspohn, C. Rockstuhl, and M. Wegener, "Cloaked contact grids on solar cells by coordinate transformations: designs and prototypes," *Optica*, vol. 2, no. 10, pp. 850–853, 2015.

[117] N. A. Mortensen, O. Sigmund, and O. Breinbjerg, "Prospects for poor-man's cloaking with low-contrast all-dielectric optical elements," *Journal of the European Optical Society-Rapid publications*, vol. 4, 2009.

[118] Z. Ruan, M. Yan, C. W. Neff, and M. Qiu, "Ideal cylindrical cloak: perfect but sensitive to tiny perturbations," *Physical Review Letters*, vol. 99, no. 11, p. 113903, 2007.

[119] M. Yan, Z. Ruan, and M. Qiu, "Cylindrical invisibility cloak with simplified material parameters is inherently visible," *Physical Review Letters*, vol. 99, no. 23, p. 233901, 2007.

[120] R. Fleury and A. Alù, "Cloaking and invisibility: A review," in *Forum for Electromagnetic Research Methods and Application Technologies (FERMAT)*, vol. 1, no. EPFL-ARTICLE-223081, 2014.

[121] Hosseinzadeh khaligh, Hadi, "Silver nanowire transparent electrodes for device applications," Ph.D. dissertation, 2016. [Online]. Available: http://hdl.handle.net/10012/10973

[122] M. Marus, A. Hubarevich, R. J. W. Lim, H. Huang, A. Smirnov, H. Wang, W. Fan, and X. W. Sun, "Effect of silver nanowire length in a broad range on optical and electrical properties as a transparent conductive film," *Optical Materials Express*, vol. 7, no. 3, pp. 1105–1112, 2017.

[123] B. Sensale-Rodriguez, R. Yan, M. M. Kelly, T. Fang, K. Tahy, W. S. Hwang, D. Jena, L. Liu, and H. G. Xing, "Broadband graphene terahertz modulators enabled by intraband transitions," *Nature communications*, vol. 3, p. 780, 2012.

[124] D. S. Wiersma, "Optical physics: Clear directions for random lasers," *Nature*, vol. 539, no. 7629, p. 360, 2016.

[125] K. S. Novoselov, A. K. Geim, S. Morozov, D. Jiang, Y. Zhang, S. Dubonos, , I. Grigorieva, and A. Firsov, "Electric field effect in atomically thin carbon films," *science*, vol. 306, no. 5696, pp. 666–669, 2004.

[126] A. K. Geim and K. S. Novoselov, "The rise of graphene," *Nature materials*, vol. 6, no. 3, pp. 183–191, 2007.

[127] A. K. Geim, "Graphene: status and prospects," *science*, vol. 324, no. 5934, pp. 1530–1534, 2009.

[128] C. Lee, X. Wei, J. W. Kysar, and J. Hone, "Measurement of the elastic properties and intrinsic strength of monolayer graphene," *science*, vol. 321, no. 5887, pp. 385–388, 2008.

[129] G. W. Hanson, "Dyadic greens functions and guided surface waves for a surface conductivity model of graphene," *Journal of Applied Physics*, vol. 103, no. 6, p. 064302, 2008.

[130] V. Gusynin, S. Sharapov, and J. Carbotte, "Magneto-optical conductivity in graphene," *Journal of Physics: Condensed Matter*, vol. 19, no. 2, p. 026222, 2006.

[131] M. Liu, X. Yin, E. Ulin-Avila, B. Geng, T. Zentgraf, L. Ju, F. Wang, and X. Zhang, "A graphene-based broadband optical modulator," *Nature*, vol. 474, no. 7349, pp. 64–67, 2011.

[132] S. H. Lee, M. Choi, T.-T. Kim, S. Lee, M. Liu, X. Yin, H. K. Choi, S. S. Lee, C.-G. Choi, and S.-Y. Choi, "Switching terahertz waves with gate-controlled active graphene metamaterials," *Nature materials*, vol. 11, no. 11, p. 936, 2012.

[133] B. Sensale-Rodriguez, R. Yan, S. Rafique, M. Zhu, W. Li, X. Liang, D. Gundlach, V. Protasenko, M. M. Kelly, and D. Jena, "Extraordinary control of terahertz beam reflectance in graphene electro-absorption modulators," *Nano letters*, vol. 12, no. 9, pp. 4518–4522, 2012.

[134] W. Gao, J. Shu, K. Reichel, D. V. Nickel, X. He, G. Shi, R. Vajtai, P. M. Ajayan, J. Kono, and D. M. Mittleman, "High-contrast terahertz wave modulation by gated graphene enhanced by extraordinary transmission through ring apertures," *Nano letters*, vol. 14, no. 3, pp. 1242–1248, 2014.

[135] G. Liang, X. Hu, X. Yu, Y. Shen, L. H. Li, A. G. Davies, E. H. Linfield, H. K. Liang, Y. Zhang, and S. F. Yu, "Integrated terahertz graphene modulator with 100% modulation depth," *ACS photonics*, vol. 2, no. 11, pp. 1559–1566, 2015.

[136] K. Z. Rajab, M. Naftaly, E. H. Linfield, J. C. Nino, D. Arenas, D. Tanner, R. Mittra, and M. Lanagan, "Broadband dielectric characterization of aluminum oxide (al2o3)," *Journal of Microelectronics and Electronic Packaging*, vol. 5, no. 1, pp. 2–7, 2008.

[137] A. ZurutuzaáElorza *et al.*, "Highly air stable passivation of graphene based field effect devices," *Nanoscale*, vol. 7, no. 8, pp. 3558–3564, 2015.

[138] H. J. Xu, W. B. Lu, Y. Jiang, and Z. G. Dong, "Beam-scanning planar lens based on graphene," *Applied Physics Letters*, vol. 100, no. 5, p. 051903, 2012.

[139] C.-H. Liu and X. Yu, "Silver nanowire-based transparent, flexible, and conductive thin film," *Nanoscale Res. Lett*, vol. 6, no. 1, p. 75, 2011.

[140] Nsi-rf-sg10. [Online]. Available: http://ww2.nearfield.com/Sales/datasheets/pdfs/NSI-RF-SG10.pdf

[141] W. L. Stutzman and G. A. Thiele, *Antenna theory and design.* John Wiley & Sons, 2013.

[142] Acs material trivial transfer graphene user instruction. [Online]. Available: http://acsmaterial.com/upload/124/UserInstructionACSMaterialTTG.pdf

[143] J. Yang, D. Sell, and J. A. Fan, "Freeform metagratings based on complex light scattering dynamics for extreme, high efficiency beam steering," *Annalen der Physik*, vol. 530, no. 1, p. 1700302, 2018.

[144] N. Yu and F. Capasso, "Flat optics with designer metasurfaces," *Nature materials*, vol. 13, no. 2, p. 139, 2014.

[145] S. M. Raeis-Zadeh, M. Haghtalab, and S. Safavi-Naeini, "Graphene-based controllable antenna for terahertz photomixer sources," in *Antennas and Propagation Society International Symposium (APSURSI), 2014 IEEE.* IEEE, 2014, pp. 862–863.

[146] G. Dural and M. I. Aksun, "Closed-form green's functions for general sources and stratified media," *Microwave Theory and Techniques, IEEE Transactions on*, vol. 43, no. 7, pp. 1545–1552, 1995.

[147] D. S. Hecht, L. Hu, and G. Irvin, "Emerging transparent electrodes based on thin films of carbon nanotubes, graphene, and metallic nanostructures," *Advanced Materials*, vol. 23, no. 13, pp. 1482–1513, 2011.

[148] K. Z. Rajab, M. Naftaly, E. H. Linfield, J. C. Nino, D. Arenas, D. Tanner, R. Mittra, and M. Lanagan, "Broadband dielectric characterization of aluminum oxide (al2o3)," *Journal of Microelectronics and Electronic Packaging*, vol. 5, no. 1, pp. 2–7, 2008.

[149] V. M. Shalaev, "Optical negative-index metamaterials," *Nature photonics*, vol. 1, no. 1, pp. 41–48, 2007.

[150] L. Tsang and J. A. Kong, *Scattering of electromagnetic waves.* John Wiley & Sons, 2004, vol. 26.

[151] S.-K. Hong, J. Brand, J. Choi, M. Jain, J. Mehlman, S. Katti, and P. Levis, "Applications of self-interference cancellation in 5g and beyond," *Communications Magazine, IEEE*, vol. 52, no. 2, pp. 114–121, 2014.

[152] M. Haghtalab and S. Safavi-Naeini, "Freeform engineered disordered metalenses for super-resolution imaging and communication," *Optics express*, vol. 26, no. 8, pp. 9749–9771, 2018.